

1 **Subduction, underplating, and return flow recorded in**
2 **the Cycladic Blueschist Unit exposed on Syros, Greece**

3 **Alissa J. Kotowski^{1*}, Whitney M. Behr^{1,2}, Miguel Cisneros^{1,2}, Daniel F.**
4 **Stockli¹, Konstantinos Soukis³, Jaime D. Barnes¹, Daniel Ortega-Arroyo^{1†}**

5 ¹Department of Geological Sciences, Jackson School of Geosciences, University of Texas at Austin, USA

6 ²Geological Institute, Department of Earth Sciences, Swiss Federal Institute of Technology (ETH)

7 ³Geology and Geoenvironment, National and Kapodistrian University of Athens, Greece

8 **Key Points:**

- 9 • Syros is a tectonic stack composed of 3 slices constructed by subduction and under-
10 plating; peak subduction ages young with structural depth.
11 • The subduction-to-exhumation transition is marked by kinematic rotation and cooling
12 during decompression.
13 • Metamorphic geochronology indicates syn-subduction exhumation occurred continu-
14 ously in an Eocene-Oligocene subduction channel.

*now at Department of Earth and Planetary Sciences, McGill University

†now at Department of Earth, Atmospheric & Planetary Sciences, Massachusetts Institute of Technology

Corresponding author: Alissa J. Kotowski, alissa.kotowski@mcgill.ca

15 **Abstract**

16 Exhumed high-pressure/low-temperature (HP/LT) metamorphic rocks provide insights
 17 into deep ($\sim 20\text{-}70$ km) subduction interface dynamics. On Syros Island (Cyclades, Greece),
 18 the Cycladic Blueschist Unit (CBU) preserves blueschist-to-eclogite facies oceanic- and
 19 continental-affinity rocks that record the structural and thermal evolution associated with
 20 Eocene subduction. Despite decades of research, the pressure-temperature- deformation
 21 history (P-T-D) and timing of subduction and exhumation are matters of ongoing discus-
 22 sion. Here we show that the CBU on Syros comprises three coherent tectonic slices, and
 23 each one underwent subduction, underplating, and syn-subduction return flow along sim-
 24 ilar P-T trajectories, but at progressively younger times. Subduction and return flow are
 25 distinguished by stretching lineations and ductile fold axis orientations: top-to-the-S-SW
 26 (prograde-to-peak subduction), top-to-the-NE (blueschist facies exhumation), and then E-
 27 W coaxial stretching (greenschist facies exhumation). Amphibole chemical zonations record
 28 cooling during decompression, indicating return flow along the top of a cold subducting
 29 slab. New multi-mineral Rb-Sr isochrons and compiled metamorphic geochronology suggest
 30 that three nappes record distinct stages of peak subduction (53-52 Ma, ~ 50 Ma (?), and
 31 47-45 Ma) that young with structural depth. Retrograde blueschist and greenschist facies
 32 fabrics span $\sim 50\text{-}40$ Ma and $\sim 43\text{-}20$ Ma, respectively, and also young with structural depth.
 33 The datasets support a revised tectonic framework for the CBU, involving subduction of
 34 structurally distinct nappes and simultaneous return flow of previously accreted tectonic
 35 slices in the subduction channel shear zone. Distributed, ductile, dominantly coaxial return
 36 flow in an Eocene-Oligocene subduction channel proceeded at rates of $\sim 1.5\text{-}5$ mm/yr, and
 37 accommodated $\sim 80\%$ of the total exhumation of this HP/LT complex.

38 **1 Introduction**

39 The mechanical and thermal properties of the subduction interface strongly influence
 40 the internal structure, kinematics, and dynamics of a subduction zone (e.g., Agard et al.,
 41 2018; Cloos, 1982; Gerya & Stöckhert, 2002). Along the shallow interface (≤ 20 km),
 42 direct observations of the megathrust and accretionary wedge are possible through high-
 43 resolution seismic reflection imaging, ocean bottom seismometers, and ocean drilling projects
 44 (e.g., Fagereng et al., 2019; H. Kimura et al., 2010; Park et al., 2002). However, seismic
 45 tomography and earthquake seismology have limited spatial and temporal resolution (e.g.,
 46 Calvert et al., 2011; Rondenay et al., 2008) so the geometry and internal structure of the
 47 deep interface ($\sim 20\text{-}70+$ km) remain poorly understood (Agard et al., 2018; Chemenda et
 48 al., 1995; Gerya & Stöckhert, 2002; Platt, 1993).

49 The deep interface can be studied through geologic observations of exhumed high-
 50 pressure/low-temperature (HP/LT) metamorphic rocks. Some of the most spectacular ex-
 51 amples – e.g., the Franciscan Complex (e.g., Cloos, 1986; Wakabayashi, 1990), Japan (Aoki
 52 et al., 2008; G. Kimura et al., 2012), and the Mediterranean region (e.g., Brun & Faccenna,
 53 2008; Jolivet et al., 2003; Platt et al., 1998) – have profoundly shaped our understanding of
 54 subduction and exhumation processes. Specifically, field studies provide constraints on the
 55 structural and kinematic evolution, interface geometry, metamorphic pressure-temperature
 56 (P-T) trajectories, and timing and rates of subduction and exhumation (e.g., Agard et al.,
 57 2018; Angiboust et al., 2016; Behr & Platt, 2012; Dragovic et al., 2015; Platt et al., 2018;
 58 Ukar et al., 2012; Xia & Platt, 2017). Geologic observations can validate or challenge the
 59 results of geodynamic simulations that model the kinematics and dynamics of rock within
 60 plate boundary shear zones (e.g., Cloos, 1982; Gerya & Stöckhert, 2002; Gerya et al., 2002;
 61 Warren et al., 2008).

62 Syros Island, located in the central Aegean Sea (Fig. 1), is an ideal locality to study
 63 deep subduction interface processes due to its exceptional preservation and exposure of
 64 HP/LT blueschist-to-eclogite facies assemblages (Dürr et al., 1978; Okrusch & Bröcker, 1990;
 65 Ridley, 1982, 1984). Despite decades of research on Syros, there are many disagreements

66 regarding the structural evolution, metamorphic conditions, and timing and mechanisms of
 67 subduction and exhumation on the island (e.g., Aravadinou & Xypolias, 2017; Bröcker et
 68 al., 2013; Keiter et al., 2004; Laurent et al., 2016, 2018; Lister & Forster, 2016; Ridley,
 69 1982; Ring & Layer, 2003; Rosenbaum et al., 2002; Schumacher et al., 2008; Skelton et al.,
 70 2019; Soukis & Stockli, 2013; Trotet, Jolivet, & Vidal, 2001). Furthermore, crustal-scale
 71 extensional detachments that accommodated the latest stages of post-orogenic exhumation
 72 are well-documented across the Cyclades (Avigad & Garfunkel, 1989, 1991; Gautier et al.,
 73 1993; Grasemann et al., 2012; Jolivet et al., 2010; Jolivet & Brun, 2010; Schneider et al.,
 74 2018; Soukis & Stockli, 2013), but workers still debate the relative importance of major
 75 detachments during syn-orogenic exhumation from peak conditions, and whether strain was
 76 distributed or highly localized on Syros (Bond et al., 2007; Keiter et al., 2004; Laurent et
 77 al., 2016; Lister & Forster, 2016; Rosenbaum et al., 2002).

78 In this work, we present new structural and petrologic data and Rb-Sr geochronol-
 79 ogy, and integrate our results with a synthesis of previously published geochronology, to
 80 present a new model for the evolution of the CBU on Syros. Our results refine the island’s
 81 deformation-metamorphism history, and shed light on the kinematics, metamorphic con-
 82 ditions, and timing of subduction and return flow in the Hellenic subduction zone. This
 83 work has implications for rates and mechanisms of HP/LT rock exhumation, and provides
 84 a broader framework for regional construction of the Attic-Cycladic Complex.

85 2 Regional Geologic Setting

86 The Cycladic Islands and parts of mainland Greece are part of the Attic-Cycladic
 87 Complex (ACC), which is divided into three units according to depositional age and meta-
 88 morphic history. From structural top to bottom, the units are: (1) the Upper Cycladic
 89 Nappe; (2) the Cycladic Blueschist Unit; and (3) the Basal Unit (e.g., Altherr et al., 1994;
 90 Avigad & Garfunkel, 1989; Dürr et al., 1978; Jacobshagen, 1986; van der Maar & Jansen,
 91 1983) (Fig. 1). The Upper Cycladic Nappe is a suite of ophiolitic slivers, altered carbon-
 92 ates \pm serpentinites, Late Cretaceous (70-100 Ma) amphibolite-facies orthogneisses, and
 93 Miocene greenschist-facies meta-basalts, and correlates with the Pelagonian Unit exposed
 94 on mainland Greece (Papanikolaou, 1987). The Upper Nappe was the upper plate during
 95 Late Cretaceous-Paleogene subduction and crops out above the Cycladic Blueschist Unit
 96 (CBU) in the hanging wall of crustal-scale, Miocene detachment faults on several Cycladic
 97 Islands (Jolivet et al., 2010, 2013; Soukis & Stockli, 2013).

98 The majority of the ACC is composed of the Cycladic Blueschist Unit (CBU) (Fig.
 99 1). The CBU comprises poly-metamorphosed tectonic slices (Dürr et al., 1978; Forster &
 100 Lister, 2005, 2008; Jolivet & Brun, 2010) of the following protoliths: (1) (Jurassic?-to-)
 101 Cretaceous (\sim 80 Ma) mafic igneous crust with enriched-MORB and back-arc geochemical
 102 signatures \pm serpentinitized mantle (Bonneau, 1984; Bulle et al., 2010; Cooperdock et al.,
 103 2018; Fu et al., 2015; Seck et al., 1996; Tomaschek et al., 2003), (2) Triassic (\sim 240 Ma)
 104 bimodal rift volcanics (Bolhar et al., 2017; Keay, 1998; Löwen et al., 2015; Robertson,
 105 2007) blanketed by Triassic-to-Cretaceous, locally-sourced, rifted and passive continental
 106 margin siliciclastic and carbonate rocks (Löwen et al., 2015; Papanikolaou, 2013; Poulaki
 107 et al., 2019; Seman, 2016; Seman et al., 2017), and (3) peri-Gondwanan basement cross-
 108 cut by Carboniferous calc-alkaline granitoids (Flansburg et al., 2019; Keay, 1998; Keay &
 109 Lister, 2002). Regionally, CBU lithologies record evidence for HP/LT metamorphism under
 110 blueschist-to-eclogite facies (‘M1’) conditions between \sim 53-30 Ma (Cliff et al., 2016; Dixon,
 111 1976; Lagos et al., 2007; Laurent et al., 2017; Okrusch & Bröcker, 1990; Ring, Glodny, et
 112 al., 2007; Schliestedt, 1986; Tomaschek et al., 2003; J. R. Wijbrans et al., 1990). The CBU
 113 was exhumed first within the subduction channel, leading to blueschist and greenschist
 114 facies overprinting (e.g. Cliff et al., 2016; Kotowski & Behr, 2019; Laurent et al., 2018;
 115 Ring et al., 2020), and then in the footwalls of crustal-scale, low-angle normal faults of
 116 the North, West, and South Cycladic (Grasemann et al., 2012; Jolivet et al., 2003, 2010;
 117 Jolivet & Brun, 2010; Ring et al., 2003, 2011; Roche et al., 2016; Soukis & Stockli, 2013), the

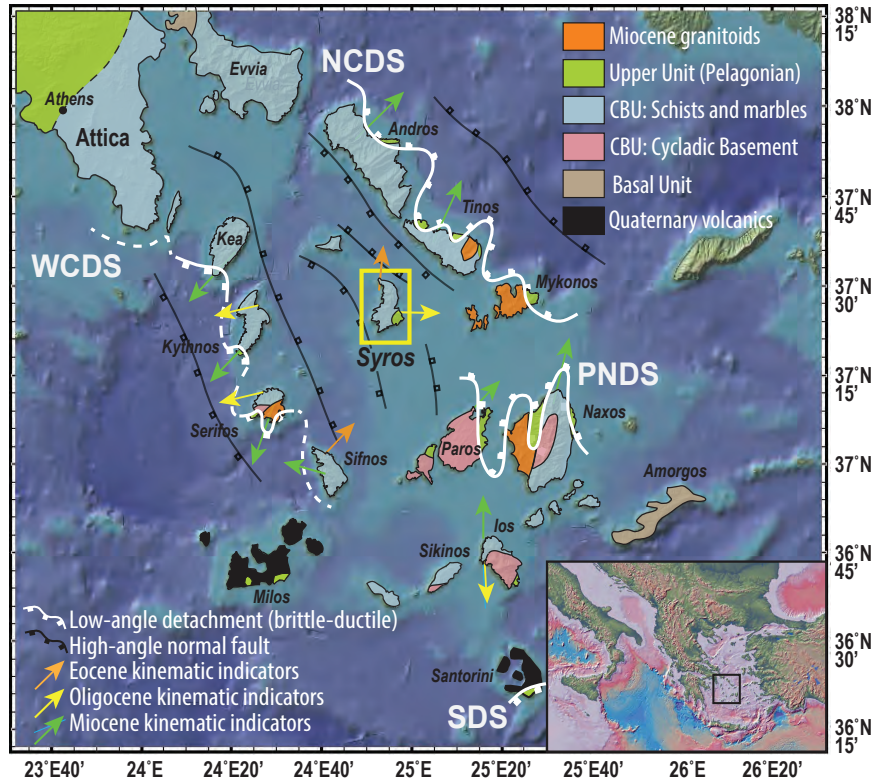


Figure 1: Regional tectonic map of the Cyclades, modified from Grasemann et al. (2012). Syros is outlined by the yellow box. North Cycladic (NCDS), West Cycladic (WCDS), Paros-Naxos (PNDS), and Santorini (SDS) Detachment Systems are outlined in white. Kinematic indicators are from Aravadinou et al. (2016), Forster et al. (2020), Grasemann et al. (2012), Huet et al. (2009) and references therein.

118 Paros-Naxos (Gautier et al., 1993), and the Santorini Detachment Systems (Schneider et al.,
 119 2018). Exhumation beneath ductile and semi-brittle detachments led to the development
 120 of Metamorphic Core Complexes (MCCs) that locally also produced a greenschist-facies
 121 ('M2') overprint (Bröcker, 1990; Bröcker et al., 1993). As slab rollback initiated and the
 122 arc migrated southward through the former forearc, Miocene I-type plutons intruded the
 123 exhuming CBU, and MCC formation led to a local high-temperature, amphibolite-facies
 124 ('M3') overprint on some islands (e.g., Paros and Naxos, Mykonos, and Ikaria) between
 125 ~21-17 Ma (Andriessen et al., 1979; Brichau et al., 2007; Lister et al., 1984; Pe-Piper et
 126 al., 2002; Rabillard et al., 2018; Vanderhaeghe & Whitney, 2004; J. Wijbrans & McDougall,
 127 1988).

128 3 The CBU on Syros Island

129 3.1 Rock types and tectonostratigraphy

130 Syros is a small island (~84 km²) in the central Cyclades and is dominantly composed
 131 of CBU with a klippe of UU in the southeast in the hanging wall of the Oligo-Miocene
 132 Vari Detachment (Ridley, 1984; Ring et al., 2003; Keiter et al., 2011; Soukis & Stockli,
 133 2013) (Fig. 1). In the context of the Cyclades, Syros best preserves the regional HP/LT
 134 metamorphic event (Ridley, 1982; Okrusch & Bröcker, 1990), but similar assemblages are
 135 preserved on the island of Sifnos (Aravadinou et al., 2016; Roche et al., 2016).

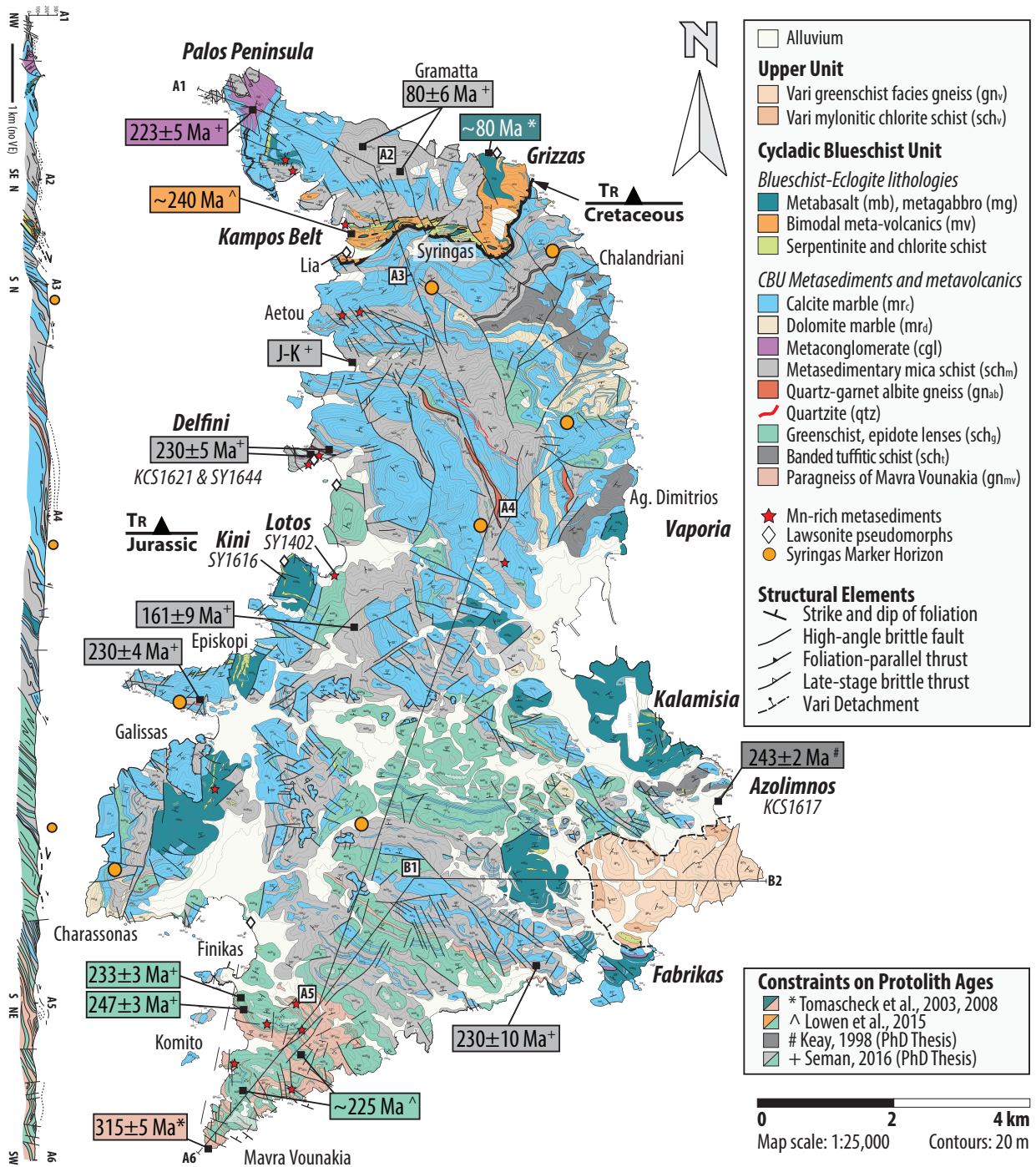


Figure 2: Geologic and structural map of Syros Island, modified from Keiter et al. (2004, 2011). Structural elements and locations of the Syringas Marker Horizon are from Keiter et al. (2011). Constraints on protolith ages are from the references discussed in Section 3.1. Protolith ages are color coded according to rock type. Localities discussed in this study are shown in bold italics, new Rb-Sr sample names and locations are in italics.

136 Within the CBU on Syros, mafic blueschists and eclogites crop out along three tectonostratigraphic horizons: Kampos Belt, Kini-Vaporía-Kalamisia, and Galissas-Fabrikas. Each
 137 horizon exposes ~300-500 m (structural thickness) of blueschist-to-eclogite facies meta-
 138 basalts and gabbros, serpentinites, and bimodal blueschist-quartz schist meta-volcanics in
 139 varying proportions. Along Kampos Belt, eclogitic meta-gabbros, blueschist facies bimodal
 140 meta-volcanics, and serpentinite/chlorite-talc schists are most abundant (Dixon & Ridley,
 141 1987; Keiter et al., 2011; Ridley, 1982) (Fig. 2). Kini, Vaporía (north of Ermoupoli),
 142 and Kalamisia are primarily composed of fine-grained mafic blueschist, and contain pods
 143 and lenses of eclogite (centimeters-to-decimeters in diameter) and meters-thick layers of
 144 serpentinite/talc schist (Keiter et al., 2011; Kotowski & Behr, 2019). Fabrikas comprises
 145 coarse-grained glaucophane-bearing eclogites (centimeters to meters in diameter) within a
 146 fine-grained matrix of mafic blueschists and quartz-mica schists, capped by meta-carbonate
 147 (Kotowski & Behr, 2019; Ring et al., 2020; Skelton et al., 2019). Keiter et al. (2011)
 148 suggested that mafic blueschists and eclogites are genetically related, and changes in vol-
 149 ume proportions of lithologies reflect primary lateral and/or vertical ‘facies changes’ of an
 150 enriched-MORB or back-arc igneous suite.
 151

152 The majority of the CBU comprises a ~6-8 km section of intercalated meta-volcanic
 153 and meta-sedimentary schists, and calcite- and dolomite-marbles with Jurassic-to-Cretaceous
 154 depositional ages (Keiter et al., 2004; Löwen et al., 2015; Papanikolaou, 2013; Seman et al.,
 155 2017) (Fig. 2). Keiter et al. (2004, 2011) documented a series of boudinaged marbles,
 156 cherts, and albite-bearing quartzite, which they named the Syringas Marker Horizon (or-
 157 ange dots on Fig. 2). The sequence crops out at 3 or 4 different structural levels suggesting
 158 it marks several km-scale thrust sheets and may reflect relict primary sedimentary layering
 159 (Dixon & Ridley, 1987; Keiter et al., 2011; Ridley, 1982). Repetition of the Syringas Marker
 160 Horizon by km-scale folding is unlikely because the largest observable upright folds within
 161 this sequence have amplitudes of several hundreds of meters and the marker horizon never
 162 appears to be overturned (Keiter et al., 2011). Furthermore, Keiter et al. (2011) docu-
 163 mented repetition of distinct packages of bimodal, rift-related meta-volcanics (also mapped
 164 as “banded tuffitic schists”) that have Triassic magmatic protolith ages (Keay, 1998; Löwen
 165 et al., 2015; Pe-Piper et al., 2002; Seman, 2016) (Fig. 2), and Seman (2016) presented detri-
 166 tal zircon (DZ) Maximum Depositional Ages (MDA) for meta-sedimentary rocks that reveal
 167 young-on-old tectonostratigraphic inversions; both results appear to support imbrication.

168 3.2 Previously proposed P-T-D-t paths

169 Previously published P-T-D evolutions for Syros fall into two categories. Some work-
 170 ers have argued that the majority of deformation and metamorphism on the island is
 171 exhumation-related (Laurent et al., 2016; Lister & Forster, 2016; Trotet, Jolivet, & Vi-
 172 dal, 2001) (Fig. 3A). These studies interpret mafic blueschists and eclogites to occupy the
 173 top of the structural pile and separate them from underlying meta-sedimentary rocks along
 174 extensional shear zones (Forster & Lister, 2005; Laurent et al., 2016, 2018; Trotet, Vidal,
 175 & Jolivet, 2001). An implication of this model is that distinct rock types were juxtaposed
 176 during syn-orogenic exhumation (Forster & Lister, 2005; Laurent et al., 2016). Fresh and
 177 retrogressed eclogite has been documented throughout the structural pile on Syros, which
 178 is considered evidence that all rocks reached high-pressure conditions during subduction.
 179 However, lithologic packages that currently occupy different structural depths could have
 180 followed different P-T paths during exhumation (cf. Laurent et al., 2018; Trotet, Vidal,
 181 & Jolivet, 2001; Trotet, Jolivet, & Vidal, 2001), and/or could have been subducted at dif-
 182 ferent times (Laurent et al., 2017; Lister & Forster, 2016). This model could potentially
 183 explain reported differences in P-T estimates across Syros; mafic blueschists and eclogites
 184 may have been subducted slightly deeper, earlier, compared to meta-sedimentary lithologies
 185 (as discussed by Schumacher et al. (2008)).

186 Alternatively, other work has suggested that prograde deformation and metamorphism
 187 on the island are locally preserved, and exhumation-related strain was partitioned into

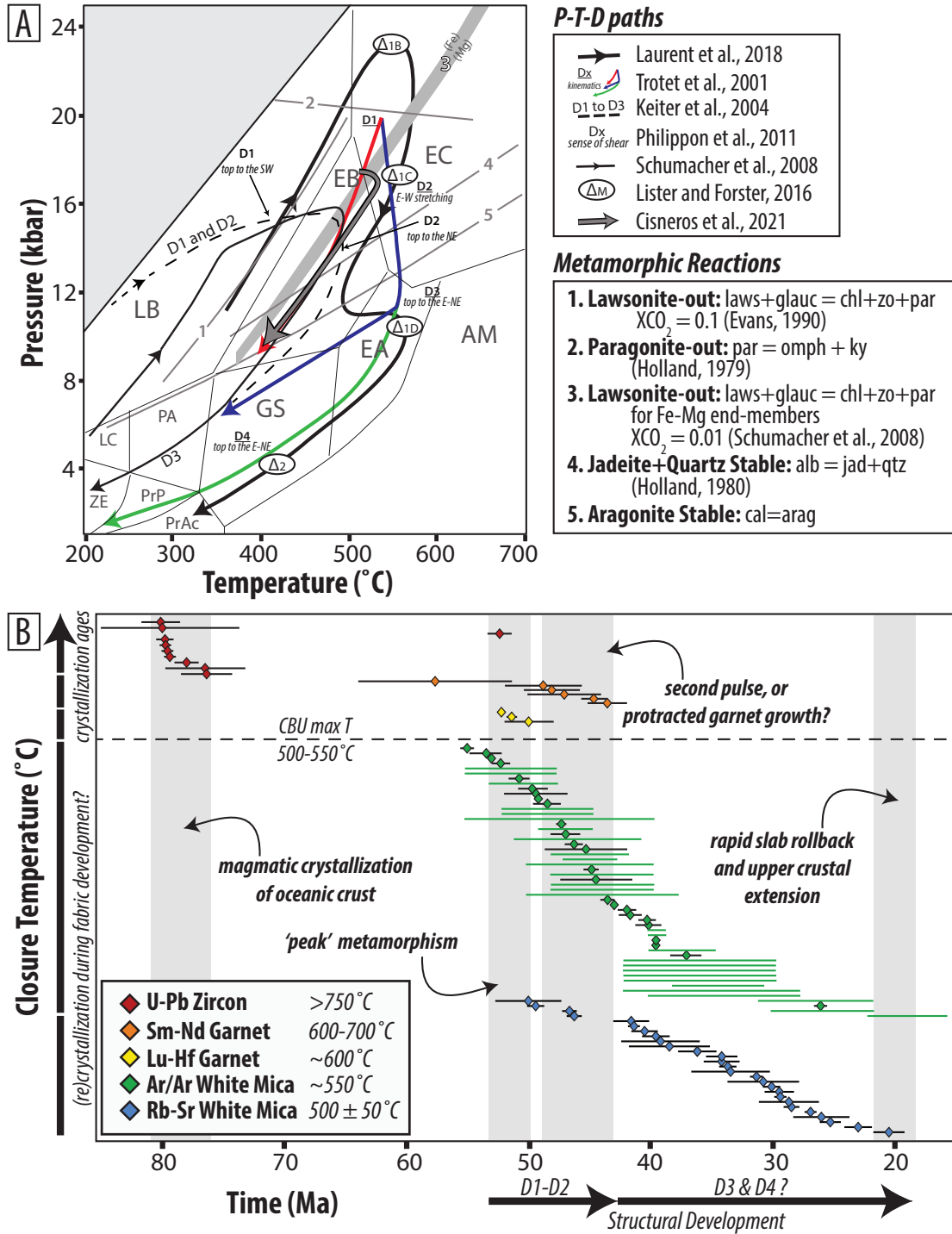


Figure 3: (A) Compilation of proposed P-T-D histories for the CBU on Syros. (B) Closure temperature vs. time for compiled metamorphic geochronology listed in Table A2. This dataset comprises 100 datapoints made up of 185 individual ages (some data clusters are weighted means), from 16 studies and 5 chronometers, from work published during the interval 1987-2019. The black bar at the bottom labeled 'structural development' shows that the timing and tectonic significance of progressive Eo-Oligocene deformation events (see also D1-D4 in panel A) and corresponding fabric development is contentious.

weaker lithologies (Bond et al., 2007; Cisneros et al., in press; Keiter et al., 2004, 2011; Ridley, 1982; Rosenbaum et al., 2002) (Fig. 3A). These studies interpret mafic blueschist and eclogites to record primary relationships with surrounding schists and marbles, or to have been juxtaposed with the schists and marbles during early thrusting (Blake Jr et al., 1981; Hecht, 1985; Keiter et al., 2004; Ridley, 1982). For either of those cases, map-scale lenses of mafic blueschists and eclogites at Vaporia, Kalamisia, and Fabrikas need not be separated from surrounding CBU by faults or shear zones (i.e., the structurally highest Kampos sub-unit of Laurent et al. (2016)), but instead could occupy a range of structural depths throughout the tectonostratigraphic pile (Keiter et al., 2004). This model implies that meta-mafic and meta-sedimentary rocks that occupy similar structural levels were subducted together and experienced similar P-T histories through subduction and exhumation (Cisneros et al., in press; Keiter et al., 2011; Schumacher et al., 2008).

Although existing metamorphic ages help to roughly distinguish prograde from retrograde fabrics, and the timing of subduction vs. exhumation, clearly differentiating between these P-T-D evolutions has been challenging because of the difficulty in assigning geologic significance to ages (Fig. 3B). Two age clusters are commonly cited for the timing of peak subduction on Syros: ~ 53 -50 Ma (U-Pb zircon, Ar/Ar and Rb-Sr white mica, Lu-Hf garnet; Cliff et al. (2016); Lagos et al. (2007); Lister and Forster (2016); Tomaschek et al. (2003)), and both ~ 52 Ma *and* ~ 45 Ma for different underplated slices (Ar/Ar white mica; Forster and Lister (2005); Laurent et al. (2017); Lister and Forster (2016)). Garnet Sm-Nd and Lu-Hf ages span the proposed range, thus raising the question of whether garnet growth reflects two pulses or continuous growth at peak conditions (cf. Kendall, 2016). Furthermore, Ar/Ar and Rb-Sr ages span the entire Eocene. Maximum CBU temperatures do not appear to have exceeded those required for diffusional resetting of the Ar/Ar and Rb-Sr systems, therefore it is unclear whether retrograde blueschist-to-greenschist facies white mica ages record incomplete isotopic mixing, and/or partial or continuous recrystallization during exhumation, beneath the isotopic closure temperature of the Ar/Ar and Rb-Sr systems (Fig. 3B) (e.g., Bröcker et al., 2013; Cliff et al., 2016; Laurent et al., 2017; Rogowitz et al., 2014; Uunk et al., 2018). An additional challenge is that many geochronologic data points in Figure 3B were collected without a clear framework for linking the ages to specific fabric-forming events.

219 4 Approach and Methodology

220 4.1 Structural and Microstructural Analysis

Following detailed mapping by Keiter et al. (2004, 2011) (map in Figure 2 and 4), we collected new structural data at several localities from Northern Syros (Fig. 4A-C), Central Syros (Fig. 4D-H), and Southeastern Syros (Fig. 4I-K). Planar and linear structural elements were measured, including foliations and cleavages, axial planes to folds, fold axes, and mineral growth, crenulation and stretching lineations. We constructed π circle diagrams to constrain fold orientations by plotting poles to metamorphic foliation planes. Each color on a given stereonet in Figure 4 corresponds to poles to foliations of a specific rock type, or poles to foliations defining single outcrop-scale folds (e.g. Fig. 5I,K). Our measurements used to produce π diagrams were all derived from cylindrical structures; even if folds have curved hinge lines on larger scales, we measured folds in locations where hinge lines are locally straight. We calculated poles to mean circles to determine fold axis orientations (bold circles), and compared them to fold axes that could be directly measured (diamonds) and mineral lineations (open circles). We documented minerals defining lineations and fold axes, porphyroblast stability and kinematic context (i.e., pre-, syn-, post-kinematic with respect to surrounding fabric), and break-down and replacement textures (Fig. 5) to constrain metamorphic conditions of deformation. Microstructural analysis (Fig. 6) (139 total samples, 21 studied in detail) and quantitative EPMA analyses of zoned minerals (6 samples) further refined P-T-D conditions (Figs. 7, 8).

239

4.2 Rb-Sr Geochronology

240

241

242

243

244

245

246

247

248

249

250

251

252

253

254

We selected five samples for multi-mineral Rb-Sr geochronology. This technique has been applied to exhumed HP/LT metamorphic rocks to date deformation and metamorphism with great success (Angiboust et al., 2016; Cliff et al., 2016; Freeman et al., 1997; Glodny et al., 2005, 2008; Kirchner et al., 2016; Ring, Will, et al., 2007). The primary assumption required to construct a multi-mineral isochron is that the phases defining the isochron were co-genetic, such that they all inherited the same initial Sr composition. We separated and picked minerals that we hypothesized were co-genetic based on our structural and microstructural results, and quantitatively tested this hypothesis by identifying phases that were in isotopic disequilibrium (i.e., fell off the isochron) (Cliff & Meffan-Main, 2003). Strong foliations support the assumption of syn-kinematic recrystallization of selected minerals, which can reset the Sr isotopic signature between mica and co-genetic phases to temperatures as low as 300°C (Müller et al., 2000). Furthermore, diffusional resetting of the Rb-Sr system is thought to begin at ~550-600°C (Glodny et al., 2008; Inger & Cliff, 1994), which exceeds maximum temperatures in the CBU. Therefore, we interpret our Rb-Sr ages as (re-)crystallization ages associated with deformation.

255

256

257

258

259

260

261

262

263

264

265

266

267

268

269

270

271

272

273

Following Glodny et al. (2003, 2008), we used a bulk mineral separation technique and cut out ~5 cm³ cubes of rock from hand samples to isolate specific fabrics corresponding to different stages of the deformation history recorded on Syros. Samples were crushed with a small hammer between sheets of paper, ground gently with a rock crusher, and sieved and separated by grain size. Grain size fractions 125-250 μm and 250-500 μm were frantzed to separate minerals based on magnetic susceptibility. Mineral separates were picked by hand under a microscope, and white mica separates were cleaned of inclusions by gently smearing them in a mortar and pestle and washing them through a sieve with ethanol. All Rb and Sr isotopic separation and analyses were done at the University of Texas at Austin in the Radiogenic Isotopic Clean Lab. All separates (except apatite) were cleaned in 2 N HCl to remove surficial contamination and spiked with mixed high Rb/Sr and low Rb/Sr spikes. We followed methodology for mineral dissolution, isotope column chemistry, Thermal Ionization Mass Spectrometry (Sr analyses), Solution Inductively Coupled Plasma Mass Spectrometry (Rb analyses), and estimating uncertainties in isotopic ratios as described in Kirchner et al. (2016). Reproducibility on replicate USGS Standard Hawaiian Basalt (BHVO) Rb measurements determine the uncertainty of the Rb-Sr ratio, and long-term reproducibility on the NBS987 Sr standard determines the uncertainty of the Sr ratio (Table 2). Ages were calculated using the IsoplotR toolbox (Vermeesch, 2018) with the ⁸⁷Rb decay constant of $1.3972 \pm 0.0045 \times 10^{-11}$ year⁻¹ (Villa et al., 2015).

274

5 Structures and Deformation Fabrics

275

276

277

278

279

280

281

282

283

284

The CBU on Syros records evidence for three main phases of deformation and metamorphism, herein referred to as D_R , D_S , and D_{T1-2} (Table 1). Subscripts follow an alphabetical order according to the relative age of deformation, i.e., D_R is the oldest observed deformation, and D_{T1-2} is the youngest. Each phase led to spaced to penetrative foliation development, and/or ductile folding of older foliations. Kinematic indicators, metamorphic mineral assemblages, and porphyroblast zonations described herein demonstrate that D_R and D_S developed on the prograde path and are best preserved in mafic blueschists and eclogites (but are locally preserved as textural relicts in bimodal meta-volcanics and meta-sediments), and D_T developed on the retrograde path and is best recorded by meta-volcanic and meta-sedimentary schists.

285

286

5.1 D_R – Prograde fabric development during subduction under blueschist facies conditions

287

288

D_R is the earliest recognizable prograde event but it is not visible at the outcrop-scale. D_R likely formed a strong, penetrative S_R foliation that is locally recorded as inclusion trails

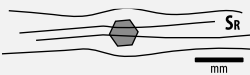
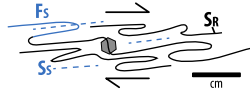
Event	Context	Diagnostic Structures	Metamorphism	Example Localities
D _R	Subduction	<ul style="list-style-type: none"> Only preserved as inclusion trails in garnets and as early fabric (S_R) that is tightly folded during D_S 	lawsonite-blueschist	N/A
D _S	Subduction to near-peak P-T conditions	<ul style="list-style-type: none"> Axial plane schistosity (S_s) associated with tight to isoclinal folds (F_s) that transpose the S_R foliation, with S-SW-plunging fold axes S-SW mineral and stretching lineations Dominantly non-coaxial with top-S-SW sense of shear, locally non-penetrative in mafic lenses (e.g. Grizzas) 	lawsonite blueschist-to-eclogite	Grizzas Kini
DT ₁₋₂	Exhumation	<ul style="list-style-type: none"> Crenulation cleavage (S_T) associated with upright, open-to-tight folds (F_T) that fold S_s S_s foliation continuously reworked and retrogressed Fold axes and mineral lineations rotate from N-NE (DT₁) to E-W (DT₂) as a function of strain Dominantly coaxial, but locally non-coaxial (e.g. near the Vari Detachment at Fabrikas, Kalamisia) Ductile to semi-brittle boudinage in later stages 	epidote-blueschist progressing to greenschist	Kamos (early) Azolimnos (early) Delfini (later) Lotos (later)

Table 1: Summary of interpreted deformation-metamorphism events in the CBU on Syros.

289 in garnet porphyroblasts at Kampos (Fig. 6A,B) and is tightly folded during D_S. Inclusion
 290 trails are orthogonal to the external foliation and are defined by glaucophane, omphacite,
 291 and white mica.

292 5.2 D_S – Prograde-to-peak fabric development during subduction under 293 blueschist to eclogite facies conditions

294 5.2.1 D_S Structures

295 D_S is best recorded at Grizzas and Kini (Fig. 4E), with relicts preserved on Kampos
 296 Belt (Fig. 4C), at Lia Beach, and at Azolimnos (Fig. 4J). D_S produced a dominant S_S
 297 foliation in mafic blueschists, meta-cherts, and bimodal meta-volcanics at Grizzas that is
 298 parallel to the axial planes of intrafolial folds (F_S), and rotated and boudinaged quartz
 299 veins. This folding event is characterized by shallowly to moderately plunging SW-trending
 300 fold axes clustering around 205-251°/15-35°; glaucophane mineral lineations are similarly
 301 oriented (Fig. 4B). In rare cases, outcrop-scale prograde metamorphism was not associated
 302 with penetrative deformation, indicated by preservation of igneous protolith features such as
 303 pillow lavas (Grizzas, cf. Keiter et al. (2011)), intrusive relationships (Kini, cf. Kotowski and
 304 Behr (2019) and Laurent et al. (2016)), and magmatic breccias (e.g., at Grizzas, Episkopi,
 305 Fig. 5A).

306 Kini dominantly records D_S deformation-metamorphism; it is bounded by high-angle
 307 normal faults and is structurally discordant with respect to the surrounding CBU (Fig. 4E;
 308 cf. Keiter et al. (2011)). In one location, serpentinite wraps around the base of massive meta-
 309 gabbros, which transitions upward into fine-grained blueschists, suggesting local preservation
 310 of an attenuated section of metamorphosed oceanic lithosphere (Fig. 5B). Similar to Grizzas,
 311 the D_S fabric in Kini blueschists contains isoclinal folds (F_S) with shallowly south-plunging
 312 fold axes. This fold generation is recorded by a 182°/33° fold axis in Kini schists (Fig. 4E;
 313 Fig. 5D). The S_S axial planar cleavage seen in Kini mafic blueschists (e.g., Fig. 5C,D) is also
 314 seen as textural relicts in quartz-mica rich lithologies, as at Azolimnos (Fig. 5G). In some
 315 localities, blue amphibole lineations define great circles, likely reflecting folding of earlier

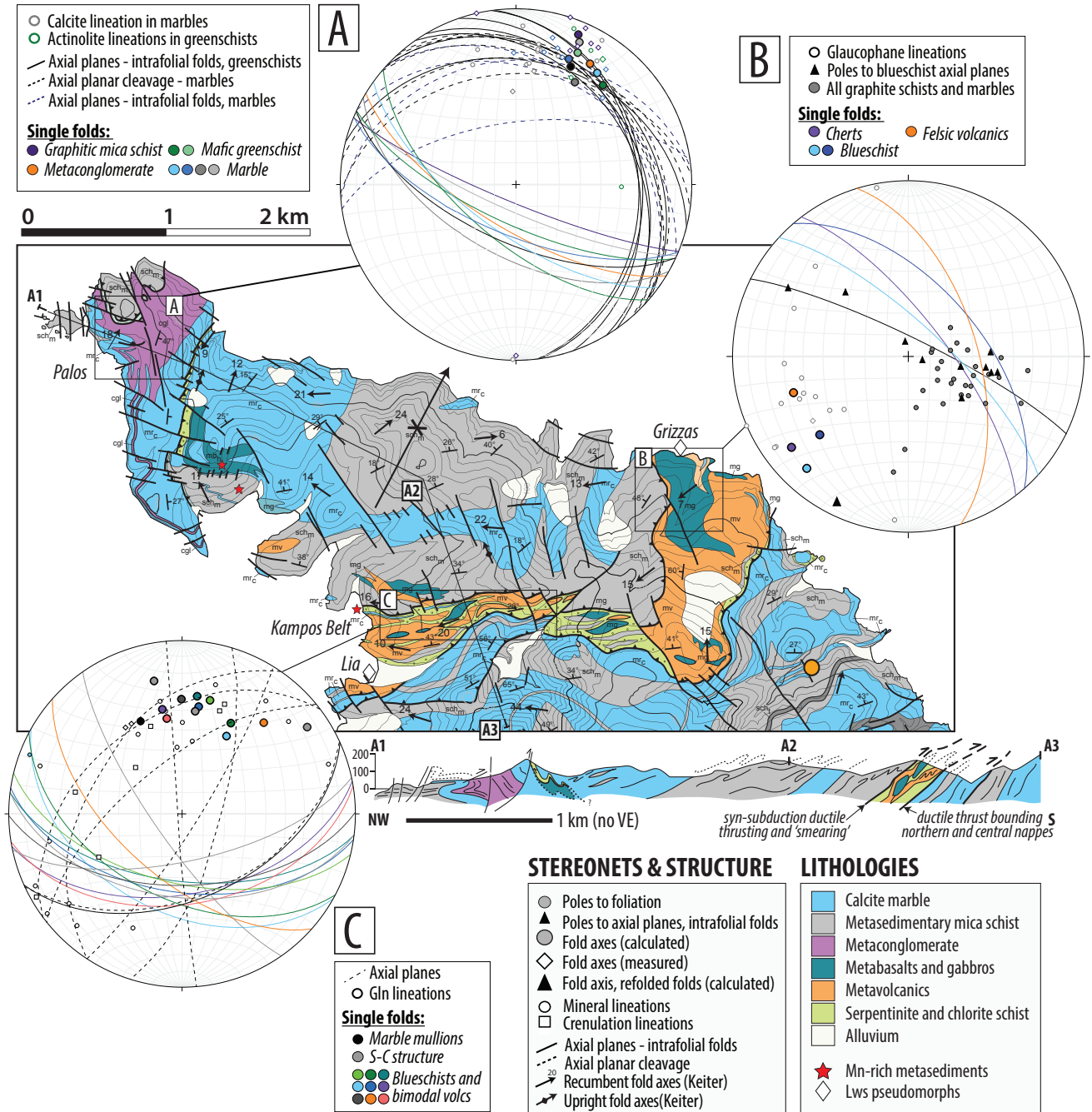


Figure 4: Geology and structural elements of Northern Syros. Base map, foliation orientations, and fold axes (black arrows) are from Keiter et al. (2011). Black fold axes are Keiter et al. (2011)'s intrafolial 'F2 shear folds.' The spread of orientations is the result of superposed folding, as older folds were progressively reoriented by S-vergent simple shear folding during prograde subduction (cf. Keiter et al., 2004). Foliations are plotted as poles (unless otherwise specified), and colored best-fit planes are π circles. Topographic contours are 20 m. New data plotted in stereonet were collected from the areas outlined by solid black boxes. Cross section A1-A2-A3 is modified from Keiter et al. (2011). See text for description of structural elements.

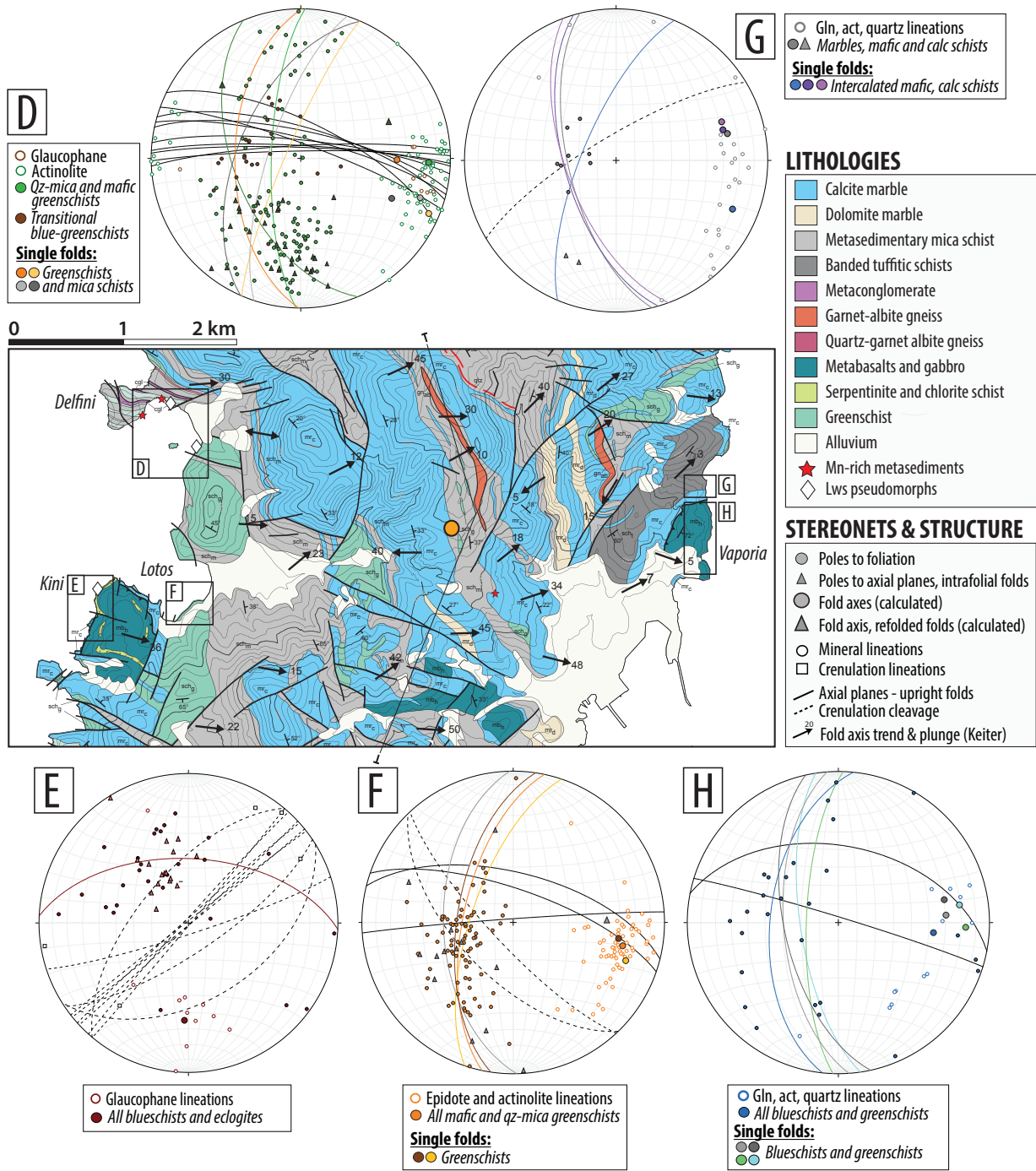


Figure 4: Continued. Geology and structural elements of Central Syros. See Fig. 2 for the cross section corresponding to the line shown.

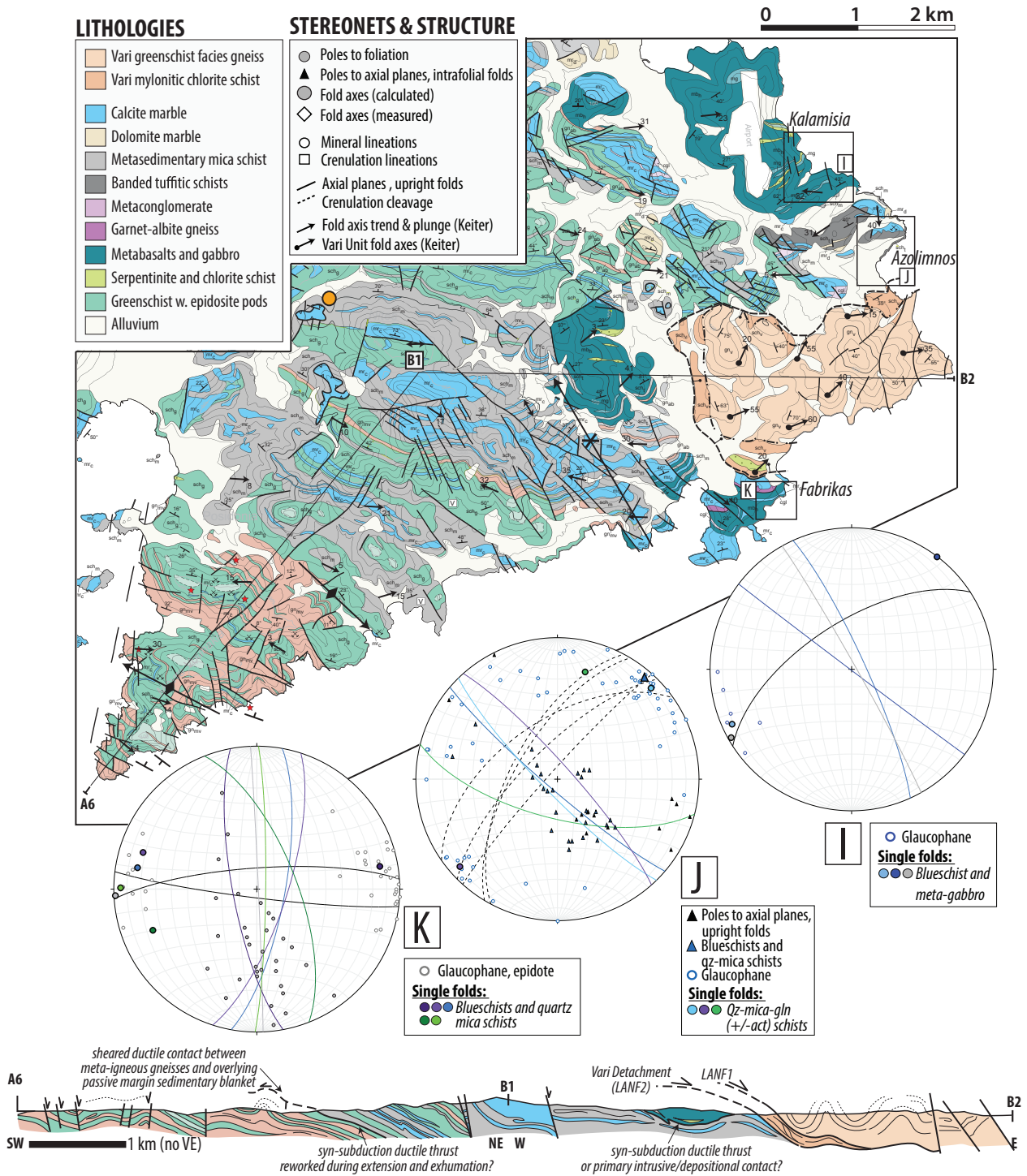


Figure 4: Continued. Geology and structural elements of Southeast Syros. Black arrows with the circles are upright fold axes in the Vari Unit. Cross section B1-B2-B3 is modified from Keiter et al. (2011); compare with Laurent et al. (2016).

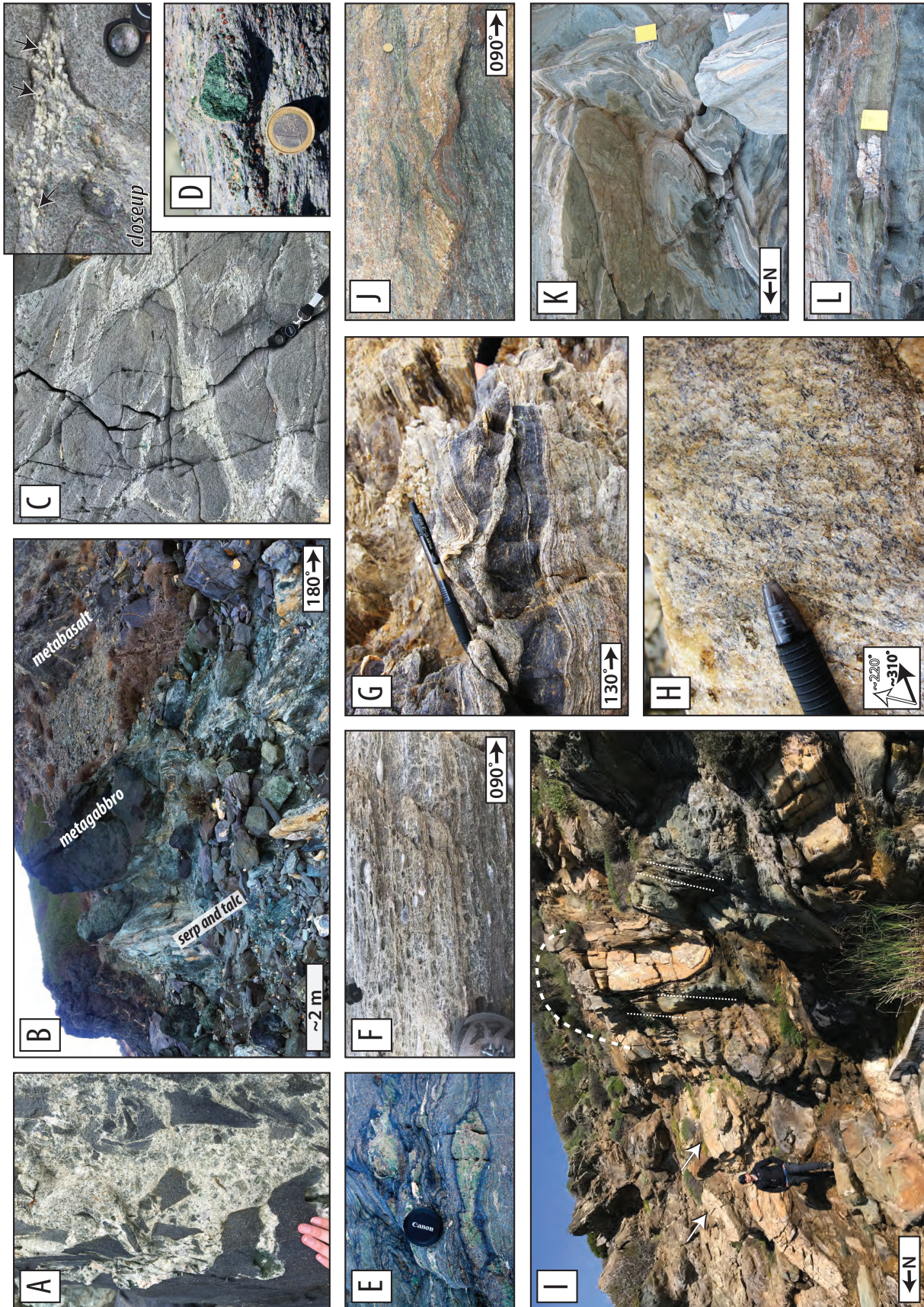


Figure 5: Caption next page.

Figure 5: (Previous page.) Selected field photos showing prograde (A-D) and retrograde (E-L) deformation and metamorphism. (A) Preservation of primary igneous breccias at Grizzas. (B) Right-side-up sequence of oceanic lithosphere at Kini. (C, D) S_S at Kini contains lawsonite pseudomorphs and omphacite with glaucophane- and garnet-filled pressure shadows. Black arrows in the close-up photo of (C) point to pseudomorphs with garnet inclusions. (E) D_{T1} retrogression under blueschist-facies conditions is marked by local static glaucophane coronas formed around pinched eclogite lenses at Vaporia. (F) Coaxial E-W stretching of calcite clasts in meta-conglomerate at Delfini during D_{T1-2} . (G,H) S_S is cut by S_{T1} crenulation cleavage at Azolimnos. (H) Two glaucophane lineations record transposition of S_S (black arrow, parallel to pen) into alignment with crenulation hinges (white arrow) during D_{T1} . (I-K) D_{T2} greenschist facies retrogression and upright folding at Delfini (I) and Lotos (K). (I) White arrows point to F_S folds along the limbs of F_T fold. Dashed white lines mark the axial planar S_T cleavage. (J) Non-coaxial, top-to-the-E extensional shear under retrograde blueschist-to-greenschist facies conditions at Fabrikas. (K) S_S cross-cut by D_T folding; fold axes trend E-W. (L) Coaxial, lineation-parallel D_{T2} brittle boudinage of epidote-rich lenses in greenschists.

316 (D_R) fabric during D_S (Fig. 4C, 4E; relicts at Azolimnos in Fig. 4J). In other localities, blue
 317 amphibole lineations appear to be reoriented into moderately S- or SW-plunging clusters
 318 (e.g., Grizzas and Kini, Fig. 4B,E). Similarly, Keiter et al. (2004, 2011) documented a
 319 significant spread of fold axis orientations which they attributed to superposed folding that
 320 systematically reoriented older fold hinges via S-vergent simple shear during prograde-to-
 321 peak subduction (i.e. their D_2 , black fold axes in Fig. 4).

322 Locally, centimeter-sized, prismatic pseudomorphs after lawsonite indicate that law-
 323 sonite grew at the culmination of D_S but did not survive peak conditions. Syn-to-post-
 324 kinematic porphyroblasts overgrow the mafic blueschist foliation at Grizzas and Lia, deco-
 325 rate foliation-parallel compositional layers at Kini (Fig. 5C), and commonly contain inclu-
 326 sions of garnet, and are included by garnet (Fig. 5C, closeup). Pseudomorphs are weakly
 327 attenuated along the limbs of folds, but preserve their diamond-like shapes in fold hinges
 328 (Fig. 5C).

329 **5.2.2 D_S Microstructures and Mineral Chemistry**

330 D_S micro-textures in meta-sedimentary rocks are characterized by strong quartz-mica
 331 cleavage-microlithon S_S fabrics and rotated inclusion trails in garnets that are mostly con-
 332 tinuous with external foliations (Fig. 6C). Quartz-rich microlithons have strong lineation-
 333 parallel shape-preferred orientations, and mica-rich cleavages comprise intergrown phengite
 334 and paragonite (Fig. 6C, Fig. 7C). Lawsonite pseudomorphs preserved as inclusions in
 335 garnet comprise intergrown epidote and white mica (Fig. 6D).

336 D_S micro-textures in mafic blueschists are characterized by compositional segregation
 337 defined by glaucophane-rich and epidote-rich layering alternating on the mm-scale (\sim 50-200
 338 μm grain size) (Fig. 6E). The S_S foliation contains syn-kinematic porphyroblasts of garnet
 339 and omphacite (\sim 300 μm -5 mm), and rutile with minor titanite overgrowths (Figs. 6F,
 340 7A). Syn-kinematic phengitic white mica is chemically homogeneous and has 3.35-3.45 Si
 341 atoms p.f.u. (Fig. B1). Omphacite and garnet deflect local foliations, and have pressure
 342 shadows and strain caps composed of glaucophane, phengite and paragonite, and/or more
 343 omphacite (Fig. 5D, 7A). Omphacite porphyroblasts in Kini blueschists have cores of low-
 344 Na, high-Mg omphacite, fringed by asymmetric, syn-kinematic pressure shadows of high-
 345 Na, low-Mg omphacite (Fig. 7A). D_S amphibole is glaucophane (Figs. 7A, 8A). Rare

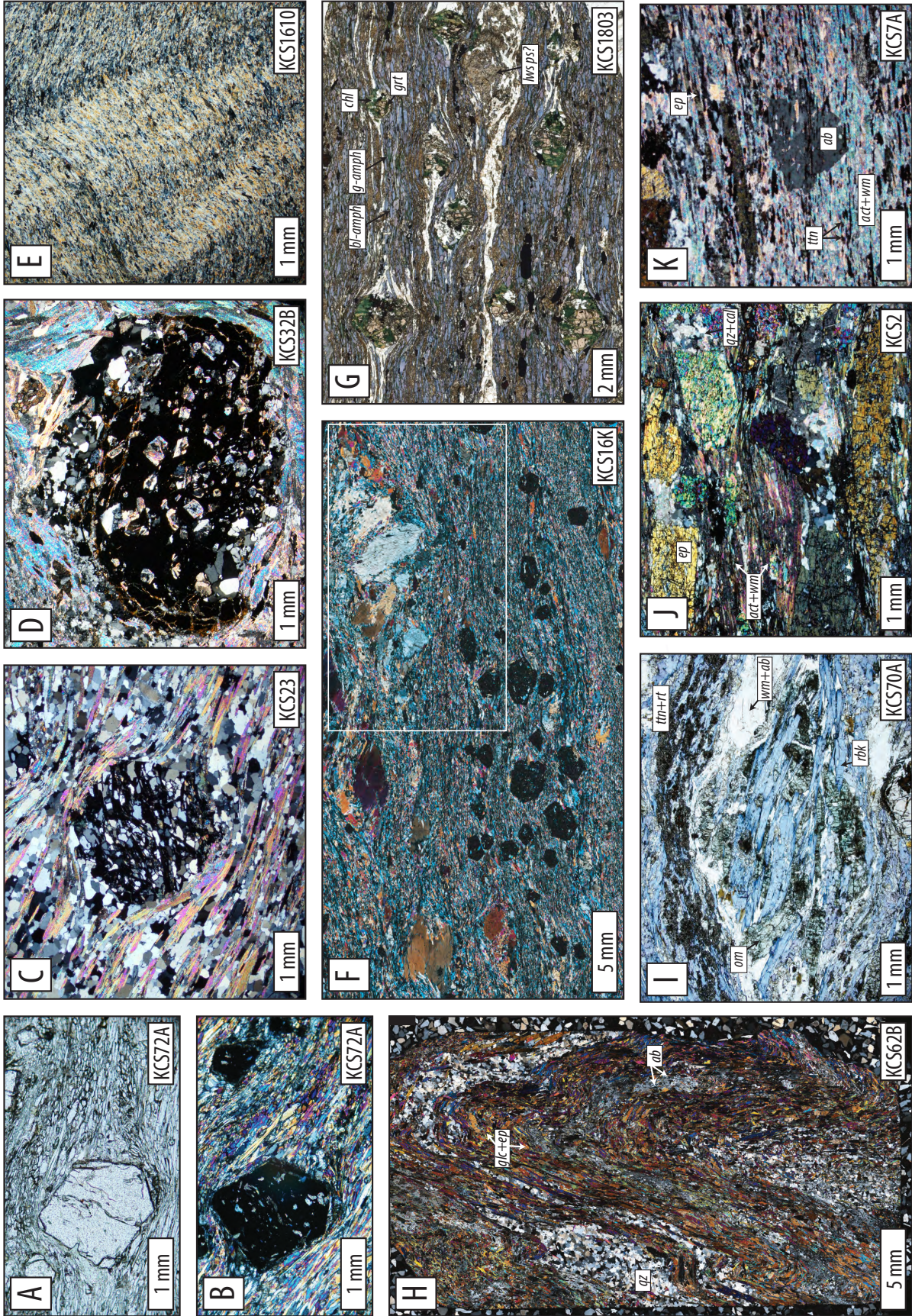


Figure 6: Caption next page.

Figure 6: (Previous page.) Selected photomicrographs showing prograde (A-F) and retrograde (E, G-K) deformation and metamorphism. (A,B) Internal S_R inclusion trails from Lia Beach (A, PPL; B, XPL). (C) S_S contains syn-kinematic garnet porphyroblasts with foamy quartz inclusion trails that are rotated but continuous with respect to the dominant external S_S foliation. (D) D_S garnets include pseudomorphs after lawsonite (comprising epidote and white mica). (E, F) S_S in mafic blueschists. (E) S_S is cut by D_{T1} crenulation under glaucophane-stable conditions in mafic blueschists. (F) Omphacite and garnet in D_S Kini blueschists have asymmetric pressure shadows filled with high-pressure minerals. (G-I) D_{T1} retrogression in bimodal meta-volcanics at Kampos (H), Azolimnos (H) and Kalamisia (I). (H) D_{T2} crenulation transposes S_S , and strengthens as albite, chlorite, and actinolite stabilize. (I) Omphacite and paragonite break down to epidote, blue amphibole, and albite. (J,K) D_{T2} in Lotos greenschists. (J) Brittle micro-boudinage of epidote porphyroblasts. (K) Final stages of D_{T2} are characterized by post-tectonic albite growth.

346 examples reveal glaucophane cores with thin, patchy rims (Fig. 7B) that trend towards
 347 lower $Al^{iv}/(Al^{iv}+Fe_{tot})$ values and higher $(Na+K)_A$ (Fig. 8A, Fig. B1).

348 **5.3 D_T – Retrograde fabric development, crenulation, and re-folding through** 349 **blueschist-to-greenschist facies conditions**

350 **5.3.1 D_T Structures**

351 D_{T1} is best recorded at Kampos Belt and Palos (Fig. 4A,C), Azolimnos (Fig. 4J),
 352 and Kalamisia (Fig. 4I), and locally at Kini (Fig. 4E). D_{T1} structures re-fold older S_S folia-
 353 tions into inclined-to-upright, open-to-tight, shallowly to moderately N- and NE-plunging
 354 folds (Fig. 4C, 4G,H, 4I,J; C1). Glaucophane, calcite, and quartz mineral and stretching
 355 lineations are oriented parallel to F_T fold hinge lines (Fig. 4C,I,J). Along Kampos Belt,
 356 D_{T1} fold axes span $\sim 335\text{-}055^\circ/15\text{-}45^\circ$, with a cluster of moderately N-plunging folds (e.g.,
 357 Fig. 4C). At Azolimnos, D_{T1} folding locally develops an upright crenulation cleavage (S_T)
 358 that cuts the S_S foliation (Fig. 4I,J; 5G). Cm-scale spaced cleavages are parasitic to larger
 359 open folds with $045^\circ/5\text{-}10^\circ$ fold axes and steep axial planes. At Azolimnos, glaucophane
 360 lineations define a great circle and swing from N to NE into alignment with F_{T1} crenulation
 361 hinge lines (Fig. 5H). Crenulation of Kini rocks is defined by a vertical, NE-striking S_{T1}
 362 cleavage that cross-cuts mafic blueschists (Fig. 4E).

363 D_{T2} is characterized by E-W orientated mineral and stretching lineations that are pri-
 364 marily indicative of greenschist facies conditions (e.g., Lotos, Delfini; Fig. 4D,F) but locally
 365 preserve blueschist facies conditions where strain was highly non-coaxial (i.e., Fabrikas; Figs.
 366 4K, 5J), and can be seen in a wide range of rock types throughout central and southern Sy-
 367 ros. At Vaporia, the mafic blueschists and eclogites and the surrounding meta-sedimentary
 368 rocks develop identical D_{T2} structures (Fig. 4G,H). Single greenschist facies F_{T2} folds range
 369 in geometry from open to tight and have near-vertical, E-NE- to E-W striking axial planes.
 370 F_{T2} fold axes cluster strongly around $\sim 070\text{-}110^\circ/5\text{-}30^\circ$ (Figs. 4D,F; 5I,K), and mineral
 371 and stretching lineations defined by actinolite, quartz, calcite, and relict glaucophane are
 372 oriented parallel to F_{T2} hinge lines (Fig. 4 D,F,H). Older S_S foliations are progressively
 373 reworked during D_{T2} creating a composite retrogressed foliation which is visible as S- and
 374 Z-folds (e.g., Fig. 5I,K) with hinge-limb layer thickness variations locally exceeding 20:1
 375 (Fig. C1). F_{T2} folds have axial planar cleavages decorated with actinolite, epidote, and
 376 chlorite. Coaxial stretching parallel to F_{T2} fold hinges is common, resulting in semi-brittle
 377 to brittle boudinage of epidote-rich lenses visible from the meso- to the micro-scale, as
 378 competent lithologies become brittle during exhumation (Fig. 5L). At Delfini, shear sense
 379 clast counting of a carbonate meta-conglomerate (GPS: $37^\circ 27' 36''$ N/ $024^\circ 53' 46''$ E) reveals

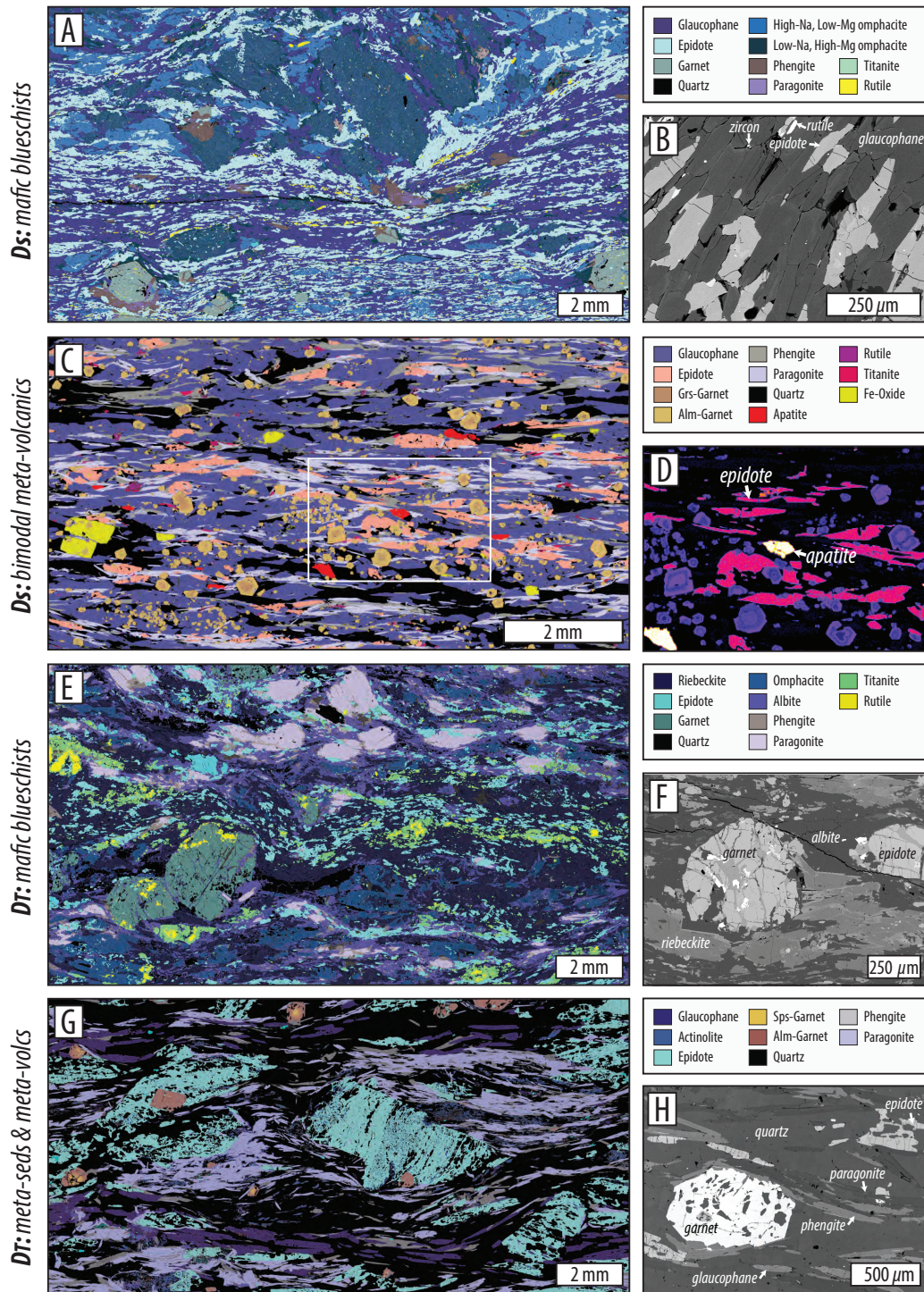


Figure 7: False-colored X-Ray maps and representative BSE images of D_S in Kini blueschists (A,B) and Azolimnos bimodal meta-volcanics (C,D), D_{T1} in Kalamisia blueschists (E,F), and D_{T2} in Fabrikas quartz-mica schists (G,H). Quantitative analyses of sodic amphiboles in (B, KCS53) and (F, KCS12B) are shown in Fig. 8; white mica analyses from (H, KCS65) are shown in Fig. B1.

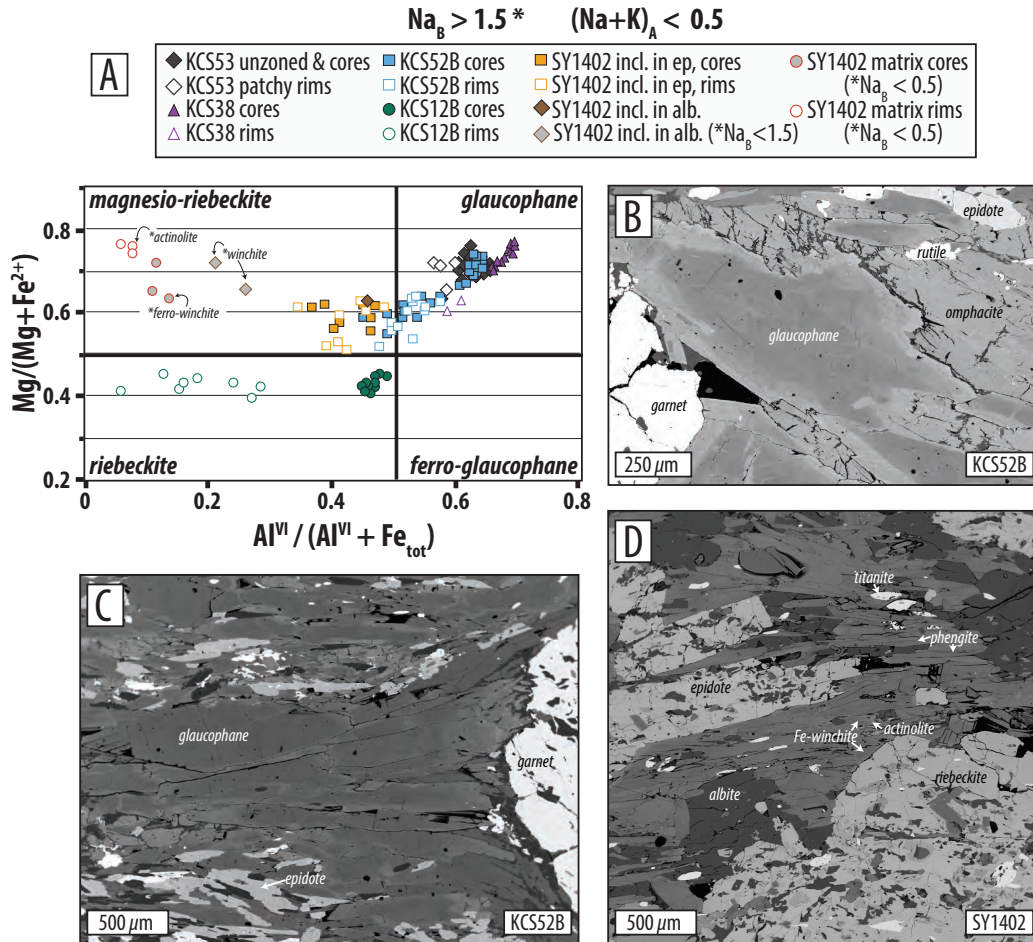


Figure 8: Amphibole mineral chemistry and micro-textures. (A) Quantitative amphibole EPMA analyses (Leake et al. (1997) classification scheme). All analyses have $\text{Na}_B > 1.5$ apfu except for those indicated with an asterisk. (B) D_{T1} static growth zonation in glaucophane contained in retrogressed eclogite pod. (C) D_{T1} lineation-parallel zonation developed in glaucophane-filled strain shadow fringing garnet porphyroclasts. (D) Greenschists preserve relict D_{T1} sodic amphibole as inclusions in epidote, and matrix amphibole records lineation-parallel compositional changes during D_{T2} retrogression.

380 conflicting and/or ambiguous shear sense. This is indicative of dominantly coaxial strain
 381 during reworking of a composite foliation that develops syn-kinematically with respect to
 382 upright folding (cf. Supplemental Fig. C1).

383 Pulses of D_T metamorphism that are not associated with penetrative strain are seen
 384 at Vaporia where pinched eclogite pods are rimmed by roughly even-thickness inky blue
 385 coronas of glaucophane (Fig. 5E), and along Kampos Belt where the margins of meta-
 386 gabbros develop radiating clusters of blue and green amphibole needles (Fig. C1). Although
 387 D_T strain is primarily coaxial, strongly asymmetric strain occurs locally on the E-SE side
 388 of the island. Non-coaxial D_{T1-2} is best preserved at Kalamisia and Fabrikas, respectively.
 389 At Fabrikas for example, outcrop-scale extensional shear bands and boudinage cross-cut
 390 eclogite pods and are decorated by glaucophane (partially replaced by actinolite) and quartz
 391 (Kotowski & Behr, 2019; Laurent et al., 2016).

392 5.3.2 D_T Microstructures and Mineral Chemistry

393 D_{T1} microstructures transpose and retrogress older S_S foliations, record geochemical
 394 evidence for retrogression through primarily blueschist facies conditions, and are primarily
 395 coaxial. Crenulation hinges that record D_{T1} in mafic blueschists are defined by high-Si
 396 white mica and glaucophane that has an identical composition to glaucophane defining the
 397 S_S foliation (Lia Beach, Fig. 6E; Fig. B1). Coaxial D_{T1} deformation in mafic blueschists is
 398 evidenced by symmetric strain shadows around partially chloritized garnets. During D_{T1} ,
 399 S_S -defining blue amphibole grows in the symmetric strain shadows and records lineation-
 400 parallel growth zonations trending from glaucophane to magnesio-riebeckite (Vaporia, Fig.
 401 8A,C) and locally becomes actinolitic (e.g., Kampos, Fig. 6G). Some static textures record
 402 the same compositional trend (e.g., Fig. 8A,B). At Kalamisia, extensional C-C' fabrics are
 403 well-developed in thin section, and C' top-to-the-ENE shear bands are decorated with albite,
 404 paragonite, and phengite (Fig. 7E,F). C' cleavages are also defined by finely recrystallized
 405 blue amphibole that records lineation-parallel core-to-rim zonations from high-Al riebeckite
 406 to low-Al (and lower $(Na+K)_A$) riebeckite (Figs. 6I, 7F, 8A). Omphacite and paragonite
 407 porphyroblasts record the breakdown reaction *omphacite + paragonite + H₂O = sodic am-*
 408 *phibole + epidote + albite* (Fig. 6I), and rutile is overgrown by syn-kinematic titanite (Figs.
 409 7E). In quartz-mica schists, the retrogressed S_S foliation comprises alternating glaucophane-
 410 rich and quartz-mica \pm albite-calcite layering; the syn- D_{T1} axial planar cleavage, S_{T1} , is
 411 defined by actinolite, albite, phengite and paragonite in the cores of upright F_{T1} folds (Fig.
 412 6H).

413 D_{T2} microstructures transpose and retrogress older S_S foliations, and are primarily
 414 coaxial and record geochemical evidence for retrogression under greenschist facies condi-
 415 tions (e.g., Delfini and Lotos). Locally D_{T2} was non-coaxial and developed under blueschist
 416 facies conditions (e.g., Fabrikas). Mafic greenschists that record D_{T2} comprise strongly
 417 retrogressed S_S foliations that are defined by fine-grained white mica, albite, epidote, acti-
 418 nolite, chlorite, calcite, and titanite (\sim 50-500 μ m grain size), and contain lineation-parallel
 419 epidote porphyroblasts (\sim 2-5 mm) and unoriented, mat-like albite porphyroblasts (\sim 1-5
 420 mm) (Fig. 6J,K). Amphibole occurs in two distinct contexts: as inclusions in epidote and
 421 albite porphyroblasts, and as a dominant S_S foliation-forming phase. Amphibole inclusions
 422 record core-rim zonations evolving from magnesio-riebeckite to winchite, and matrix am-
 423 phibole record core-rim zonations evolving from ferro-winchite to actinolite (Figs. 8A,D).
 424 S_S -defining, syn- D_{T2} epidote porphyroblasts have pressure shadows filled with white mica,
 425 calcite and albite, and are boudinaged, with necks filled by quartz and calcite (Fig. 6J,
 426 8D). In blueschist facies fabrics at Fabrikas, the retrogressed S_S foliation comprises syn-
 427 D_{T2} epidote porphyroblasts that contain rotated inclusion trails of quartz and glaucophane
 428 and inclusions of garnet that preserve syn- D_S spessartine-to-almandine zonations (Figs.
 429 7G,H). Phengite and paragonite define C- and C'-planes of an extensional, top-to-the-E
 430 shear fabric. Phengitic white mica reveals a tight range of Si atoms p.f.u. (\sim 3.33-3.39
 431 a.p.f.u, Fig. B1), and Si content of C- and C'-defining phengite is identical (Fig. 7G, Fig.

432 B1). Lineation-parallel brittle micro-boudinage of epidote and amphibole porphyroblasts
 433 is common; epidote boudin necks are filled with quartz, and blue amphibole boudin necks
 434 contain green amphibole needles. A planar S_{T2} fabric that cuts S_S is only found in the core
 435 of F_{T2} folds (i.e., S_{T2} crenulation cleavage at Delfini, Cisneros et al. (in press)).

436 6 Geochronology

437 6.1 New multi-mineral Rb-Sr isochron petrochronology

438 All of the isochrons described herein have Mean Standard Weighted Deviations (MSWDs)
 439 greater than 1, which suggests that the data dispersion exceeds that predicted by analytical
 440 uncertainties (i.e., the data are overdispersed) (Wendt & Carl, 1991). However, MSWDs are
 441 a reflection of analytical precision (e.g., Kullerud, 1991; Powell et al., 2002), and reflect the
 442 goodness of fit of a regression line to the datapoints, which includes their analytical uncer-
 443 tainties. Our dataset has a very high analytical precision (calculated from reproducibility
 444 of standards measurements), which leads to a significant increase in the MSWD of a Rb-Sr
 445 isochron when the regression line does pass through a datapoint's uncertainties (e.g., Fig.
 446 9B). However, we consider our Rb-Sr ages reliable records of true deformation and meta-
 447 morphism events, after closer evaluation of our isochrons (see Table A1), despite their high
 448 MSWDs. This is because the isochrons were constructed from mineral suites that our struc-
 449 tural and petrographic observations suggest are co-genetic, and the co-linearity of the data
 450 are striking (with some justifiable exceptions discussed below). The high MSWD values may
 451 reflect underestimation of our analytical uncertainties, or minor Rb-Sr disequilibrium during
 452 metamorphism (perhaps due to incomplete recrystallization, e.g., Halama et al. (2018)) that
 453 does not significantly affect our Rb-Sr ages (Table A1).

454 Sample SY1616 is an omphacite-blueschist collected at Kini Beach and records D_S
 455 (texturally identical to Fig. 7A). This sample yielded an age of 53.48 ± 0.65 Ma (MSWD =
 456 5) based on a 10-point isochron defined by epidote, glaucophane, omphacite, five paragonite
 457 separates, garnet, and one phengite separate (Table 2, Fig. 9). To test the robustness of
 458 the isochron, several two- to five-point isochrons were calculated from combinations of the
 459 co-genetic phases; the age does not change but the MSWD is reduced (=1 for 2-pt isochrons
 460 by definition; <1 for 3- and 4-pt, and 1.4-1.7 for 5-pt).

461 Sample KCS1617 is a bimodal meta-volcanic schist collected at Azolimnos and records
 462 D_{T1} (similar to sample in Fig. 7C). This sample yielded an age of 45.51 ± 0.29 Ma (MSWD
 463 = 8) based on a 7-point isochron defined by glaucophane, four paragonite separates, and
 464 two phengite separates (Table 2, Fig. 9). Two garnet separates fell off of the isochron and
 465 are discarded in the age calculation. We justify this based on microstructural observations
 466 shown in Figure 7D; garnets preserve complex Ca-zonation patterns and may record pulsed
 467 growth. Furthermore, garnets are D_S porphyroblasts and are not expected to be in isotopic
 468 equilibrium with the D_{T1} fabric during incipient retrogression. Previous work suggests that
 469 Sr isotopic zoning in garnets (Sousa et al., 2013) and/or isotopic inheritance from earlier
 470 stages of metamorphism and poor homogenization during subsequent stages of metamor-
 471 phism (Romer & Rotzler, 2011) tend to make garnets poor candidates for constructing
 472 Rb-Sr isochrons. Adding epidote to the isochron does not change the age (45.43 ± 0.46
 473 Ma, $n=8$), but increases the MSWD to 23. Epidote is stable throughout subduction and
 474 exhumation and could record subtle zonations that grew during subsequent deformation
 475 events and therefore may not be co-genetic (e.g., Cisneros et al., in press).

476 Sample KCS1621 is a quartz-mica schist collected from Delfini and records D_{T2} in
 477 meta-sedimentary schists. It was collected from a fold limb of a structure like the one in
 478 Fig. 5I, and is interlayered with quartz-schists on the decimeter-scale that locally preserve
 479 blue amphibole lineations. This sample yielded an age of 37.06 ± 0.12 Ma (MSWD =
 480 13) based on a 7-point isochron defined by epidote, chlorite, 3 paragonite separates, and
 481 2 phengite separates (Table 2, Fig. 9). For this sample, various combinations of 2- to

Sample ID and Summary	Mineral	Rb (ppm)	Sr (ppm)	$^{87}\text{Rb}/^{86}\text{Sr}$	$\pm 2\sigma$	$^{87}\text{Sr}/^{86}\text{Sr}$	$\pm 2\sigma$		
SY1616: Kini omphacite-epidote blueschist Solution on 10 points: $53.48 \pm 0.65 \text{ Ma}$ Initial $^{87}\text{Rb}/^{86}\text{Sr}$: 0.703211 ± 0.000012 MSWD = 5	epidote (L18-001)	0.12	1008	0.00035	1.73E-07	0.703224	1.41E-05		
	glaucophanite (L18-010)	0.15	143	0.00301	1.50E-06	0.703225	1.41E-05		
	omphacite (L19-099)	0.28	31	0.02571	1.29E-05	0.703235	1.41E-05		
	paragonite (L19-097)	0.31	19	0.04765	2.38E-05	0.703244	1.41E-05		
	paragonite (L19-093)	0.31	16	0.05829	2.91E-05	0.703234	1.41E-05		
	paragonite, 0.5 A, 125-250 μm (L19-009)	0.37	17	0.06439	3.22E-05	0.703284	1.41E-05		
	gamet #1 (L18-011)	0.29	13	0.06562	3.28E-05	0.703261	2.04E-05		
	paragonite (L19-094)	1	44	0.07644	3.82E-05	0.703248	1.41E-05		
	paragonite (L19-096)	6	142	0.12305	6.15E-05	0.703289	1.41E-05		
	phengite, 0.4 A, 250-500 μm (L19-095)	35	24	4.26296	2.13E-03	0.706398	1.41E-05		
	<i>removed from isochron</i>								
	gamet #2 (L19-098)	0.35	12	0.08338	4.17E-05	0.703353	1.41E-05		
	KCS1617: Azolinnos glaucophane-mica blueschist Solution on 7 points: $45.51 \pm 0.29 \text{ Ma}$ Initial $^{87}\text{Rb}/^{86}\text{Sr}$: 0.706592 ± 0.000022 MSWD = 8	paragonite (L19-103)	9	199	0.13309	6.65E-05	0.706681	1.41E-05	
		paragonite (L19-102)	15	179	0.23810	1.19E-04	0.706776	1.41E-05	
glaucophane (L18-002)		0.3	3	0.33478	1.67E-04	0.706783	1.41E-05		
paragonite (L19-100)		34	178	0.55161	2.76E-04	0.706927	1.41E-05		
paragonite, 0.8 A, 125-250 μm (L18-007)		5	14	0.97194	4.86E-04	0.707200	1.41E-05		
phengite (L19-101)		112	112	2.87985	1.44E-03	0.708433	1.42E-05		
phengite, 0.7 A, 250-500 μm (L18-005)		219	43	14.89794	7.45E-03	0.716067	1.43E-05		
<i>removed from isochron</i>									
epidote (L18-003)		0.7	1486	0.00136	6.82E-07	0.706668	1.41E-05		
gamet #1 (L19-004)		0.69	8	0.26530	1.33E-04	0.706583	1.41E-05		
gamet #2 (L19-104)		0.87	4	0.63469	3.17E-04	0.706733	1.41E-05		
KCS1621: Delfini actinolite-mica greenschist Solution on 7 points: $37.06 \pm 0.12 \text{ Ma}$ Initial $^{87}\text{Rb}/^{86}\text{Sr}$: 0.706626 ± 0.000033 MSWD = 13		epidote	1	1961	0.00143	5.71E-07	0.706597	1.41E-05	
		paragonite, 0.6 A, 250-500 μm (L19-225)	54	258	0.60594	2.42E-04	0.706951	1.41E-05	
		paragonite, 0.5 A, 125-250 μm (L19-222)	326	39	2.37806	9.51E-04	0.707878	1.42E-05	
	chlorite, 0.25 A, 250-500 μm (L19-226)	9	11	2.41488	9.66E-04	0.707852	1.42E-05		
	paragonite, 0.6 A, 125-250 μm (L19-224)	150	155	2.79655	1.12E-03	0.708052	1.42E-05		
	phengite, 0.5 A, 125-250 μm (L19-223)	142	173	24.45665	9.78E-03	0.719330	1.44E-05		
	phengite, 0.4 A, 250-500 μm (L19-221)	369	21	51.64803	2.07E-02	0.733354	1.47E-05		
	<i>removed from isochron</i>								
	phengite, 0.4 A, 125-250 μm (L19-220)	343	47	21.16233	8.46E-03	0.717173	1.43E-05		
	SY1644: Delfini mineralization in epidosite boudin neck Solution on 3 points: $36.05 \pm 2.6 \text{ Ma}$ Initial $^{87}\text{Rb}/^{86}\text{Sr}$: 0.706655 ± 0.00058 MSWD = 82	epidote (L19-041)	0.23	2170	0.00031	1.23E-07	0.706608	1.41E-05	
		actinolite (L19-042)	17	123	0.39700	1.59E-04	0.706899	1.41E-05	
		white mica (L19-040)	303	30	29.24565	1.17E-02	0.721388	1.44E-05	
		SY1402: Lotos reaction rim around epidosite pod Solution on 5 points: $34.88 \pm 5.8 \text{ Ma}$ Initial $^{87}\text{Rb}/^{86}\text{Sr}$: 0.70455 ± 0.00363 MSWD = 76000	apatite	2	726	0.00992	5.21E-03	0.70497	8.10E-06
			white mica < 125 μm (L19-029)	204	13	47.20997	1.89E-02	0.72438	1.45E-05
white mica 125-250 μm (L19-030)			227	10	68.82184	2.75E-02	0.73953	1.48E-05	
white mica, 0.4 A, 250-500 μm (L19-031)			234	7	95.01809	3.80E-02	0.75342	1.51E-05	
white mica, 0.6 A, 250-500 μm (L19-032)			203	9	67.84958	2.71E-02	0.73643	1.47E-05	

Table 2: Summary of Rb and Sr concentrations and measured ratios from analyzed samples. Mineral separates discarded from calculated isochrons are listed. Uncertainty in age estimate (i.e., $\pm t$) are calculated assuming overdispersion, as $z = y \times \sqrt{MSWD}$, where y is the confidence interval for t using the appropriate number of degrees of freedom.

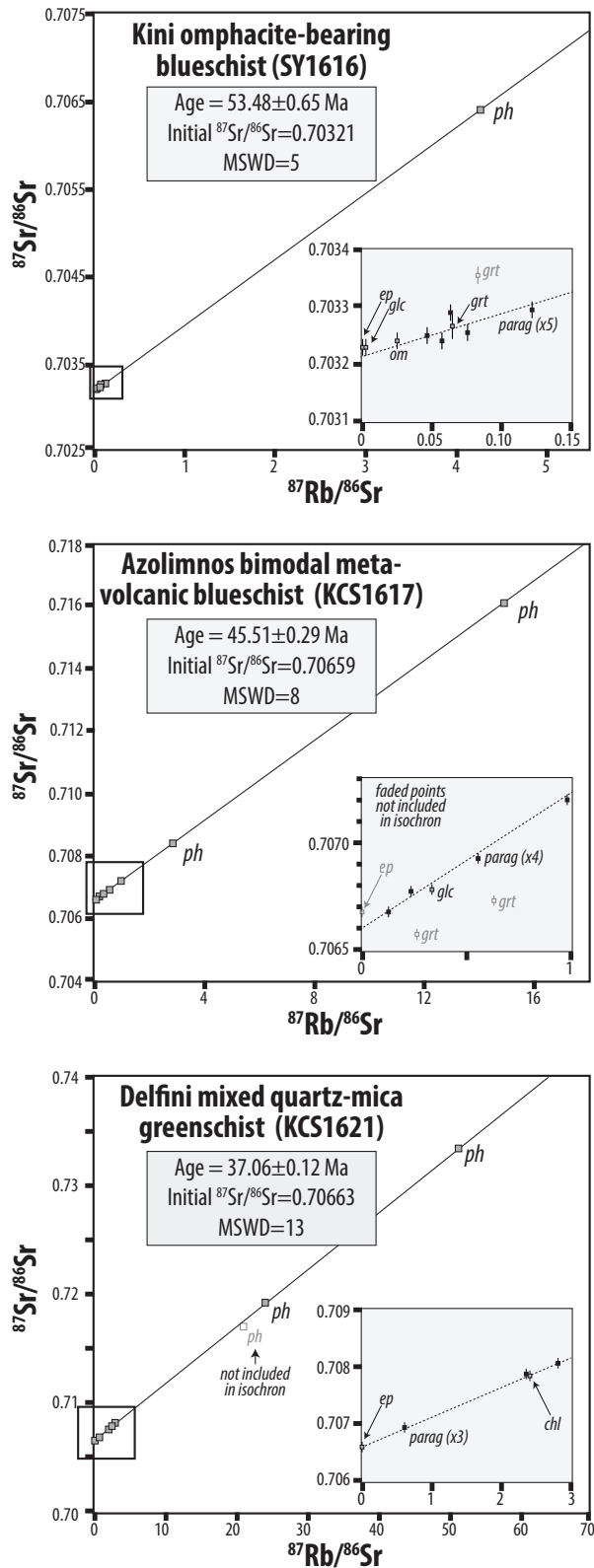


Figure 9: Multi-mineral Rb-Sr isochrons from a Kiny omphacite-blueschist (SY1616), Azolimnos quartz-mica blueschist (KCS1617), and Delfini quartz-mica greenschist (KCS1621). Grey insets are zoom-ins of low Rb/Sr separates outlined in black boxes. Faded grey symbols were excluded from isochron calculations. Multiple paragonite separates for each isochron are shown in black symbols. Sample SY1616 records D_S in the northern nappe, KCS1617 records D_{T1} in the central nappe, and KCS1621 records D_{T2} in the central nappe. D_T retrogression pre-dates the onset of regional core complex capture. Mineral abbreviations: ep = epidote, glc = glaucophane, om = omphacite, grt = garnet, parag = paragonite, ph = phengite, chl = chlorite.

482 6-pt isochrons all yield ages of $\sim 35\text{-}37$ Ma with MSWD varying from $\ll 1$ (e.g., 3-pt
 483 epidote-chlorite-paragonite), to 1 (e.g., 2-pt paragonite-chlorite) to 21 (e.g., 4-pt epidote-
 484 chlorite-phengite-phengite). Even the isochrons that are not defined in high-Rb space (i.e.,
 485 do not contain phengite) yield nearly identical ages to the 7-point isochron (Table A1).

486 Sample SY1644 is a collection of minerals precipitated in the neck of a brittlely-
 487 boudinaged epidote-rich lens from Delfini, and sample SY1402 is a greenschist facies reaction
 488 rind at the margin of an epidote-rich lens from Lotos. These samples are representative of
 489 semi-brittle boudinage associated with D_{T2} stretching (e.g., Fig. 5L). These samples yield
 490 ages with reasonable uncertainties, but extremely high MSWDs. Sample SY1644 yielded
 491 an age of 36.1 ± 2.6 Ma (MSWD = 82) based on a 3-point isochron defined by epidote,
 492 actinolite, and phengite, and sample SY1402 yielded an age of 34.9 ± 5.8 Ma (MSWD =
 493 76000) based on a 5-point isochron defined by apatite and 4 phengites (Table 2). For both
 494 samples, 2-pt isochrons yield ~ 36 Ma and $\sim 29\text{-}36$ Ma, respectively (MSWD=1; Table A1).
 495 We consider these data qualitative, but these ages are similar to and trend slightly younger
 496 than KCS1621, which is consistent with our structural observations.

497 6.2 Synthesis of previously published metamorphic geochronology

498 We compiled all available metamorphic geochronology (to our knowledge, from 1987
 499 through 2019) for Syros, and took inventory of the descriptions of deformation fabrics and
 500 metamorphic textures provided by the authors, to re-evaluate the significance of Eocene ages
 501 in the context of subduction vs. exhumation. A full compilation is shown in Supplementary
 502 Figure A1 and Table A2. We applied several qualitative filters to the dataset to derive a
 503 subset of ages that we can confidently attribute to fabric-forming events. The filters are
 504 justified as follows:

505 *Zircon U-Pb* ages are robust records of igneous crystallization, but as metamorphic
 506 ages, can be difficult to place in pro- or retrograde context (Liu et al., 2006; Tomaschek et
 507 al., 2003; Yakymchuk et al., 2017). We include U-Pb ages from Tomaschek et al. (2003)
 508 for comparison with other ages, but we do not rely on it for island-scale interpretations.
 509 *Garnet Lu-Hf and Sm-Nd* are considered reliable indicators of ‘peak’ subduction ages (i.e.,
 510 maximum depths) (Kendall, 2016; Lagos et al., 2007), because HP/LT garnets tend to grow
 511 rapidly following reaction overstepping (Baxter & Caddick, 2013; Dragovic et al., 2012,
 512 2015). Kendall (2016) and Lagos et al. (2007) both reported evidence for rapid, pulsed
 513 garnet growth near peak conditions, in the form of overlapping ‘bulk’ and ‘rim’ Sm-Nd
 514 ages, and tight clustering of Lu-Hf ages even though samples exhibited different Lu zoning
 515 profiles and distributions between their cores and rims, respectively (see also Skora et al.
 516 (2006)). This refutes the possibility that garnet cores grew significantly earlier than their
 517 rims somewhere along the prograde path. One garnet age from Kini reported by Kendall
 518 (2016) was removed from the final compilation because of its extremely low radiogenic
 519 component and therefore large uncertainty.

520 *White mica Ar/Ar* has potential to capture timing of metamorphism during fabric
 521 development. However, this system is highly susceptible to disequilibrium, partial (re-)
 522 crystallization and mixed ages, and/or unpredictable loss or gain of radiogenic products,
 523 making it difficult to interpret the geological significance of an age (Bröcker et al., 2013;
 524 Laurent et al., 2016; Lister & Forster, 2016; Maluski et al., 1987). For the final dataset, we
 525 only included five Ar/Ar step-heating ages with strong plateaus from micro-drilled grains
 526 which all had clear micro-textural context (Laurent et al., 2017), and one strong plateau
 527 age from a well-characterized marble shear zone (Rogowitz et al., 2014). We acknowledge
 528 that in other HP terranes, even strong plateau ages have been previously attributed to
 529 excess Ar (Sherlock & Arnaud, 1999). However, the Ar ages included in this study over-
 530 lap within reported error of independent Rb-Sr isochrons from rocks at the same locality
 531 and/or similar structural levels, which suggests that at least locally, excess Ar is absent
 532 (or apparently absent; cf. Ruffet et al. (1995)). *Rb-Sr isochrons* are typically considered

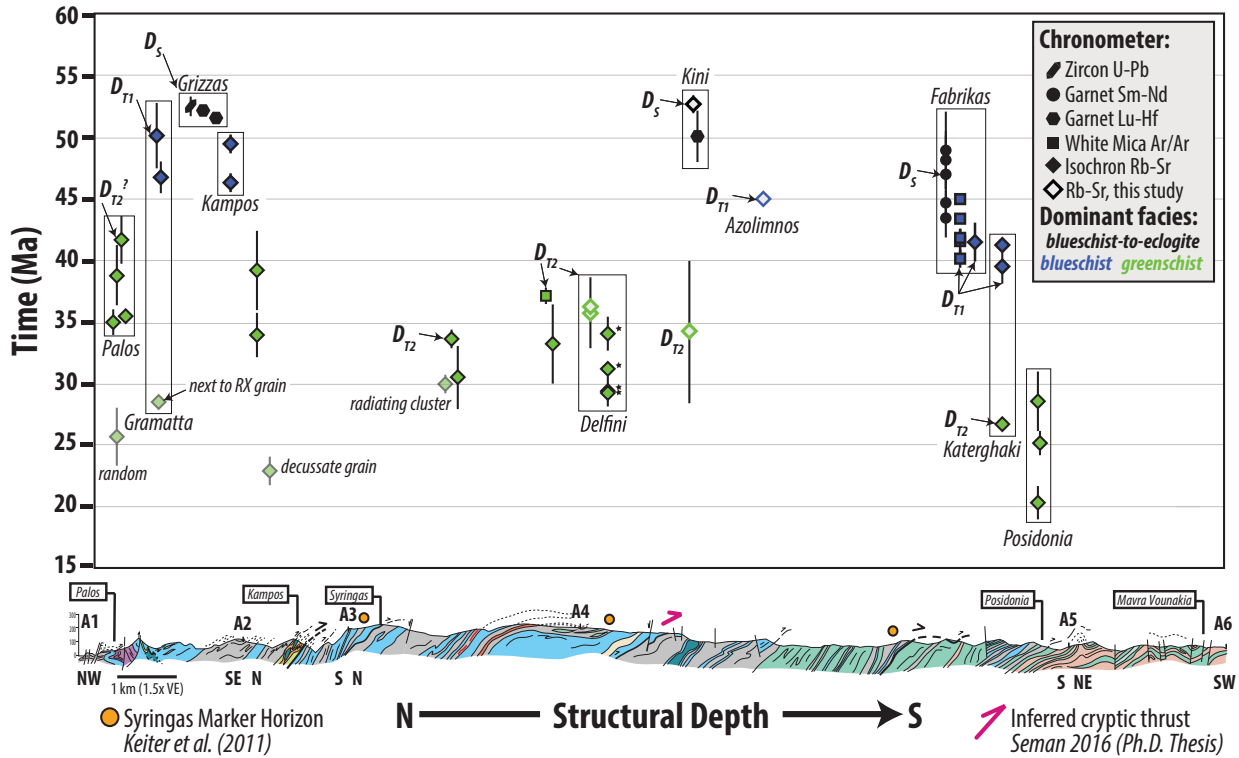


Figure 10: Metamorphic age vs. structural depth for the Syros nappe stack. The cross-section line A1-A6 is shown in Figure 2 and modified from Keiter et al. (2011). Only locations that crop out on the cross section line are labeled in white boxes; in the upper panel, other locations are indicated that project into or out of the page at the structural level shown (e.g. Kini is a normal fault-bounded block on the west side of the island and therefore is not shown on the cross section). Only ages that were confidently linked to the deformation scheme outlined in this paper are included. Clusters of ages outlined in black boxes are derived from the same locality, and collapse onto a single point on the cross section. Delfini symbols marked with stars were reported as blueschist-facies fabrics by Cliff et al. (2016); however, local preservation of glaucophane under greenschist facies conditions can be due to CO₂-bearing fluids. Pink half arrows mark the locations of inferred imbricate ductile thrusts; black half arrows indicate interpreted nappe-delimiting ductile shear zones, which were likely reworked as extensional structures during exhumation.

533 good indicators of fabric ages when the selected fabrics, and minerals defining them, are
 534 well-characterized (Bröcker & Enders, 2001; Bröcker et al., 2013; Skelton et al., 2019). Fur-
 535 thermore, constructing a Rb-Sr isochron directly tests the assumption that selected minerals
 536 were in isotopic equilibrium during metamorphism, which validates interpretation of Rb-Sr
 537 ages as deformation-metamorphism events. Micro-drilling of white micas and co-genetic
 538 Sr-rich phases (epidote or calcite) also provide strong textural context for regressed ages
 539 (Cliff et al., 2016).

540 In some cases, we propose different interpretations of published data based on our own
 541 structural observations. Skelton et al. (2019), for example, interpreted three of their Rb-Sr
 542 isochrons from Fabrikas as peak metamorphic ages (i.e., D_S), but we interpret Fabrikas
 543 fabrics to relate to D_{T1-2} , associated with early exhumation (cf. Fig. 4K). This revised
 544 interpretation is supported by previous petrologic observations of eclogite breakdown to

blueschist, replacement of glaucophane by actinolite, and core-to-rim decrease in celadonite component of foliation-forming phengitic white mica (Kotowski & Behr, 2019; Laurent et al., 2018) (see also Fig. 7), and structural studies that interpret Fabrikas to record dominantly extensional top-to-the-E, exhumation-related deformation immediately beneath the Vari Detachment. Furthermore, top-E extensional kinematics at Fabrikas clearly contrast with other localities where prograde, top-S-SW deformation is preserved (compare stereonet for Kini with Fabrikas in Fig. 4). Cliff et al. (2016) analyzed micro-drilled phengites from blueschist-to-greenschist facies (i.e., D_{T1} to D_{T2}) extensional fabrics in calc-schists and quartz-mica schists. Four of their samples from Delfini were described as blueschist-facies (black stars in Fig. 10); however, our observations point to penetrative greenschist facies deformation at Delfini (D_{T2}). Glaucophane is locally preserved in abundance in calc-schists at Delfini, and elsewhere on Syros. Rather than reflecting blueschist facies conditions during deformation, this could be due to a glaucophane-stabilizing, CO_2 -bearing fluid under greenschist facies P-T conditions (Kleine et al., 2014), or channelized fluid flow at lithological boundaries leading to heterogeneous retrogression (Breeding et al., 2003). Finally, Rogowitz et al. (2014) dated phengites from a top-E extensional greenschist facies marble shear zone, and hypothesized the ages would be Miocene in accordance with the regional ‘M2’. They interpreted their Eocene ages as evidence that Miocene deformation did not reset the isotopic signature. However, our results suggest their ages capture a true Eocene recrystallization event (e.g., strong E-W stretching during greenschist facies D_{T2}).

In Figure 10, the refined compilation ($n=43$) and new Rb-Sr geochronology ($n=5$) are projected onto the cross-section line drawn in Figure 2. Where possible, ages are labeled according to fabric generation. Faded data points were assigned textural identities but do not record penetrative strain (e.g., randomly oriented, radiating cluster). Key observations from new and compiled geochronology include:

1. D_S , blueschist-to-eclogite facies deformation-metamorphism spans ~ 53 to ~ 45 Ma, and is captured by a multi-mineral Rb-Sr isochron (this study, Kini), and Lu-Hf and Sm-Nd garnet ages
2. D_S ages are oldest and well-clustered at Grizzas and Kini (~ 53 - 52 Ma), and younger and potentially more widespread at Fabrikas (~ 48 - 42 Ma).
3. D_{T1} , retrograde blueschist facies deformation-metamorphism spans ~ 50 - 40 Ma (Rb-Sr isochrons and Ar/Ar single grain analyses) and youngs with structural depth, i.e., from Kampos, to Azolimnos, to Fabrikas.
4. D_{T2} , retrograde greenschist facies deformation-metamorphism spans ~ 42 - 20 Ma (all Rb-Sr) and youngs with structural depth, i.e., from Palos (~ 43 - 35 Ma), to Delfini (~ 35 - 28 Ma), to Posidonia (~ 28 - 20 Ma).
5. Rocks that presently occupy different structural levels developed distinct fabric generations contemporaneously. Examples include: Fabrikas D_S and Kampos D_{T1} (~ 50 - 45 Ma), Fabrikas D_{T1} and Palos D_{T2} (~ 43 - 38 Ma), and Posidonia D_{T2} and non-penetrative greenschist metamorphism in the north (faded symbols, ~ 25 - 20 Ma). In other words, retrograde blueschist and greenschist facies deformation-metamorphism occurred first in the structurally highest units and progressed structurally downwards with time.

7 Synthesis of structural and petrologic data and interpreted Deformation-Metamorphism history

7.1 D_R P-T conditions

We interpret the D_R fabric as the oldest recognizable in the CBU, and that it formed under lawsonite-blueschist facies conditions based on several lines of evidence: (1) D_R inclusion trail mineralogy (e.g., glaucophane, omphacite, phengite); (2) pseudomorphs of D_{R-S} lawsonite included in D_S garnets from meta-basites on Syros (also seen on Sifnos) (Okrusch

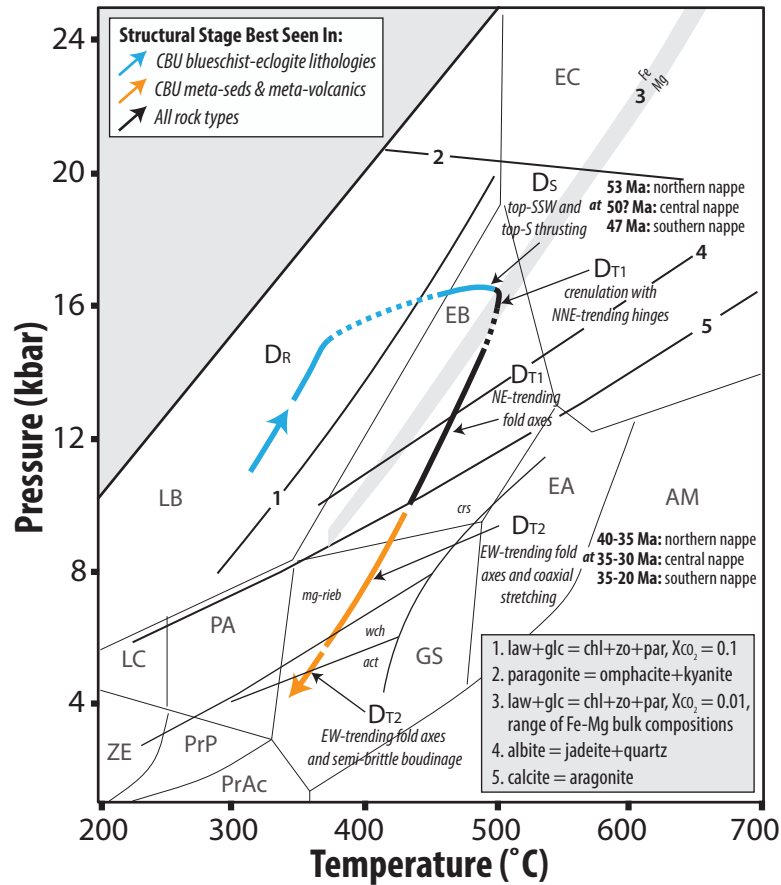


Figure 11: Preferred, schematic P-T-D-t path for the CBU, consistent with observations and analytical results from this study. The shape of the path is modified from Schumacher et al. (2008). Amphibole stability fields constraining D_{T2} temperatures are from Otsuki and Banno (1990). The timing of metamorphism labeled along the P-T loop corresponds to progressive subduction and exhumation of three distinct tectonic slices (the northern, central, and southern nappes; see Sections 6, 7 and Fig. 10). Mineral abbreviations: crs = crossite (sodic amphibole), mg-rieb = magnesio-riebeckite, wch = winchite, act = actinolite. Facies fields defined in Figure 3.

595 & Bröcker, 1990; Ridley, 1982); and (3) syn-kinematic D_{R-S} omphacite blasts recording
 596 up-pressure, core-to-rim zonations marked by increasing jadeite component (Fig. 7A) (cf.
 597 Thompson, 1974). Lawsonite and epidote appear to have both been stable in mafic bulk
 598 compositions during D_R , with lawsonite growing later on the prograde path under higher-
 599 pressure conditions (cf. Balleve et al., 2003). This is consistent with textural observations
 600 of lawsonite growing late, syn- and post-tectonic with respect to the S_R foliation, incorpor-
 601 ating inclusions of garnet (which also grows near peak pressures, cf. Baxter and Caddick
 602 (2013); Dragovic et al. (2012, 2015)), and being included by garnet.

603 7.2 D_S deformation and P-T conditions

604 Deformation stage D_S captures peak metamorphic conditions, and produced: (1) an
 605 axial plane schistosity, S_S , associated with tight to isoclinal folds (F_S) that fold S_R , record
 606 asymmetric top-to-the-S-SW sense of shear, and have S-SW-plunging fold axes; (2) SSW-

607 to-S-plunging mineral lineations; (3) a blueschist-to-eclogite facies fabric containing syn-
 608 kinematic garnet, omphacite, and (now pseudomorphed) lawsonite porphyroblasts; and (4)
 609 chemical zonations in glaucophane and omphacite that record syn-kinematic increase in
 610 pressure and temperature. New and compiled metamorphic geochronology demonstrate
 611 that different structural levels of the CBU on Syros experienced peak conditions and D_S
 612 deformation at different times (i.e. younging with structural depth, cf Fig. 10; discussed
 613 further below). However, it appears that each tectonic slice experienced similar P-T trajec-
 614 tories, including peak P-T, despite subducting at different times.

615 We do not provide new quantitative constraints on D_S metamorphic conditions, but
 616 peak P-T for the D_S fabric shown in Figure 11 are consistent with our petrologic obser-
 617 vations and previous studies and are justified as follows. Peak temperatures have been
 618 calculated from garnet-omphacite major element exchange for mafic blueschists and eclog-
 619 ites (450-550°C) (Laurent et al., 2018; Okrusch & Bröcker, 1990; Rosenbaum et al., 2002;
 620 Schliestedt, 1986); the upper limit of glaucophane stability in marble ($\sim 500^\circ\text{C}$ at ~ 15 -
 621 16 kbar; Schumacher et al. (2008)); and calculated lawsonite-out reactions that predict
 622 up-temperature, prograde dehydration according to the reaction $lawsonite = epidote +$
 623 $paragonite + H_2O$ at ~ 400 -500°C over ~ 12 -20 kbar (depending on bulk rock and fluid
 624 composition) (Evans, 1990; Liou, 1971; Philippon et al., 2011; Schumacher et al., 2008)
 625 (Fig. 11). Raman Spectroscopy of Carbonaceous Material from graphite schists suggests
 626 slightly higher temperatures of ~ 540 -560°C (Laurent et al., 2018). Observed porphyrob-
 627 last stability (e.g. lawsonite pseudomorph inclusions in garnets and vice versa), amphibole
 628 chemistry, and the volumetric dominance of glaucophane-bearing marbles throughout the
 629 CBU on Syros are generally consistent with peak T of ~ 500 -550°C.

630 Reported peak pressures for D_S are variable in the literature, and challenging to rec-
 631 oncile. Early conventional thermobarometry suggested peak P of ~ 12 -18 kbar in mafic
 632 blueschists and eclogites (Dixon, 1976; Okrusch et al., 1978; Okrusch & Bröcker, 1990;
 633 Schliestedt, 1986). These pressures are supported by recent solid inclusion quartz-in-garnet
 634 barometry constraining garnet growth at Kini, Kalamisia, Delfini, and Lotos to ~ 13 -17 kbar
 635 (Behr et al., 2018; Cisneros et al., in press). However, more recent thermodynamic modeling
 636 accounting for garnet fractionation suggests rocks reached ~ 22 -24 kbar (Laurent et al., 2018;
 637 Skelton et al., 2019; Trotet, Jolivet, & Vidal, 2001). We consider this unlikely based on the
 638 abundance of S_S paragonite and absence of kyanite in meta-mafic rocks, which suggests
 639 that the upper stability limit of paragonite at ~ 20 -23 kbar was not reached (Okrusch &
 640 Bröcker, 1990; Schliestedt, 1986; Skelton et al., 2019) (Fig. 11), although we acknowledge
 641 that the kyanite-in reaction is strongly dependent on bulk rock composition (cf. Laurent et
 642 al., 2018). Large differences in P-T estimates between traditional phase equilibria and recent
 643 thermodynamic modeling may reflect arbitrary choices of thin section domains selected as
 644 representative bulk compositions (e.g., Lanari & Engi, 2017). This effect has been demon-
 645 strated for CBU lithologies on Syros (see Fig. 15 in Laurent et al., 2018) and is especially
 646 likely in garnet-bearing rocks, due to the strong disequilibrium effect that garnet exerts on
 647 local bulk composition (Lanari et al., 2017; Lanari & Engi, 2017; Lanari & Duesterhoeft,
 648 2018). It is also possible that higher-P conditions are real, but have not yet been sampled
 649 by solid inclusion techniques.

650 7.3 D_T deformation and P-T conditions

651 D_T represents retrograde deformation under blueschist-to-greenschist facies conditions
 652 during exhumation. D_T is distinguished by: (1) transposition of the S_S foliation during
 653 formation of upright, open to tight F_T folds and progressive new (S_T) fabric development; (2)
 654 lineation orientations that rotate from N-NE (D_{T1}) to E-W (D_{T2}) with progressive strain and
 655 (in general) increasing greenschist facies retrogression; (3) dominantly coaxial, but locally
 656 non-coaxial deformation; and (4) chemical zonations in amphibole tracking syn-kinematic
 657 decrease in pressure and temperature during development of a composite, reworked foliation
 658 (e.g. S_S is locally deformed and metamorphosed during D_T).

659 During D_T , foliation-forming amphiboles transition from glaucophane to (magnesio)
 660 riebeckite, to winchite, to actinolite. The progressive decrease of total Al, Na_B , and
 661 $(Na+K)_A$ in amphibole indicates that P and T decreased as D_T evolved. Glaucophane
 662 coronas that develop around eclogite pods during D_{T1} are chemically similar to syn- D_S
 663 glaucophane, and retrogressed glaucophane records decreasing Al^{vi} (KCS53, KCS52B) and
 664 Na_B (KCS53) from core to rim, and a minor increase in $(Na+K)_A$ as (Fig. 8, Fig. B1).
 665 These signatures indicate decompression and potentially slight warming (Ernst & Liu, 1998;
 666 Laird & Albee, 1981; Moody et al., 1983; Raase, 1974; Robinson, 1982), at the subduction-
 667 to-exhumation transition.

668 D_{T2} is characterized by foliation-forming calcic amphiboles, and local relicts of sodic
 669 amphiboles are found as inclusions in porphyroblasts. The transition from sodic-to-calcic
 670 amphibole recorded here indicates cooling during decompression (Brown, 1977; Ernst &
 671 Liu, 1998; Laird & Albee, 1981; Maruyama et al., 1983; Moody et al., 1983; Otsuki &
 672 Banno, 1990; Schmidt, 1992; Thompson, 1974) through albite-epidote blueschist facies and
 673 eventually greenschist facies conditions (Fig. 11). This P-T trend is supported by the
 674 abundance of albite and titanite overgrowths on rutile, boudin neck quartz-calcite oxygen
 675 isotope temperatures and quartz-in-epidote inclusion barometry (Cisneros et al., in press),
 676 and decreases from core-to-rim in celadonite component of foliation-forming white micas
 677 (Laurent et al., 2018). While we cannot rule out an initial phase of isothermal decompression
 678 at high pressures, our documented amphibole geochemical zonations support cooling
 679 during decompression at moderate pressures and do not support a positive thermal excursion
 680 into the epidote-amphibolite facies field (e.g., edenite, pargasite, crossite), as suggested
 681 by Laurent et al. (2018), Lister and Forster (2016), and Trotet, Jolivet, and Vidal (2001)
 682 P-T-D paths. Notably, Aravadinou et al. (2016) reported syn-kinematic amphibole zonations
 683 from retrograde fabrics in the CBU on Sifnos that also support exhumation along a
 684 cooling-during-decompression pathway (see also Schmädicke and Will (2003)).

685 8 A new tectonic model for the CBU on Syros

686 Here we synthesize protolith age constraints, and our structural, petrologic, and geochrono-
 687 logic data, and propose a revised tectonic model for the CBU on Syros. First we present a
 688 pre-subduction configuration, then discuss a stepwise reconstruction capturing progressive
 689 subduction, underplating, and exhumation, leading to the three-part tectonic stack exposed
 690 on Syros today.

691 8.1 Pre-subduction configuration

692 Figure 12 builds on previous work (e.g., Papanikolaou, 1987, 2013; Ring et al., 2010;
 693 Van Hinsbergen et al., 2020) and illustrates a highly schematic paleogeographic setting for
 694 the CBU on Syros and Southern Cyclades immediately prior to subduction at ~ 60 Ma. Peri-
 695 Gondwanan Cycladic Basement, cross-cut by Carboniferous magmatism (~ 315 on Syros,
 696 Tomaschek et al. (2008); 330-305 in Southern Cyclades, Flansburg et al. (2019)), was rifted
 697 in the Triassic (~ 240 Ma, Keay (1998); Löwen et al. (2015)). Syn-rift bimodal volcanics
 698 and sediments intruded and blanketed the hyper-extended margin; these will become the
 699 diagnostic marker horizons referred to as banded tuffitic schists and bimodal meta-volcanics
 700 mapped by Keiter et al. (2011) (orange and dark grey in Fig. 12; cf. Fig. 2). Rifting was
 701 followed by passive margin sedimentation of psammites, debris flows, and carbonates from
 702 the Triassic (~ 230) through the Cretaceous (~ 75 Ma) (Löwen et al., 2015; Poulaki et al.,
 703 2019; Seman, 2016; Seman et al., 2017). Carbonates interbedded with clastic sediments may
 704 be the protolith for the Syringas Marker Horizon (Keiter et al., 2011). Cretaceous rifting
 705 (~ 80 Ma, Tomaschek et al. (2003)) dissected the hyper-extended basement and passive
 706 margin sedimentary sequence, forming a small oceanic-affinity (backarc?) basin (Bonneau,
 707 1984; Cooperdock et al., 2018; Fu et al., 2012; Keiter et al., 2011).

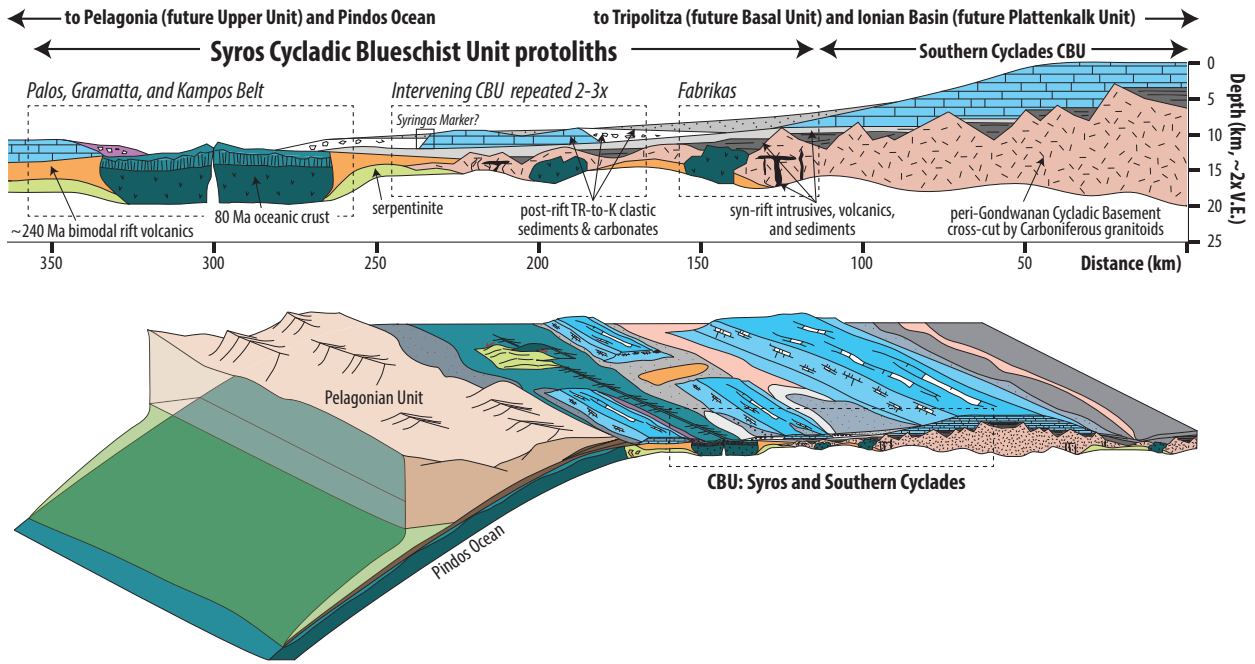


Figure 12: Schematic paleogeographic reconstruction of the CBU, with emphasis on lithologies exposed on Syros at ~ 60 Ma. The zoomed-in cross section is modified from Seman (2016). Stepwise evolution of the CBU during subduction is shown in the next figure.

708 The most interpretive part of Figure 12 is the locations of mafic igneous rocks. These
 709 rocks could reflect off-axis, shallow intrusions related to Cretaceous rifting, or older mafic
 710 igneous rocks related to Triassic rifting; protolith ages have not been determined for Kini,
 711 Vaporia, Kalamisia, or Fabrikas mafic rocks. Regardless of their origin, the key point is that
 712 protoliths for mafic blueschists and eclogites were distributed throughout the CBU before
 713 subduction, rather than only coming from the small ocean basin in the north. While the
 714 precise locations and sources of these mafic volcanics are unknown, this interpretation is
 715 supported by different ages of peak metamorphism in blueschists and eclogites that crop
 716 out at Kampos/Kini and Fabrikas (see Fig. 10 and discussion below).

717 This paleogeographic interpretation allows us to split the CBU on Syros into three
 718 sub-domains characterized by distinct, but related, protolith assemblages (dashed boxes in
 719 Fig. 12). These sub-domains are the precursors to each of three main tectonic slices that
 720 comprise the structural pile on Syros today.

721 8.2 Peak subduction of the Palos-Gramatta-Kampos nappe (~ 53 Ma)

722 The Palos-Gramatta-Kampos nappe (northern nappe) comprises Cretaceous oceanic
 723 lithosphere intruded into Triassic bimodal rift volcanics and Triassic-to-Cretaceous sedi-
 724 ments (Fig. 12). Our view of this structurally highest subunit differs from that of Laurent
 725 et al. (2016)'s 'Kampos subunit' in that it does not solely comprise meta-mafic lithologies,
 726 and it does not include the map-scale meta-mafic lenses at Vaporia, Kalamisia, and Fabrikas
 727 (see also Section 9). Garnet Lu-Hf from Grizzas and new Rb-Sr isochrons from Kini yield
 728 identical ages of D_S fabric development within error, suggesting that Kini was originally
 729 subducted as part of the northern nappe (Fig. 10), and was down-dropped by late-stage,
 730 high-angle normal faults to its present position (cf. Keiter et al., 2011; Ridley, 1984).

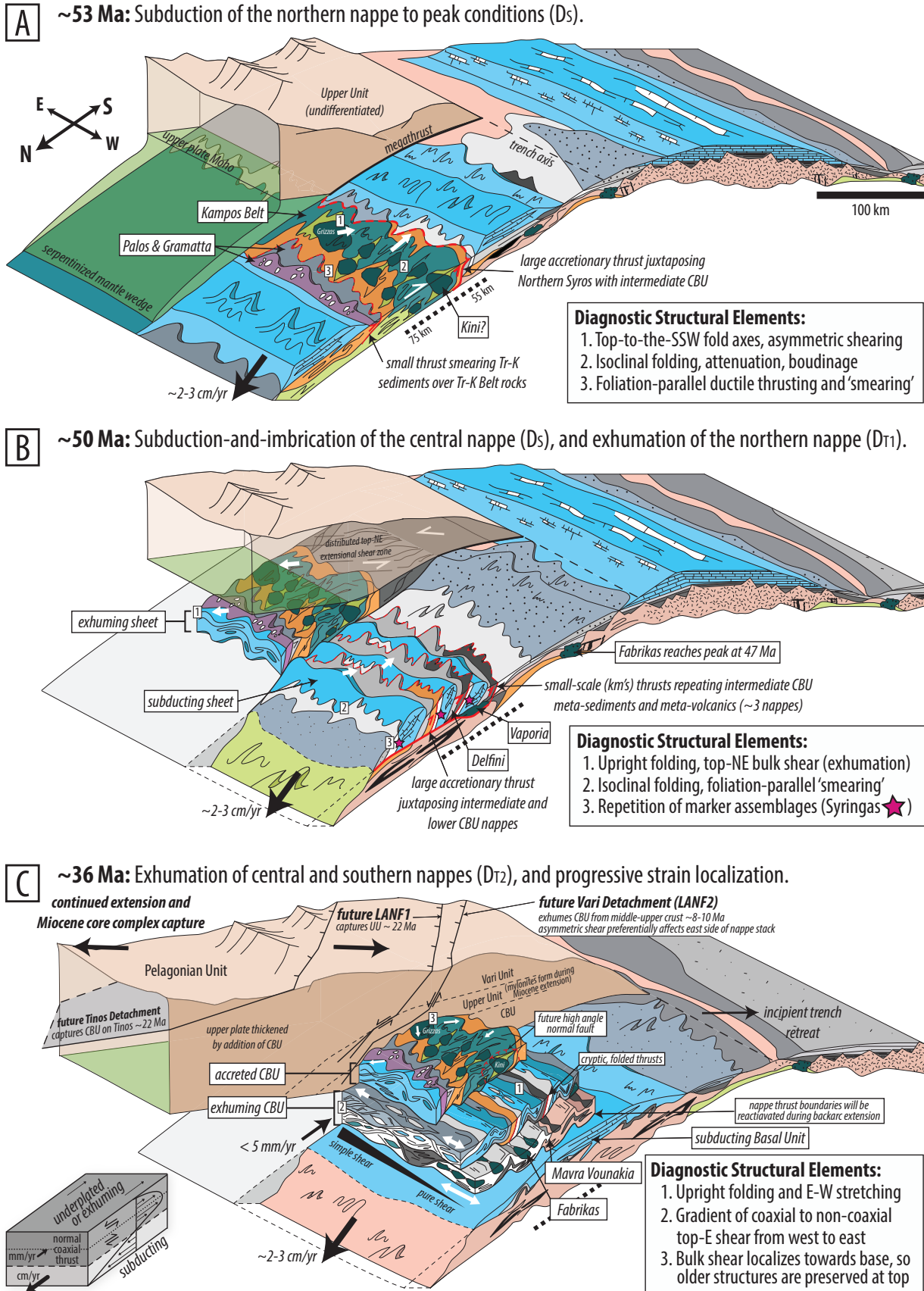


Figure 13: Caption on next page.

Figure 13: (Previous page.) Block diagrams illustrating the structural evolution and timing of subduction and exhumation recorded by the three tectonic slices in the Syros nappe stack. Compare stepwise subduction of sub-units to the paleogeography in Figure 12. Horizontal scaling is equivalent to subduction rates of $\sim 2\text{-}3$ cm/yr and diagrams are roughly 2x vertically exaggerated. The thickness of the interface is exaggerated for clarity.

731 Prograde-to-peak subduction was characterized by extremely high top-to-the-SSW
 732 asymmetric shear strain and at least two stages of foliation development under blueschist-
 733 to-eclogite-facies conditions (D_R and D_S ; Fig. 13A). Metamorphism led to the forma-
 734 tion of blueschists *and* eclogites under identical P-T conditions, reflecting differences in
 735 bulk composition and/or protolith texture (Kotowski & Behr, 2019; Skelton et al., 2019).
 736 Subduction-related strain was very heterogeneous. This is evidenced by rheologically strong
 737 meta-gabbros at Grizzas and Kini that preserve primary igneous features (Keiter et al.,
 738 2004, 2011; Kotowski & Behr, 2019; Laurent et al., 2016). Furthermore, early prograde
 739 SW-plunging fold axes and mineral lineations are preserved at Grizzas, Kini, and locally
 740 along Kampos Belt. Girdled glaucophane lineations (e.g., Kini, Kampos) record continuous
 741 kinematic rotation from SW to N-S during subduction. Top-to-the-SW and top-to-the-S
 742 asymmetric thrusting are diagnostic of subduction kinematics (Blake Jr et al., 1981; Keiter
 743 et al., 2004; Laurent et al., 2016; Philippon et al., 2011; Ridley, 1984), indicated by SW-
 744 verging thrusts on mainland Greece (Jacobshagen, 1986). Despite the extremely high shear
 745 strains during subduction, Seman (2016) was able to identify a relict young-on-old depo-
 746 sitional relationship preserved between Kampos Belt meta-igneous rocks and the overlying
 747 Gramatta meta-sedimentary package. This relationship, seen in the detrital zircon U-Pb
 748 geochronologic record, suggests that the contact between the two units has not been sub-
 749 stantially disturbed during subduction and exhumation. However, some small-offset ductile
 750 thrusting likely ‘smeared’ the Palos-Gramatta meta-sedimentary rocks along the top of
 751 Kampos Belt volcanics (e.g., small thrust in Fig. 13A).

752 The northern nappe was underplated after D_S development and before D_T exhuma-
 753 tion, removing it from the active subduction interface. Detrital zircon U-Pb data support
 754 independent structural observations that suggest a large thrust separates the northern nappe
 755 from the central nappe beneath it (Keiter et al., 2004; Laurent et al., 2016; Seman, 2016)
 756 (Fig. 13A; structurally highest black thrust in cross section in Fig. 10). This thrust
 757 placed Triassic and Cretaceous igneous rocks (Kampos) atop Cretaceous (Syringas) sedi-
 758 ments and allowed the underplated nappe to exhume, while subduction of the intermediate
 759 nappe occurred beneath it.

760 **8.3 Subduction-and-imbrication of the Syringas-Azolimnos nappe and blueschist** 761 **facies exhumation of the northern nappe (~ 50 Ma)**

762 The Syringas-Vaporio-Azolimnos nappe (central nappe) occupies the central portion
 763 of the island and comprises interbedded Triassic-to-Cretaceous meta-sedimentary schists,
 764 meta-volcanic schists, and meta-carbonates (Fig. 12). In contrast to Laurent et al. (2016)’s
 765 central Chroussa subunit, we suggest that Vaporio and Kalamisia meta-mafic lenses belong
 766 to this central slice and record primary intrusive and/or depositional relationships with
 767 surrounding CBU meta-sediments (cf. Keiter et al. (2011)). The timing of peak D_S during
 768 subduction of the central nappe is unknown, but based on this tectonic model and the
 769 well-constrained ages of peak subduction in the northern and southern nappes, it likely
 770 reached peak conditions at ~ 50 Ma (this is testable with garnet geochronology from Delfini,
 771 Vaporio, or Kalamisia). D_S in the central nappe is largely overprinted during subsequent
 772 exhumation-related deformation, but early fabrics are reminiscent of D_S in the northern
 773 nappe and similarly consist of isoclinal folds and strong cleavage development (e.g., textural

774 relicts at Azolimnos). While D_S developed in the central nappe, D_{T1} exhumation-related
 775 blueschist facies fabrics formed at the same time in the northern nappe (Fig. 10, 13B).

776 Detrital zircon U-Pb geochronology and Maximum Depositional Ages (MDAs) of meta-
 777 sedimentary rocks in the central nappe reveal several old-on-young stratigraphic inversions,
 778 which suggest imbrication occurred along cryptic ductile thrusts during subduction (Seman,
 779 2016) (pink thrusts in Fig. 10, pink stars in Fig. 13B). For example, Seman (2016) doc-
 780 umented an old-on-young stratigraphic inversion where Triassic meta-volcanics at Delfini
 781 are thrust atop Cretaceous meta-sediments east of Kini (Fig. 2). Even though these struc-
 782 tures cannot be seen in the field, the presence and locations of inferred thrusts are further
 783 supported by the repeated Syringas Marker Horizon, which never appears overturned (or-
 784 ange circles and pink stars in Fig. 10 and 13B, respectively) and repetition of Triassic
 785 bimodal meta-volcanic sequences (orange and dark grey in Figs. 2 and 13B). Thus, we
 786 propose that the central nappe is bounded by larger nappe-delimiting thrusts to its north
 787 and south, and also comprises smaller-scale thrusts accommodating internal imbrication of
 788 CBU meta-sedimentary rocks, shown in the cross section in Figures 2 and 10.

789 During peak subduction of the central nappe (D_S), D_{T1} deformation occurred in the
 790 northern nappe, and was characterized by upright folding, crenulation cleavage development,
 791 and NE-trending fold axes and mineral lineations. This kinematic transition is marked by
 792 $\sim 120\text{-}180^\circ$ rotation in dominant mineral lineations and fold axis orientations from the S-SW
 793 to the N-NE. We interpret the crenulation cleavage formed during D_{T1} to be a signature of
 794 the ‘subduction-to-exhumation transition,’ when rocks ‘turn the corner’ in the subduction
 795 channel, based on the observation that crenulation lineations are decorated by high-pressure
 796 phases with compositions similar to peak D_S blueschist-to-eclogite facies conditions (Kini,
 797 Figs. 6E). D_{T1} and subsequent strain localized in weaker CBU meta-sediments during ex-
 798 humation (e.g., Palos, Gramatta), whereas prograde subduction-related fabrics are locally
 799 preserved in rheologically strong meta-gabbros at Grizzas and Kini. These observations sup-
 800 port previous structural studies that suggest exhumation-related deformation progressively
 801 localized towards the bottom of the structural pile, leading to more pervasive greenschist
 802 facies overprints in the south of the island (Laurent et al., 2016; Lister & Forster, 2016;
 803 Ring et al., 2020).

804 The structural base of the central nappe is difficult to pinpoint. However, metamorphic
 805 geochronology suggests that it is somewhere below Azolimnos and must be above the Fab-
 806 rikas tectonostratigraphic horizon, which comprises the third and lowermost nappe. The
 807 presence of a nappe-bounding thrust is also consistent with progressive southward facies
 808 changes in the rock types, as carbonate horizons thin substantially and paragneissic mate-
 809 rial crops out at the island’s southern tip, as well as the presence of thrust fault-bounded
 810 marble klippe exposed locally on the southern portion of the island (Figs. 2 and 10). Laurent
 811 et al. (2016) traced a nappe-bounding shear zone across the island based on the observed
 812 intensity of greenschist overprinting and the disappearance of marbles, and suggested its
 813 western extent crops out as splaying shear zones above and below the Delfini peninsula (i.e.
 814 their ‘Achaldi-Delfini shear zone’). If this is the case, then new and compiled geochronol-
 815 ogy suggests that greenschist facies overprinting in the southern slice spanned $\sim 36\text{-}20$ Ma.
 816 Alternatively, if the nappe-bounding shear zone occupies a slightly deeper structural level
 817 (i.e. right beneath Delfini peninsula, such that Delfini represents the lowermost portion
 818 of the central nappe that is heavily retrogressed under greenschist facies conditions), then
 819 D_{T1-2} development in the central slice is slightly older ($\sim 35\text{-}30$ Ma) than in the south-
 820 ern slice ($\sim 30\text{-}25$ Ma). This ductile nappe-bounding structure accommodated underplating
 821 of the central nappe at ~ 50 Ma while the southern nappe was still subducting, and was
 822 subsequently reworked during exhumation.

8.4 Peak subduction of the Fabrikas nappe and blueschist facies exhumation of the central nappe ($\sim 48\text{-}43$ Ma)

The Fabrikas nappe (southern nappe) comprises Triassic meta-sedimentary schists, meta-volcanic schists, and thinner meta-carbonate horizons compared to the central nappe (cf. Keiter et al., 2011); this meta-sedimentary sequence was spatially associated with mafic igneous rocks with unknown crystallization ages (Fig. 12). The primary difference between our southern slice and Laurent et al. (2016)'s Posidonia subunit is that it contains the Fabrikas meta-mafic lens, which they placed in the structurally highest Kampos subunit. Otherwise, our structural measurements and metamorphic observations are similar. Peak subduction of the Fabrikas nappe is well-constrained at $\sim 48\text{-}43$ Ma by garnet Sm-Nd crystallization ages (Kendall, 2016). A weighted mean of Fabrikas garnet ages using Isoplot (Ludwig et al., 2010), weighted by assigned uncertainties, is 45.1 ± 2.9 Ma (2 sigma) (Fig. 10) and is distinctly younger than peak subduction at ~ 53 Ma of the northern nappe. The subduction-to-exhumation transition, or underplating event, of the southern nappe is bracketed by peak subduction recorded by garnet Sm-Nd ages and blueschist facies retrogression recorded by Rb-Sr multi mineral isochrons, and occurred somewhere between $\sim 42\text{-}39$ Ma (Skelton et al., 2019).

Between $\sim 48\text{-}45$ Ma, rocks of the central nappe exhumed in the subduction channel under blueschist facies conditions. Retrograde blueschist fabrics at Azolimnos, well-constrained at ~ 45 Ma, overlap with garnet Sm-Nd ages at Fabrikas but are older than retrograde blueschist fabrics at Fabrikas, which directly supports the separation of the central and southern tectonic slices. At this time, mafic blueschists and eclogites and surrounding meta-sedimentary schists in the central nappe developed identical D_{T1-2} structures (e.g., Vaporia and overlying meta-sedimentary rocks, and Kalamisia and Azolimnos; Fig. 4). This indicates that during D_{T1-2} , mafic blueschists and eclogites and surrounding meta-sedimentary rocks were exhumed together, and in some places, strain was partitioned between them. Therefore, even if mafic blueschists and eclogites reached higher pressures on their prograde path, they must have been partially exhumed and juxtaposed with CBU meta-sediments by ~ 45 Ma to explain concordant exhumation-related structures.

8.5 Exhumation of the Syros nappe-stack in the subduction channel under greenschist facies conditions (through ~ 20 Ma)

Between $\sim 44\text{-}20$ Ma, greenschist facies D_{T2} fabrics continuously developed throughout the accreted CBU stack, as each underplated nappe was exhumed in series from north to south. Retrograde greenschist facies deformation-metamorphism occurred first in the structurally highest northern nappe, and migrated structurally downward through time (see also Ring et al. (2020) and Roche et al. (2016)). Exhumation imparted penetrative deformation that progressively transposed older fabrics under blueschist facies (D_{T1}) and eventually greenschist facies (D_{T2}) conditions. Previous geochronology and our new Rb-Sr isochron from Delfini suggest that fabrics formed during blueschist-to-greenschist facies retrogression can be precisely dated if appropriate mineral assemblages are targeted. Furthermore, exhumation-related D_{T1} and D_{T2} strain was dominantly coaxial and well-distributed. This is evident from symmetric strain shadows on garnets, ductile pinching of partially retrogressed eclogites at Agios Dimitrios, and outcrop-scale greenschist facies folds with sub-horizontal E-W trending hinge lines with hinge-parallel symmetric boudinage of competent blueschist and epidote-rich lenses (e.g., Delfini and Lotos; Figs. 5, C1).

The youngest dynamic D_{T2} greenschist facies fabrics associated with subduction channel exhumation are $\sim 25\text{-}20$ Ma and are recorded in the southern nappe (Fig. 10). At this time, greenschist facies metamorphism continued in the northern and central nappes, but was not associated with penetrative strain (e.g., random grains, radiating clusters, decussate textures; Cliff et al. (2016)). These observations indicate strain progressively localized towards the base of the stack through time. Patchy, static metamorphism in the northern

874 and central nappes may reflect local fluid availability as deformation migrated structurally
875 downward.

876 **8.6 Upper plate extension and core complex capture**

877 Slab rollback accelerated ~ 23 -21 Ma, which is constrained by dating of detachment
878 faults and supra-detachment sedimentary basins that developed in response to upper crustal
879 extension (Gessner et al., 2013; Ring et al., 2010). Rollback led to core complex capture
880 and southward migration of the volcanic arc through the former forearc (e.g., the Tinos
881 granite, 14.6 ± 0.2 Ma, Bolhar et al. (2010)). CBU rocks were exhumed in the footwall
882 of the North and West Cycladic Detachment Systems and related smaller-scale structures
883 during ‘post-orogenic’ exhumation (Jolivet et al., 2010; Soukis & Stockli, 2013). On Syros,
884 the Vari Detachment was reactivated as a semi-brittle to brittle extensional structure and
885 accommodated late stages of exhumation (Fig. 2).

886 Soukis and Stockli (2013) presented low-temperature zircon and apatite (U-Th)/He
887 thermochronology, and concluded that the southern Syros CBU was juxtaposed with two
888 structurally higher upper-plate units, the Upper Unit (intermediate structural level) and
889 Vari Unit (structurally highest), along at least two semi-brittle detachment faults (Fig. 13C,
890 labeled as future structures). While the Tinos Detachment exhumed CBU rocks between
891 ~ 22 -19 on what would become neighboring Tinos Island, low-angle normal faults juxtaposed
892 the Vari and Upper Units on Syros. Exhumation of the Vari and Upper Units at ~ 13 -15 Ma
893 was roughly coeval with magmatism on Tinos but the Syros CBU exhumed later, ~ 8 -10 Ma,
894 beneath the Vari Detachment (Soukis & Stockli, 2013). Final exhumation of the CBU on
895 Syros occurred in multiple, temporally distinct, rapid episodes of unroofing. Exhumation
896 beneath the Vari Detachment was rapid, but only accommodated the final ~ 6 -9 km of
897 vertical exhumation (Ring et al., 2003).

898 **9 Implications**

899 The tectonic model described above has several similarities and differences compared
900 to previous tectonic models. First, our results agree with previous studies suggesting that
901 Syros is composed of distinct tectonic slices that reached peak conditions at different times
902 (Laurent et al., 2017; Lister & Forster, 2016; Ring et al., 2020; Uunk et al., 2018). However,
903 while some previous work has identified two slices in the north and south (Ring et al., 2020;
904 Uunk et al., 2018), our data indicate that there may be a third slice in between. The timing
905 of subduction of Fabrikas rocks provides key constraints on how many tectonic slices exist.
906 Skelton et al. (2019) interpreted their Rb-Sr isochrons as records of peak subduction at ~ 40
907 Ma, which is younger than garnet crystallization ages presented by Kendall (2016). If Fab-
908 rikas did reach peak conditions at ~ 40 Ma, this supports the inference of a central slice above
909 Fabrikas, because our new Rb-Sr isochron from Azolimnos indicates that rocks occupying a
910 higher structural level above Fabrikas experienced blueschist facies retrogression at ~ 45 Ma,
911 and therefore must have reached peak conditions before that. If the garnet crystallization
912 ages presented by Kendall (2016) are accurate records of peak subduction of the southern
913 Fabrikas nappe unit (e.g. weighted mean at ~ 45 Ma), then this also supports the interpre-
914 tation of an intermediate slice, which was exhuming at the same time as Fabrikas nappe
915 reached peak conditions. Future structural and geochronologic investigations should target
916 garnet-bearing lithologies within the proposed central nappe to constrain the timing of peak
917 subduction in this intermediate structural unit. Our study places quantitative constraints
918 bracketing the timing of subduction of each slice, demonstrates that deformation occurred
919 continuously throughout the Eocene and Oligocene, and illustrates that subduction- and
920 exhumation-related fabrics developed contemporaneously at different structural levels.

921 Furthermore, we argue that mafic blueschists and eclogites do not exclusively occupy
922 the structurally highest tectonic slice, in contrast to Laurent et al. (2016) and Trotet, Jo-
923 livet, and Vidal (2001). Rather, protoliths for mafic blueschists and eclogites were present

924 throughout the CBU before subduction and therefore appear to record primary relationships
 925 (cf. Keiter et al., 2011). This implies that the mafic blueschists and eclogites at Vaporia,
 926 Kalamisia and Fabrikas are not separated from surrounding schists and marbles by shear
 927 zones and/or detachments, as shown for the ‘Kampos subunit’ of Laurent et al. (2016).
 928 The primary observations supporting that Fabrikas cannot belong to the same subducting
 929 unit are that Fabrikas meta-volcanics record peak metamorphism that is distinctly younger
 930 than that of Kampos and Kini, Fabrikas crops out towards the southern end (i.e. bottom)
 931 of the north-dipping structural pile, and Fabrikas meta-volcanics are associated with more
 932 meta-carbonate and meta-clastic sedimentary lithologies than Kampos and Kini suggesting
 933 they represent subduction of different protolith assemblages. Moreover, the fact that Fab-
 934 rikas occupies the immediate footwall of the Vari Detachment does not necessarily imply
 935 that it belongs to the structurally highest unit. Even though the Vari Detachment has
 936 been interpreted as the paleo-subduction channel roof, continuous ductile extension along
 937 a shallowly to moderately dipping structure throughout the Eo(?)–Oligocene, in addition
 938 to the proposed 6–9 km of semi-brittle exhumation accommodated by ~ 20 km of localized
 939 slip in the Miocene (Ring et al., 2003), can easily explain tectonic removal of the uppermost
 940 units. This process would juxtapose structurally deeper CBU units with the Upper Unit in
 941 the hanging wall.

942 Our observations indicate that prograde textures are locally preserved in mafic blueschists
 943 and eclogites (cf. Keiter et al., 2004), but the majority of the Syros CBU has been over-
 944 printed during subduction channel exhumation (cf. Bond et al., 2007; Rosenbaum et al.,
 945 2002; Trotet, Vidal, & Jolivet, 2001). Heterogeneous rock types that occupy a given nappe
 946 were subducted and exhumed together, and therefore experienced identical P–T paths (in
 947 contrast to Trotet, Vidal, and Jolivet (2001); Trotet, Jolivet, and Vidal (2001)). There-
 948 fore, differences in strain, metamorphic mineral assemblages, and/or preserved kinematics
 949 between mafic blueschists and eclogites and meta-sedimentary rocks can be attributed to
 950 relative strengths, bulk composition, and fluid availability (and composition) during meta-
 951 morphism (see Schmädicke and Will (2003) for a similar discussion of P–T paths and retro-
 952 gression of the CBU on Sifnos).

953 Exhumation from peak depths was accommodated by well-distributed, ductile coaxial
 954 thinning throughout the bulk stack (cf. Bond et al., 2007; Rosenbaum et al., 2002) and
 955 resulted in penetrative Eocene–Oligocene blueschist and greenschist facies retrogression, un-
 956 related to regional Miocene greenschist facies deformation. Velocity vectors across a dipping
 957 planar shear zone (i.e. non-downward tapering) can yield simultaneous subduction and re-
 958 turn flow depending on the balance between down-dip shear traction (Couette flow), and
 959 up-dip buoyancy (Poiseuille flow) (Beaumont et al., 2009; Raimbourg et al., 2007; Warren
 960 et al., 2008; Xia & Platt, 2017), thus giving rise to the subduction channel. Calculated
 961 flow vectors predict that subduction imparts non-coaxial shear strain (e.g., Fig. 13A) and
 962 immense strain rate gradients across the shear zone, resulting in heterogeneous distributions
 963 of finite strain, as documented in blueschist-eclogite lithologies at Grizzas and Kini. Ex-
 964 humation vectors are characterized by two opposite shear senses that switch across the axis
 965 of maximum exhumation velocity (Gerya et al., 2002; Raimbourg et al., 2007; Xia & Platt,
 966 2017). Therefore, in the center of the upward-translating portion of the channel, exhuma-
 967 tion is slow and kinematics are effectively coaxial, consistent with the rates and distribution
 968 of strain during exhumation of the Syros nappes (Fig. 13B,C).

969 Non-coaxial deformation on the eastern and southeastern side of the island can be
 970 attributed to proximity to the Vari Detachment, which is thought to have operated as
 971 the extensional subduction channel roof (Aravadinou & Xypolias, 2017; Laurent et al.,
 972 2016; Ring et al., 2020). Compiled metamorphic geochronology and new Rb–Sr ages allow
 973 us to calculate exhumation rates of 1.5–5 mm/yr ($= 1.5\text{--}5$ km/Myr) for each underplated
 974 nappe. These rates are roughly an order of magnitude slower than subduction for the
 975 Hellenides, and are consistent with buoyancy-driven, channelized return flow in a distributed
 976 shear zone (Burov et al., 2014; Gerya et al., 2002; Warren et al., 2008). Furthermore,

977 mm/yr exhumation rates are not consistent with fast rates (comparable to subduction rates)
 978 predicted for exhumation along deep-reaching, highly-localized detachments in a downward-
 979 tapering ‘extrusion wedge’ (e.g., Ring & Reischmann, 2002; Ring et al., 2020), nor with
 980 forced return flow and melange-like mixing in a low-viscosity wedge (Cloos, 1982; Gerya
 981 et al., 2002). Thus, between ~ 50 and ~ 25 Ma, return flow in the subduction channel
 982 accomplished *at least* 35 km, and potentially as much as 55 km of vertical exhumation from
 983 maximum depths to the greenschist facies middle crust (~ 4 kbar, ~ 15 km), accounting for
 984 ~ 75 -80% of CBU exhumation.

985 On a regional scale, subduction, underplating, and syn-subduction exhumation were
 986 fundamental processes during construction of the greater Attic-Cycladic Complex (e.g.,
 987 Jolivet et al., 2003; Laurent et al., 2017; Lister & Forster, 2016; Ring & Layer, 2003; Ring et
 988 al., 2020; Trotet, Jolivet, & Vidal, 2001). CBU rocks on Sifnos have garnet crystallization
 989 ages of ~ 47 -45 Ma (Dragovic et al., 2012, 2015), comparable to the base of the Syros stack.
 990 The Basal Unit exposed on Evia and Samos reached peak conditions at ~ 24 -22Ma (Ring et
 991 al., 2001; Ring & Reischmann, 2002; Ring & Layer, 2003), contemporaneous with late stages
 992 of syn-subduction greenschist facies exhumation at the base of the CBU on Syros (Fig. 10).
 993 The structurally deeper Phyllite-Quartzite Nappe and Plattenkalk unit exposed on Crete
 994 experienced HP/LT metamorphism between ~ 24 -20 Ma (Seidel et al., 1982; Thomson et al.,
 995 1999), which also overlaps with latest stages of greenschist facies exhumation on Syros (Fig.
 996 10). Extension and core complex capture that initiated during trench rollback reworked
 997 the ACC to its present configuration, and locally reactivated nappe-bounding thrusts as
 998 extensional structures (e.g., Vari Detachment on Syros).

999 10 Conclusions

1000 Structural analysis, metamorphic petrology, and new and compiled geochronology
 1001 demonstrate that exhumed HP/LT rocks on Syros Island (Cyclades, Greece) record progres-
 1002 sive subduction, underplating, and return flow of three separate tectonic slices. Each nappe
 1003 records a similar structural and metamorphic history, despite subducting at different times.
 1004 Prograde subduction and underplating of each tectonic slice was characterized by asymmet-
 1005 ric top-to-the-SSW and top-to-the-S shear strain, and was reached at ~ 53 -52 Ma (northern
 1006 nappe), ~ 50 Ma? (central nappe) and ~ 47 -45 Ma (southern nappe). Prograde deformation
 1007 and metamorphism is locally preserved in the northern and central nappes, but the majority
 1008 of the island’s meta-sedimentary lithologies were retrogressed during syn-orogenic blueschist-
 1009 to-greenschist facies exhumation. The subduction-to-exhumation transition in each nappe
 1010 is marked by systematic kinematic changes: dominant transport directions rotated from
 1011 roughly N-S (syn-subduction), to NE (post-underplating, at the subduction-to-exhumation
 1012 transition), to E-W (return flow) and the strain geometry switched from asymmetric to coax-
 1013 ial. Progressive subduction of structurally deeper nappes occurred contemporaneously with
 1014 exhumation of structurally higher nappes throughout the Eocene and Oligocene, captur-
 1015 ing syn-subduction exhumation in the Hellenic subduction channel shear zone. Subduction
 1016 channel return flow proceeded at ~ 1.5 -5 mm/yr, which is an order of magnitude slower than
 1017 subduction, and accounted for $\sim 80\%$ of the vertical exhumation of the CBU. Continuous
 1018 subduction, punctuated underplating, and syn-subduction exhumation appear to be fun-
 1019 damental processes during construction of the Attic-Cycladic Complex in the Central and
 1020 Southern Cyclades.

1021 Acknowledgments

1022
 1023 This work was funded by an NSF Graduate Research Fellowship awarded to A.K.,
 1024 an NSF Career Grant (EAR-1555346) awarded to W.B., an NSF Grant (EAR-1725110)
 1025 awarded to W.B., J.B., and D.S., a Jackson School Seed Grant awarded to J.B., W.B., and
 1026 D.S., Jackson School Graduate Research Fellowships awarded to A.K. and M.C., and Ford

1027 Foundation fellowship awarded to M.C. Many thanks to Staci Loewy and Aaron Satkoski
1028 (JSG, UT Austin) for help with Rb-Sr chemistry and isotope analyses, James Maner for
1029 assistance with the microprobe, and Emily Mixon for help with mineral separation. This
1030 project was part of A.K.'s Ph.D. dissertation and benefited from many conversations with
1031 Mark Cloos and Spencer Seman. The authors are grateful to Valentin Laurent and Uwe
1032 Ring for thoughtful and constructive reviews that improved this manuscript. The data that
1033 support the conclusions of this article are presented in the main text and in the supporting
1034 information. Quantitative microprobe analyses are available on the EarthChem repository
1035 (<https://doi.org/10.26022/IEDA/111827>). Structural data and Rb-Sr geochronologic data
1036 are available on the ETH repository (<https://doi.org/10.3929/ethz-b-000463143>). The au-
1037 thors declare no conflicts of interest.

1038 **Appendix A Geochronology**1039 **A1 Rb-Sr Methods and Sample Descriptions**

1040 Cm-sized pieces of rock were cut out from hand samples to isolate specific fabrics
 1041 corresponding to progressive stages of deformation-metamorphism as outlined in Section 5.
 1042 Samples were crushed with a small hammer between sheets of paper, and ground gently
 1043 with a mini metal rock crusher to separate mineral aggregates. Samples were sieved and
 1044 separated by grain size. Grain size fractions 125-250 μm and 250-500 μm were frantzed to
 1045 separate minerals based on magnetic susceptibility. The first pass was done with strongest
 1046 magnetic setting (~ 1.8 Amperes) to remove all non-magnetics (e.g., quartz). Subsequent
 1047 passes were done starting at the lowest setting where minerals started to magnetically sep-
 1048 arate (typically ~ 0.2 - 0.4 A); separates were repeatedly passed through the Frantz at in-
 1049 crements of ~ 0.1 - 0.2 A. Magnetic fractions were then cleaned by hand, by either negative
 1050 or positive picking of phases of interest, including garnet, glaucophane, epidote, and white
 1051 micas (and apatite and chlorite for retrograde fabrics). White mica separates were cleaned
 1052 of inclusions by gently smearing them in a mortar and pestle and washing them through
 1053 a sieve with ethanol. SY1616 was collected from float blocks at Kini Beach immediately
 1054 beneath in-place blueschist-to-eclogite facies cliff faces. The sample is representative of D_S
 1055 in blueschist-eclogite lithologies. The foliation is defined by glaucophane, epidote, phengite,
 1056 paragonite, and rutile, with porphyroblasts of garnet and omphacite. Glaucophane, epidote,
 1057 omphacite, and phengite define the lineation. A similar rock type is shown in Figure 7A.
 1058 The prograde fabric was targeted for geochronology.

1059 KCS1617 was collected from Azolimnos (approximate location: $37^\circ 24'43.86''\text{N}$, 24°
 1060 $57'55.42''\text{E}$). The sample records an older D_S cleavage cross-cut by the D_{T1} upright crenula-
 1061 tion. The mineral assemblage includes glaucophane, epidote, quartz, phengite, paragonite,
 1062 garnet, rutile, titanite, and oxides. The D_{T1} fabric was cut out of the sample using a
 1063 diamond-tipped rock saw and targeted for geochronology.

1064 KCS1621 was collected from the southern side of Delfini Beach (approximate location:
 1065 $37^\circ 27'14.61''\text{N}$, $24^\circ 53'51.23''\text{E}$). The sample is representative of D_{T2} . The foliation is defined
 1066 by quartz, phengite, paragonite and the lineation is defined by porphyroblasts of epidote and
 1067 actinolite. This sample is interbedded with quartz-rich schists that have a blue amphibole
 1068 lineation decimeters to meters above and below. The greenschist-facies fabric was targeted
 1069 for geochronology.

1070 SY1402 was collected from Lotos (approximate location: $37^\circ 26'36.64''\text{N}$, $24^\circ 53'48.87''\text{E}$).
 1071 The sample is representative of D_{T2} , during penetrative greenschist-facies deformation and
 1072 transposition of older fabrics, and some rocks surpass the ductile-to-brittle transition. The
 1073 sample collected for geochronology is a reaction rind at the margin of a brittlely boudinaged
 1074 epidote-rich lens, and includes actinolite, chlorite, epidote, phengite, paragonite, and ap-
 1075 atite. SY1644 was collected from the southern side of Delfini, very close to KCS1621. The
 1076 sample is representative of D_{T2} , as rocks locally surpass the ductile-to-brittle transition.
 1077 Minerals collected for geochronology were precipitated within the boudin neck of a brittlely
 1078 boudinaged epidote-rich lens including actinolite, epidote, white mica, and calcite.

1079 **A2 Compilation and treatment of previous geochronology on Syros**

1080 Figure A1 and Table A2 show a compilation of published metamorphic geochronology
 1081 for the island of Syros (through 2019), comprising 185 individual published ages from 16
 1082 studies and 5 chronometers. Applying filters discussed in Section 6.2 to the dataset shown
 1083 in Figure 3B reduces the compilation from 89 (excludes igneous zircon) to 44 data points,
 1084 which are plotted in Figure 10. The refined dataset comprises 65 individual ages (some
 1085 presented as weighted means) that include 44 single-grain analyses and 21 isochrons. The
 1086 single-grain analyses include 6 $^{40}\text{Ar}/^{39}\text{Ar}$ white mica (Rogowitz et al., 2014; Laurent et
 1087 al., 2017), 37 $^{87}\text{Rb}/^{86}\text{Sr}$ white mica (Cliff et al., 2016), and 1 U-Pb SHRIMP zircon age

Sample ID and Summary	Phases defining the isochron	Initial Sr	Age	Uncertainty	MSWD	n	
SY1616: Kini omphacite-epidote blueschist	paragonite-phengite	0.7032083	53.53	0.17	1	2	
	glaucophane-phengite	0.7032228	53.29	0.17	1	2	
	omphacite-phengite	0.7032158	53.41	0.17	1	2	
	garnet-phengite	0.703212	53.47	0.21	1	2	
	epidote-garnet-phengite	0.7032199	53.34	0.15	0.91	3	
	epidote-omphacite-phengite	0.7032198	53.34	0.14	0.64	3	
	epidote-garnet-omphacite-phengite	0.7032183	53.36	0.14	0.56	4	
	glaucophane-omphacite-garnet-phengite	0.7032179	54.37	0.14	0.46	4	
	omphacite-paragonite-garnet-phengite	0.7032121	53.47	0.14	0.28	4	
	paragonite(x4)-phengite	0.7031964	53.73	0.13	1.4	5	
	** cp-glauc-omph-parag-grt ** NO PHENG	0.703221	59.07	8.57	1.7	5	
	KCS1617: Azolimnos glaucophane-mica blueschist	epidote-phengite	0.7066671	45.14	0.05	1	2
		glaucophane-phengite	0.7065696	45.61	0.1	1	2
		paragonite-phengite	0.7065964	45.48	0.05	1	2
paragonite-phengite-phengite		0.7065992	45.47	0.05	0.41	3	
glaucophane-phengite-phengite		0.7065829	45.56	0.61	8.8	3	
epidote-phengite-phengite		0.706643	45.23	0.05	0.31	3	
** glaucophane-paragonite(x4) ** NO PHENG		0.7066026	43.44	0.76	10	5	
paragonite(x4)-phengite		0.7065951	45.48	0.13	9.4	5	
8 point isochron (all data, except garnet)		0.7066036	45.43	0.04	23	8	
KCS1621: Delfini actinolite-mica greenschist		** paragonite-chlorite ** NO PHENG	0.7066492	35.64	0.39	1	2
		paragonite-chlorite-phengite	0.7066201	37.04	0.015	13	3
		** epidote-chlorite-paragonite ** NO PHENG	0.7066492	35.64	0.39	7.90E-25	3
		epidote-phengite-phengite	0.7067163	36.9	0.03	6.30E-24	3
		epidote-chlorite-phengite(x2)	0.7066195	37.06	0.02	21	4
	epidote-paragonite-phengite(x2)	0.7066498	37.02	0.02	9.8	4	
	** epidote-chlorite-paragonite(x3) ** NO PHENG	0.7066471	36.19	0.29	7.9	5	
	paragonite(x3)-phengite(x2)	0.7066348	37.05	0.014	16	5	
	chlorite-paragonite(x3)-phengite(x2)	0.7066266	37.06	0.013	16	6	
	epidote-chlorite-paragonite(x3)-phengite(x2)	0.7066266	37.06	0.013	13	7	
	8 point isochron (all data)	0.7065941	36.91	0.013	440	8	
	SY1644: Delfini mineralization in epidiosite boudin neck	epidote-white mica	0.7066098	36.16	0.03	1	2
		actinolite-white mica	0.7067006	35.94	0.03	1	2
	SY1402: Lotus reaction rim around epidiosite pod	apatite-phengite1	0.704965	36.49	0.01	1	2
apatite-phengite2		0.704965	35.94	0.01	1	2	
apatite-phengite3		0.704965	33.18	0.011	1	2	
apatite-phengite4		0.704966	29.43	0.014	1	2	

Table A1: Evaluating the robustness of Rb-Sr ages. Various isochrons are calculated for each sample discussed in-text, for different combinations of (assumed) co-genetic phases. MSWD values are a reflection of analytical uncertainty and the goodness of fit of all data points on a given isochron; therefore, any two-point isochron by definition has an MSWD of 1.

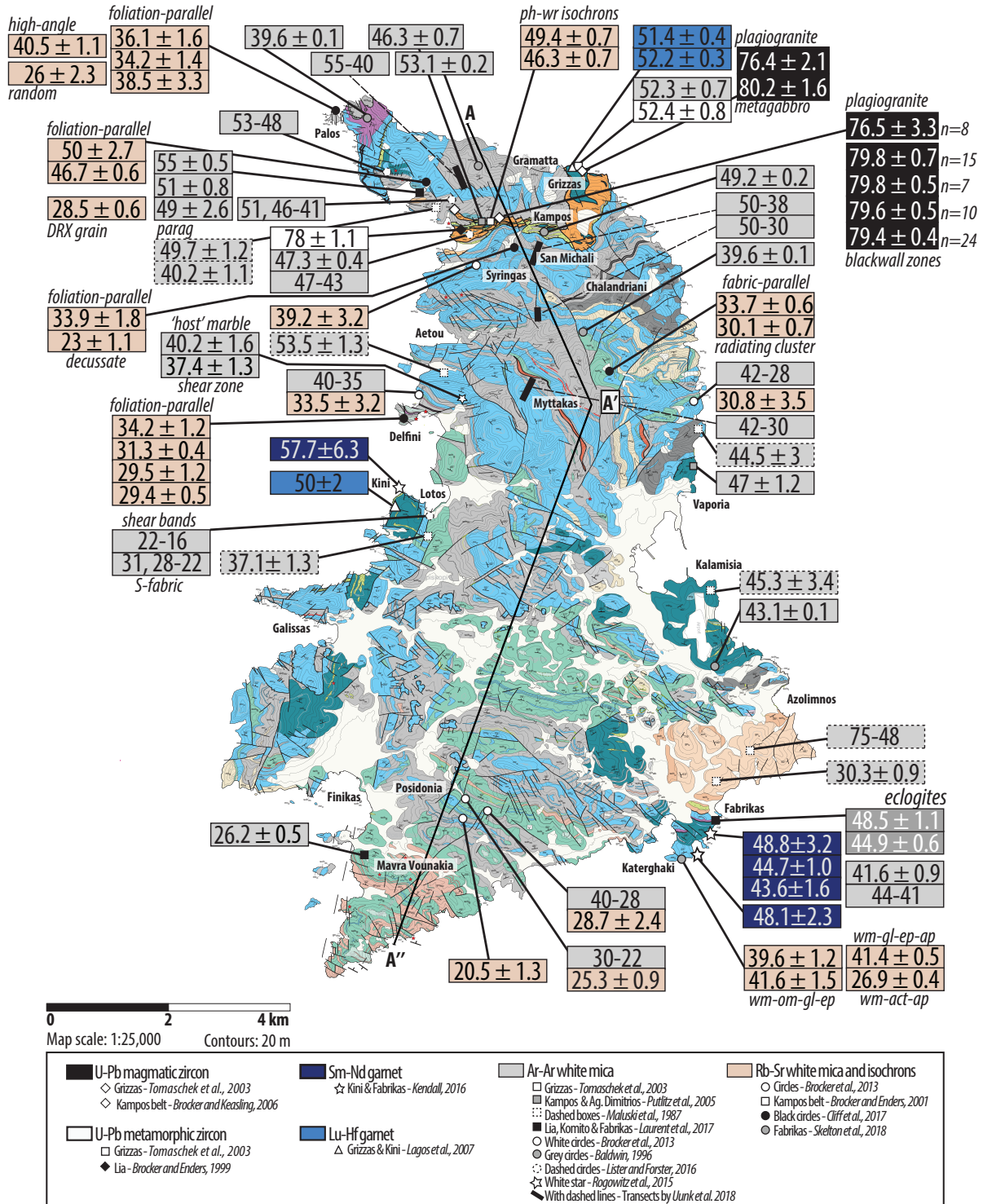


Figure A1: Compilation of the locations and ages from published metamorphic geochronology (and magmatic ages from Kampos), from references listed in grey box and discussed in Section 2. Samples are projected onto the cross-section line A-A'-A'' as shown in Figure 10. Sample locations are coded by color and shape according to citation, and box colors around reported ages correspond to different chronometers. Abbreviations for boxes with notes indicating the sample's micro-structural and/or lithologic context are as follows: DRX = dynamically recrystallized; wm=white mica, ph=phengite, om=omphacite, gl=glaucophane, ep=epidote, act=actinolie, ap=apatite, wr=whole rock.

#	Method	Closure Temp	Sample Name and Description	GPS Coordinates ^a	Location	Age	Uncertainty	Notes	Interpretation*	Ref.
1	U-Pb zircon	>750°C	metagabbro		Grizzas	80.2	1.6		magmatic crystallization (protolith)	[1]
2			meta-plagiogranite dyke		Grizzas	76.4	2.1		magmatic crystallization (protolith)	[1]
3			meta-plagiogranite breccia		Grizzas	52.4	0.8	skeletal rims, low Th/U	HP metamorphism	[1]
4			1081 omphacite		Kampos belt	78	1		interpreted as HP met, but likely magmatic	[2]
5			4017 plagiogranite in meta-gabbro	37°29.704'N, 024°54.005'E	Kampos belt	77	1	oscillatory zoned zircons	interpreted as HP met, but likely magmatic	[3]
6						76.1	1.2			[3]
7						76.6	1.3			[3]
8						76.6	1.1			[3]
9						76.9	1.1			[3]
10						75	1.2			[3]
11						76.1	1.3			[3]
12						78	1.1			[3]
						average	76.5	3.3		
13			3148 Jadeite: albite + jadeite; accessories	37°29.362'N, 024°54.335'E	Kampos belt blackwall zone	80.3	0.9	oscillatory zoned zircons (likely		[3]
14			titanite, allanite, zircon, white mica, chlorite,			78.7	0.9	magmatic, or seafloor		[3]
15			apatite			80.0	0.9	metasomatism)		[3]
16						78.6	0.7			[3]
17						78.2	0.8			[3]
18						80.6	0.8			[3]
19						78.6	0.7			[3]
20						79.4	0.9			[3]
21						80.7	0.7			[3]
22						79.9	0.7			[3]
23						80.6	0.7			[3]
24						79.8	0.6			[3]
25						77.3	1.4			[3]
26						80.8	0.7			[3]
27						82.9	2.2			[3]
						average	79.8	3.8		
						reported weighted mean	79.8	0.7		
28			3149 Omphacite: omph, alb, wm, tm, chl,	37°29.362'N, 024°54.335'E	Kampos belt blackwall zone	79.7	0.5	oscillatory zoned zircons (likely		[3]
29			opaques			79.9	0.3	magmatic, or seafloor		[3]
30						78.5	0.8	metasomatism)		[3]
31						78.4	0.4			[3]
32						76.7	0.5			[3]
33						79.9	1.0			[3]
34						77.6	1.0			[3]
						average	78.7	1.8		
						reported weighted mean	79.8	0.5		
35			3151 Glaucophane: glaucophane; subordinate	37°29.362'N, 024°54.335'E	Kampos belt blackwall zone	78.9	0.8	oscillatory zoned zircons (likely		[3]
36			amounts of omph, rt, tm, zrc, all, wm, bt			79.9	0.8	magmatic, or seafloor		[3]
37						78.9	1.2	metasomatism)		[3]
38						79.1	1.2			[3]
39						82.2	1.3			[3]
40						80.0	0.8			[3]
41						78.4	0.7			[3]
42						79.2	0.7			[3]
43						80.3	0.9			[3]
44						80.6	1.0			[3]
						average	79.8	3.0		
						reported weighted mean	79.6	0.5		
45			3152-A Chlorite Actinolite Zone: chl, act, rt,	37°29.362'N, 024°54.335'E	Kampos belt blackwall zone	77.5	1.8	oscillatory zoned zircons (likely		[3]
46			zrc, wm, ap			80.4	1.3	magmatic, or seafloor		[3]
47						82.3	2.0	metasomatism)		[3]
48						78.5	1.1			[3]
49						80.4	2.1			[3]
50						77.7	1.4			[3]
51						78.2	1.3			[3]
52						79.7	0.7			[3]
53						81.3	1.1			[3]
54						80.0	1.8			[3]
55						78.9	1.1			[3]
56						84.0	3.7			[3]
57						79.9	1.0			[3]
58						81.1	0.8			[3]
						average	80.0	6.2		
59			3152-B Chlorite-Actinolite Zone:	37°29.362'N, 024°54.335'E	Kampos belt blackwall zone	76.2	1.3	oscillatory zoned zircons (likely		[3]
60						81.3	1.0	magmatic, or seafloor		[3]
61						79.5	1.0	metasomatism)		[3]
62						78.4	1.1			[3]
63						76.9	1.3			[3]
64						73.1	0.7			[3]
65						79.6	0.5			[3]
66						79.3	1.3			[3]
67						78.5	0.8			[3]
68						79.1	0.7			[3]
						average	78.2	3.2		
						reported weighted mean	79.4	0.4		
69	Sm/Nd garnet	600-700°C	06MSY-6E rutile-bearing eclogite		Kini	57.7	6.3	8 grt-leachate-wr isochron	garnet growth	[4]
70			14RSY-8A mica-rich eclogite		Fabrikas	48.8	3.2	4 grt-wr isochron	garnet growth	[4]
71			14BSY-35D mica-rich eclogite, float		Fabrikas	48.1	2.3	bulk grt-grt-wr isochron	garnet growth	[4]
72			14BSY-35D mica-rich eclogite, float		Fabrikas	47.1	3	rims of garnet, microdrilled; rim-rim-rim pvt-matrix isochron	garnet growth	[4]
73			14BSY-38A, eclogite boudin in quartz schist matrix		Fabrikas	44.7	1.5	grt-wr isochron	garnet growth	[4]
74			14BSY-37A eclogite, float		Fabrikas	43.6	1.6	5 grt-wr isochron	garnet growth	[4]
75	Lu/Hf garnet	600°C	Ag31: meta-igneous breccia		Grizzas	52.2	0.3	wr-zrn-tm-leftover-4grt isochron; table top digestion	early garnet crystallization (Lu fractionation)	[5]

Table A2: Compilation of published metamorphic geochronology for Syros Island. Data are plotted against closure temperature in Figure 3B. References: (1) Tomaschek et al. (2003), (2) Bröcker and Enders (1999), (3) Bröcker and Keasling (2006), (4) Kendall (2016), (5) Lagos et al. (2007)...

76	Ag85: meta-igneous breccia		Grizzas	51.4	0.4 w-omph-'leftover'-lgrt isochron; table top digestion	early garnet crystallization (Lu fractionation)	[5]
77	Ap21: glaucophane eclogite		Kini	50	2 w-omph-'leftover'-3grt isochron; table top digestion	early garnet crystallization (Lu fractionation)	[5]
78	Rb-Sr WM	-500°C +/- 50					
79	5243 Ph-Chl-Ab-Qz-Ep-Cal-Tm-Gr schist	N 37° 23.50' E 24° 54.633'	South Central, Posidonia	28.7	2.4 ph-cal isochron	ages record continuous (partial) resetting of isotopic	[6]
80	5244 Ph-Chl-Ab-Qz-Ep-Cal-Tm schist	N 37° 23.265' E 24° 54.365'	South Central, Posidonia	20.5	1.3 ph-ep-ab isochron	systematics and/or (re)crystallization of white mica	[6]
81	5246 Ph-Pg-Chl-Ab-Qz-Ep-Cal-Tm schist	N 37° 23.643' E 24° 54.151'	South Central, Posidonia	25.3	0.9 ph-ep-cal isochron	during exhumation and greenschist facies	[6]
82	5267 Ph-Chl-Ab-Qz-Cal-Tm schist	N 37° 27.734' E 24° 53.898'	N. Delfini	33.5	3.2 ph-cal isochron	retrogression	[6]
83	SYR015 Ph-Pg-Chl-Ab-Qz-Ep-Cal-Tm schist	N 37° 27.497' E 24° 56.767'	N. of Agios Dimitrios	30.8	2.9 ph-par-ep isochron		[6]
	5831 Ph-Chl-Ab-Qz-Ep-Cal-Tm-Aet schist	N 37° 28.808' E 24° 54.723'	Syringas (S. of Kampos)	39.2	3.2 ph-ep-ab-cal isochron		[6]
84	1081 Omphacite		Kampos belt	49.4	0.7 ph-wr isochron	interpretation not provided in text; likely crystallization	[7]
85	1083 Omphacite		Kampos belt	46.3	0.7 ph-wr isochron	and/or incipient recrystallization	[7]
86	63286 - calc-schist, cal-ph-glc-qz-ab		Palos, Diapori	35.2	1.4 fabric-parallel phengites, 1 randomly oriented aggregate, 2 calcite	Purposefully targeted extensional blueschist- and greenschist-facies fabrics. Phengites were microdrilled from specific microstructures in calc schists and metabasites. Interpreted as "continuous deformation on a regional scale" and exhumation-related (re-)crystallization.	[8]
87				37.4	0.8 single phengite		[8]
88				34.4	0.8 single phengite		[8]
89				37.5	1.7 single phengite		[8]
90				36.1	1.6 mean of above 4 grains		[8]
				26	2.3 randomly oriented phengite		[8]
91	63297 - calc-schist, cal-ph-glc-ep-qz-ab		Palos, Diapori	35.6	0.5 4 fabric-parallel phengites, 1 grain at high angle to fabric, 3 calcite		[8]
92				32.2	0.3 single phengite		[8]
93				34.6	1.1 single phengite		[8]
94				34.4	0.5 single phengite		[8]
95				34.2	1.4 mean of above 4 grains		[8]
				40.5	1.1 high angle phengite, wrapped by foliation-parallel phengites		[8]
96	63300 - calc-schist, cal-ph-glc-chl-qz-ab		Palos, Diapori	41.8	2.4 fabric-parallel phengites, 1 calcite		[8]
97				37.1	0.4 single phengite		[8]
98				40.5	0.4 single phengite		[8]
99				34.4	0.5 single phengite		[8]
				38.5	3.3 mean of above 4 grains		[8]
100	63287a - calc-schist, cal-ph-grt-dol-glc-qtz-ep-mm		Grammata	52.5	0.8 6 fabric-parallel phengites, 4 calcite		[8]
101				52.1	1.1 single phengite		[8]
102				46.9	2.3 single phengite		[8]
103				48.6	0.5 single phengite		[8]
				50	2.7 mean of above 4 grains		[8]
104	63287b			47.1	0.6 single phengite		[8]
105				46.2	1.3 single phengite		[8]
				46.7	0.6 mean of above 2 grains		[8]
106	63287a			28.5	0.6 single phengite, has fine grained recrystallized phengite next to it		[8]
	S97/234 - greenschist, ab-chl-ph-ep-qz-cal, rare glc		N. Oros Syringas		4 fabric-parallel phengites + 3 ep; 1 grain from decussate pressure shadow adjacent to garnet		[8]
107				33.6	0.4 pseudomorph		[8]
108				29.4	2.3 single phengite		[8]
109				34	0.5 single phengite		[8]
				33.9	1.8 weighted mean of above 3 grains		[8]
110				23	1.1 decussate phengite		[8]
111	63301 - greenschist, qz-ph-chl-ab-cal-dol-tm-ap-pg		Foinikia	30.1	0.7 decussate/radiating cluster at high angle to fabric; plus 2 cal + 2 tm		[8]
112				33.7	0.6 composite fabric-parallel sample		[8]
113	63310 - blueschist, ep-glc-ph-cal-qz-ab-tm-tour-chl		Delfini		2 phengite composite samples		[8]
114				31.3	0.4 aligned with schistosity; 3 cp + 2 cal		[8]
				29.5	1.2 composite #2		[8]
115	63314 - blueschist, ph-glc-qz-ep-tm-chl-ab-cal-ap		Delfini	34	1.7 8 fabric-parallel phengites, 1 epidote, 1 apatite, 2 tm, lots of ep inclusions		[8]
116				39.5	3.1 single phengite		[8]
117				33.9	1.2 single phengite		[8]
118				36.3	1.3 single phengite		[8]
119				34.3	1.2 single phengite		[8]
120				33.7	0.6 single phengite		[8]
				34.2	1.3 regression of above six grains w. epidote		[8]
121				29.7	0.7 single phengite		[8]
122				29.2	0.7 single phengite		[8]
				29.4	0.5 weighted mean of youngest grains		[8]
123	15-SY-03 glaucophane eclogite	GPS points approximated from map, not provided in text		39.6	1.2 4wm-omph-glauc-ep isochron	Interpreted as peak metamorphism, but probably	[9]
124	15-SY-05 glaucophane eclogite	37°23'20.99"N 24°57'13.35"E Fabrikas	Fabrikas	41.6	1.5 4wm-omph-glauc-ep-ap isochron	'reworked' during exhumation	[9]
125	15-SY-01-02 epidote blueschist	37°23'17.66"N 24°57'9.50"E	Fabrikas	41.36	0.45 4wm-glauc-ep-ap isochron	greenschist recrystallization	[9]
126	17 FB 05 greenschist		Fabrikas	26.9	0.4 wm-act-ap isochron		[9]
127	Ar/Ar WM	-400-450°C				Ar steps yield apparent ages between	
128	AG144 and BSV260 meta-plagiogranite dyke & breccia	550°C (Ref. 11)	Grizzas	52.3	0.7 30-54 Ma	prograde crystallization?	[11]
129	SY01 metachert		North of Delfini	53.5	1.3	prograde?	[10]
130	SY15 metatuff		North of Ag. Dimitrios	44.5	3	(partial) resetting and/or recrystallization	[10]
131	SY30F eclogitic metagabbro		W. Kampos belt	40.2	1.1	(partial) resetting and/or recrystallization	[10]
132	SY501 omphacitic metagabbro		North of Fabrikas	30.3	0.9	(partial) resetting and/or recrystallization	[10]
133	SY7 calc-schist-metatuff		East of Kini	37.1	1.3	(partial) resetting and/or recrystallization	[10]
134	SY66 omphacitic metagabbro		Aiport	45.3	3.4	(partial) resetting and/or recrystallization	[10]
135	SY08 calc-schist		W. Kampos belt	49.7	1.2	paragonite	[10]
136	SY20 metagranite		Vari	48 to 75		no Eocene HP history in Vari Unit	[10]
						Metamorphic crystallization	[10]
137	S07-14 Grt-Omph blueschist	37.4992/24.8935	Grammata	50.84	0.84 single grain (2)	peak conditions	[11]

Table A2: Continued. References: (6) Bröcker et al. (2013), (7) Bröcker and Enders (2001), (8) Cliff et al. (2016), (9) Skelton et al. (2019), (10) Maluski et al. (1987), (11) Laurent et al. (2017)...

138				49.44	2.62	peak conditions	[11]
139	S07-16 Grt-Chl micaschist	37.4992/24.8955	Grammata	55.04	0.56 concentrate	peak conditions	[11]
140	S07-01 Gln-Ep micaschist	37.3891/24.9534	Fabrikas	41.65	0.95 single grain	recrystallization	[11]
141	S07-02 Blueschist	37.3891/24.9534	Fabrikas	43.51	0.56 single grain (2)	recrystallization	[11]
142				41.95	0.77	recrystallization	[11]
143	S07-04 Gln eclogite	37.3891/24.9534	Fabrikas	44.89	0.65 single grain	recrystallization	[11]
144	S07-04bis Gln eclogite	37.3891/24.9534	Fabrikas	40.29	0.73 single grain	recrystallization	[11]
	S07-jojo Gln eclogite	37.3891/24.9534	Fabrikas	48.5	1.1 in situ (10), inverse isochron from eclogite foliation and blueschist shear band combined (ages not resolvable different)	recrystallization	[11]
145							[11]
146	S07-17 Alb-Chl micaschist	37.3791/24.8819	NW of Komito Beach	26.12	0.52 single grain	recrystallization	[11]
147	5267 Pb-Chl-Ab-Qz-Cal-Ttn schist	N 37° 27.734' E 24° 53.898'	N. Delfini	35-40	10 grains	Ar ages span 41-27; Rb-Sr ages span 34-20	[6]
148	SYR015 Pb-Pg-Chl-Ab-Qz-Ep-Cal-Ttn schist	N 37° 27.497' E 24° 56.767'	N. of Agios Dimitrios	28-42	12 grains, excludes 1 outlier	Ages record continuous (partial) resetting of isotopic systematics and/or (re)crystallization of white mica during exhumation and greenschist facies	[6]
149	5243 Pb-Chl-Ab-Qz-Ep-Cal-Ttn-Gr schist	N 37° 23.501' E 24° 54.633'	South Central, Posidonia	28-40	12 grains		[6]
150	5246 Pb-Pg-Chl-Ab-Qz-Ep-Cal-Ttn schist	N 37° 23.643' E 24° 54.151'	South Central, Posidonia	22-30	13 grains		[6]
151	89646 quartzite		Palos	39.6	0.1 total fusion age, gradient in apparent ages 31 to 41.2	partial loss profile and/or recrystallization after HP event	[12]
152	89644 glaucophane-marble schist		Kampos belt	53.1	0.2 phengite, total fusion age, gradient 52.4 to 55	HP event	[12]
153	89642 retrograde eclogite		Kampos belt	49.2	0.2 phengite, flat spectra, weighted mean	HP event	[12]
154	89645 retrograde blueschist		Central	39.6	0.1 total fusion age, gradient 34.8 to 42.4	partial loss profile and/or recrystallization after HP event	[12]
155	89649 retrograde blueschist		Airport	43.05	0.12 total fusion age, gradient 40 to 44.2	partial loss profile and/or recrystallization after HP event	[12]
156	SY-7 phengite-rich eclogite		Kampos belt	46.3	0.7 in-situ UV-laser ablation; weighted mean laser fusion ages (n=27)	paper says prograde; could be partially reset, some ages are older (50-52)	[13]
157	SY-25 omphacite-rich meta-gabbro		Agios Dimitrios	47	1.2 in-situ UV-laser ablation; weighted mean laser fusion ages (n=30)	paper says prograde; our observations of Ag. Dim indicate this is likely recrystallization and/or recrystallization	[13]
158	AG10-31 garnet mica schist	37° 30.081'N 24° 53.173'E	N. of Gramatta	53-48	Δ1B + early Δ1C decussate + post-Δ1C shear zone, pheng-muscovite	All ages from [14] are interpreted as crystallization ages related to different microstructures using the 'method of asymptotes and limits' timing of Δ1B event	[14]
159	AG10-14 garnet mica schist	37° 29.613'N 24° 54.295'E	N. Kampos belt	51, 46-41	Δ1B + Δ1C + post-Δ1C, older phengite component, younger muscovite component	muscovite component records Δ1C growth and post-Δ1C shearing	[14]
160	AG10-15 Δ1C white mica in boudin neck	37° 29.537'N 24° 54.416'E	Kampos belt	43-47	late Δ1C porphyroblastic white mica, from dilational zone next to mega-boudin		[14]
161	AG10-16 early Δ1C decussate wm + titanite	37° 29.546'N 24° 54.404'E	Kampos belt	47.3	0.4 early Δ1C decussate white mica, from edge of mega-boudin		[14]
162	AG10-26S wm-qz-ab-chl-calc greenschist	37° 26.582'N 24° 54.166'E	E. of Kini, roads above Lotos	31, 28-22	Dominant fabric in greenschist facies schist (post-Δ1D and A2)	older phengite component; younger muscovite component	[14]
163	AG10-26C wm-qz-ab-chl-calc greenschist	37° 26.582'N 24° 54.166'E	E. of Kini, roads above Lotos	16-22	Extensional shear bands cutting greenschist fabric (relict post-Δ1D + Δ2 + post-Δ2)	muscovite component	[14]
	Kampos transect - graphite-rich Lws-Grt blueschists and micaschists, with intercalated calcite and siliceous layers		N. of Kampos belt			<i>single grain fusion experiments</i>	
164	12SR100: graphite-rich Lws-Grt-Gln micaschist, static gschit	N37° 29.855', E24° 54.369'		55-48		broad uniform age	[15]
165	12SR57: siliceous marble; Phg+Gln+ Ep+Qz+ Ttn+Chl	N37° 29.856', E24° 54.220'		55-48		broad uniform age	[15]
166	12SR02: graphite-rich Lws(ps)-Grt-Gln micaschist; ttn in foliation	N37° 29.942', E24° 54.566'		52-45		wide uniform age	[15]
167	12SR97: Phg+Qz+Ep+Ttn bearing marble	N37° 29.827', E24° 54.628'		52-45		wide uniform age	[15]
168	12SR03: phg-bearing marble with columnar aragonite pseudomorphs	N37° 29.821', E24° 54.744'		55-40		heterogeneous	[15]
	San Michalis transect - marble-schist-marble sequence; middle unit contains pyrite-bearing schists and gneisses, graphite-rich Lws-Grt-Gln micaschists and quartzitic rocks, locally with static greenschist overprint		S. of Kampos belt			<i>single grain fusion experiments</i>	
169	12SR96: Lws-Grt-Gln micaschist, static gschit	N37° 29.393', E24° 54.891'		49-45		narrow range	[15]
170	12SR04: Lws-Grt-Gln micaschist, static gschit	N37° 29.359', E24° 55.125'		48-40		heterogeneous	[15]
171	12SR13b: carbonated and brecciated blueschist; Cd-Gln, Ep	N37° 29.328', E24° 55.223'		48-40		heterogeneous	[15]
172	12SR92: Phg-bearing marble; aragonite pseudomorphs	N37° 29.395', E24° 54.975'		48-40		heterogeneous	[15]
173	12SR93: Phg-bearing marble; aragonite pseudomorphs	N37° 29.343', E24° 54.904'		50-38		heterogeneous	[15]
	Syringas transect 1 and 2 - intercalated schist-marble sequence; vary from felsic to Ep-blueschists to pervasively overprinted greenschists		Sy1 west coast; Sy2 central			<i>single grain fusion experiments</i>	
174	12SR78: recrystallized felsic mica schist	N37° 28.830', E24° 53.901'		48-42		narrow uniform age	[15]
175	12SR82: calcoschist; Phg+Qz+Chl	N37° 28.666', E24° 55.119'		38-31		intermediate	[15]
176	12SR81: Phg-bearing marble; aragonite pseudomorphs	N37° 28.664', E24° 55.118'		50-40		heterogeneous	[15]
	Mytikas transect - upper and lower marbles bookending felsic schists and gneisses and intermediate-mafic rocks ranging from ep-grt blueschists to pervasively overprinted greenschists		NE of Delfini, central			<i>single grain fusion experiments</i>	
177	12SR19: Phg-bearing marble	N37° 27.889', E24° 55.225'		40-39		narrow uniform age	[15]
178	12SR16: Ep-Ab blueschist (+Grt), partial greenschist overprint	N37° 27.796', E24° 55.147'		40-39		narrow uniform age	[15]
179	12SR20: felsic Ab gneiss; Phg+Qz foliation, Ab porphyroblasts	N37° 27.871', E24° 55.199'		42-30		heterogeneous	[15]

Table A2: Continued. References: (12) Baldwin (1996), (13) Putlitz et al. (2005), (14) Lister and Forster (2016), (15) Uunk et al. (2018) ...

180	12SR18b: intermediate-to-mafic Grt-Ep blueschist; Phg+Gln+Ep matrix	N37°27.841', E24°55.174'		42-30	heterogeneous	[15]
181	12SR18a: blueschist, static greenschist; Phg+Qz matrix	N37°27.811', E24°55.171'		42-30	heterogeneous	[15]
182	12SR17: greenschist mylonite, fine-grained Act+ClI matrix, AB blasts	N37°27.798', E24°55.154'		42-30	heterogeneous	[15]
183	12SR15: siliceous marble, Ep+Phg+Qz, aragonite pseudomorphs	N37°27.808', E24°55.101'		42-30	heterogeneous	[15]
184	Calcite marble, host rock	?	N. of Delfini	40.2	1.6 Si apfu 3.4-3.6, EW stretching	Authors hypothesized these would be Miocene due to strong EW stretching. Interpreted Eocene ages as evidence that the phengite was not reset during Miocene deformation; our results suggest these could be DT2 greenschist deformation [16]
185	Calcite marble, shear zone			37.4	1.3	

Table A2: Continued. References: (16) Rogowitz et al. (2014)

1088 which is a weighted mean of 7 analyses (Tomaschek et al., 2003). The isochrons include
 1089 5 Sm-Nd garnet-whole rock (Kendall, 2016), 3 Lu-Hf garnet-omphacite-whole rock (Lagos
 1090 et al., 2007), 10 multi-mineral and 2 phengite-whole rock $^{87}\text{Rb}/^{86}\text{Sr}$ (Bröcker & Enders,
 1091 2001; Bröcker et al., 2013; Skelton et al., 2019). . The $^{40}\text{Ar}/^{39}\text{Ar}$ ages included in the final
 1092 compilation are strong plateaus from step-heating experiments of grains extracted from
 1093 well-characterized microstructural domains (Laurent et al., 2017). We excluded: 1 Sm-Nd
 1094 isochron with low $^{147}\text{Sm}/^{144}\text{Nd}$ ratio and potential for contamination due to the presence
 1095 of an off-isochron inclusion (cf. Kendall, 2016); 50 $^{40}\text{Ar}/^{39}\text{Ar}$ ages, and one 10-pt inverse
 1096 $^{40}\text{Ar}/^{39}\text{Ar}$ isochron that exhibit one or more of the complications described in Section 6.2
 1097 (Maluski et al., 1987; Baldwin, 1996; Tomaschek et al., 2003; Putlitz et al., 2005; Bröcker
 1098 et al., 2013; Lister & Forster, 2016; Laurent et al., 2017; Uunk et al., 2018). We removed
 1099 the 10-pt isochron from the final compilation because its 10 points combine measurements
 1100 from an eclogitic foliation and a blueschist cross-cutting shear band which overlap within
 1101 error, so this age cannot be conclusively interpreted as either peak eclogite facies nor early
 1102 retrograde blueschist facies. It is likely a mixing line between these two ‘events.’

1103 Lagos et al. (2007) presented Lu-Hf garnet growth ages from meta-igneous rocks at
 1104 Grizzas and Kini, showing that those blueschist-eclogite localities reached peak metamorphic
 1105 conditions at 51.9 ± 1.4 Ma and 50 ± 2 Ma, respectively. New fabric ages from Kini blueschists
 1106 (this study, 52.62 ± 0.64 Ma) overlap with garnet growth ages at Grizzas and Kini, and with
 1107 the SHRIMP age determined by Tomaschek et al. (2003) for Grizzas metamorphic zircons.

1108 Fabrikas eclogites record Sm-Nd garnet crystallization ages of $\sim 45 \pm 3$ Ma (Kendall,
 1109 2016). ‘Bulk’ garnet ages (48.1 ± 2.3 Ma) overlap within error with ‘rim’ ages (47.1 ± 3 Ma),
 1110 providing evidence for rapid, pulsed garnet crystallization that is distinctly younger than
 1111 Grizzas and Kini. A weighted mean of Fabrikas garnet ages using Isoplot (Ludwig et al.,
 1112 2010), weighted by assigned uncertainties, is 45.1 ± 2.9 Ma (two sigma). Garnet growth ages
 1113 are consistent with $^{40}\text{Ar}/^{39}\text{Ar}$ ages of foliation-forming white mica in Fabrikas glaucophane-
 1114 bearing eclogites (48.5 ± 1.1 Ma to 44.9 ± 0.6 Ma, Laurent et al. (2017)).

1115 Retrograde blueschist-facies fabric ages range from ~ 50 -40 Ma, and are captured by:
 1116 (1) Phengite-whole rock Rb-Sr isochrons from omphacites at Kampos (49.4 ± 0.7 Ma and
 1117 46.3 ± 0.7 Ma, Bröcker and Enders (2001)) and Rb-Sr ages of micro-drilled phengites from
 1118 glaucophane-bearing calcschists at Gramatta (50.5 ± 3.1 Ma and 47.3 ± 1.2 Ma, Cliff et al.
 1119 (2016)); (2) A new multi-mineral Rb-Sr isochron from Azolimnos (44.71 ± 0.43 Ma, this
 1120 study); (3) A Rb-Sr isochron from omphacite-blueschists (41.5 ± 1.5 Ma, Skelton et al. (2019))
 1121 and $^{40}\text{Ar}/^{39}\text{Ar}$ ages of foliation-forming white mica in retrogressed Fabrikas eclogites and
 1122 bluechists (44.9 ± 0.65 Ma to 40.3 ± 0.7 Ma, $n=4$, Laurent et al. (2017)).

1123 Retrograde greenschist-facies fabric ages range from ~ 42 -36 Ma, and are captured by
 1124 Rb-Sr multi-mineral isochrons and Rb-Sr ages of foliation-forming micro-drilled phengites
 1125 from greenschists and calcschists from the following locations: (1) Palos (40.5 ± 1.1 Ma to
 1126 34.2 ± 1.4 Ma, Cliff et al. (2016)); (2) Syringas (39.2 ± 3.2 Ma, Bröcker et al. (2013); 33.9 ± 1.8
 1127 Ma Cliff et al. (2016)); (3) North of Delfini (33.7 ± 0.6 Ma, Cliff et al. (2016); 33.5 ± 3.2 Ma
 1128 and 30.8 ± 2.9 Ma, Bröcker et al. (2013)); (4) Delfini (34.2 ± 1.3 Ma to 29.4 ± 0.5 Ma; Cliff et
 1129 al. (2016); 36.47 ± 0.11 Ma, this study); (5) Fabrikas (26.9 ± 0.4 Ma, Skelton et al. (2019));
 1130 and (6) Posidonia (28.7 ± 2.4 Ma, 25.4 ± 0.9 Ma, 20.5 ± 1.3 Ma, Bröcker et al. (2013)).

1131 **Appendix B Electron Microprobe Techniques and Data Treatment**

1132 **B1 Qualitative X-Ray Mapping**

1133 Qualitative X-Ray compositional maps were acquired on the JEOL JXA-8200 electron
 1134 microprobe at the University of Texas at Austin. Polished $30 \mu\text{m}$ thin sections were analyzed
 1135 using a 15 kV accelerating voltage, focused beam, 300 nA current, $6 \mu\text{m}$ step size, and 1 ms
 1136 dwell time. X-ray maps for Si, Al, Ca, Mg, Fe, Na, K, Mn, Ti, and P were collected. Post-

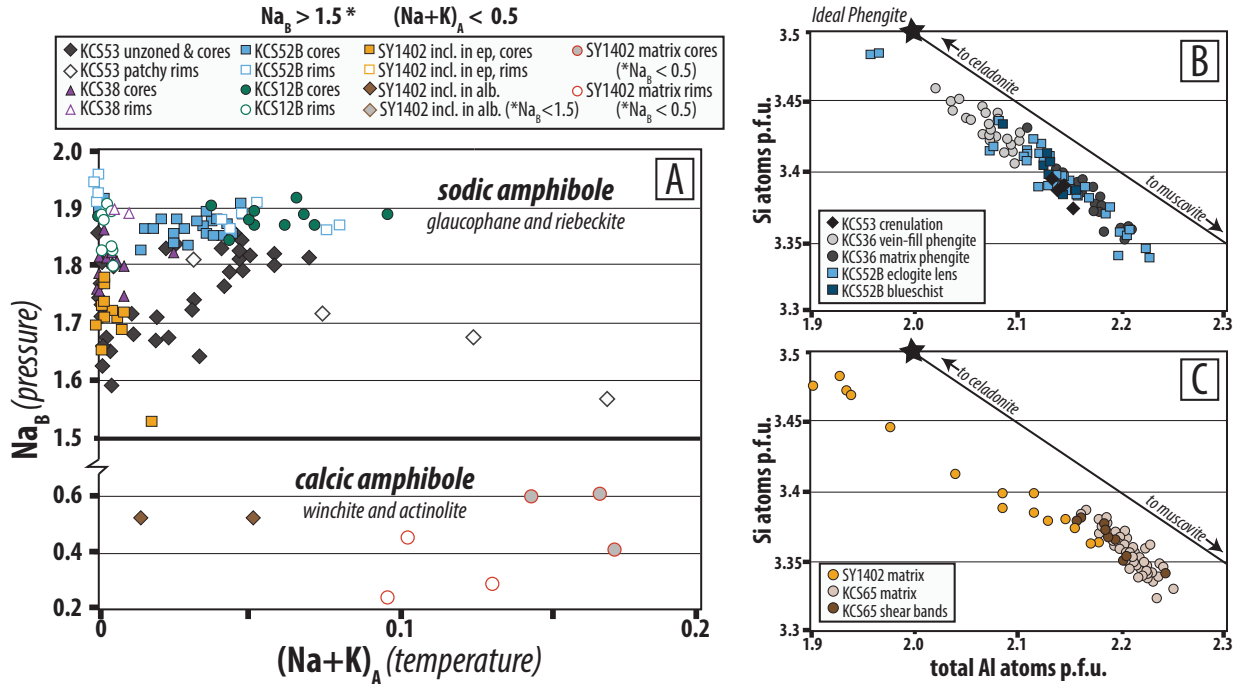


Figure B1: Quantitative EPMA results for (A) amphiboles and (B,C) white micas. (A) Na_B and $(Na+K)_A$ in amphibole are qualitative indicators of pressure and temperature, respectively. Temperature is less reliable since all of these amphiboles are very ‘cold’ (i.e., crystallize at $<500^\circ$). Sodic amphiboles correspond to D_S and D_{T1} , and calcic amphiboles correspond to D_{T2} ; see text for significance of core-rim zonation and compositional trends during deformation. (B) D_S and D_{T1} white mica chemistry. Elevated Si apfu indicates HP metamorphism. (C) D_{T2} white mica chemistry. Grains cluster towards a lower Si apfu on average, which reflects more pervasive recrystallization under lower P conditions. Intergrown phengite and paragonite is common during all deformation stages. CBU samples do not contain the limiting assemblage required for Si-in-phengite geobarometry calibrated by (Massonne & Schreyer, 1987). However, they do contain other stable Fe-Mg buffering phases (e.g., epidote, amphibole), so within a given sample and between samples of similar bulk compositions, Si variability is a reasonable measure of *relative* changes in pressure, not absolute. Samples in (B) are all meta-mafics, SY1402 in (C) is meta-mafic, KCS65 in (C) is a quartz-rich mixed meta-volcanic/meta-sediment.

1137 processing to produce false color compositional maps creation was done in ImageJ software
 1138 by merging element channels with assigned colors.

1139 B2 Quantitative Point Analyses

1140 Quantitative analyses were collected for representative amphiboles and micas on the
 1141 JEOL JXA-8200 electron microprobe at the University of Texas at Austin. Samples were
 1142 selected to cover the range of interpreted structural contexts determined during field work
 1143 and microstructural analysis. Polished $30\ \mu\text{m}$ thin sections were analyzed using a 15 kV
 1144 accelerating voltage, a $1\ \mu\text{m}$ beam diameter amphibole and a $10\ \mu\text{m}$ beam diameter for mica,
 1145 10 nA current, and counting time 30 s for all elements. Synthetic compounds and homoge-
 1146 neous minerals were used as standards, and secondary standards were analyzed throughout
 1147 analytical procedures. Data were processed using the JEOL ZAF procedure.

Sample:	KCS53	n=30	KCS53	n=6	KCS53	n=4	KCS53	n=10	KCS38	n=14	KCS38	n=2	KCS52B	n=21	KCS52B	n=4	KCS52B	n=8	KCS52B	n=3
Context:	matrix cores	cren. limb cores	cren. limb rims	cren. hinges	matrix cores	matrix cores	matrix rims	ecl. rims	ecl. cores	ecl. rims	matrix cores	matrix rims	ecl. rims	matrix cores	matrix rims	matrix cores	matrix rims	matrix cores	matrix rims	
SiO2	58.71	0.54	58.67	0.32	57.09	1.04	58.60	0.18	59.25	0.22	58.87	0.30	58.54	0.49	58.07	0.20	58.53	0.33	58.03	0.42
Al2O3	11.23	0.20	11.07	0.05	11.00	0.12	11.07	0.15	11.78	0.26	11.59	0.13	10.83	0.72	10.11	0.10	11.26	0.20	10.72	0.43
K2O	0.01	0.01	0.01	0.01	0.03	0.02	0.01	0.01	0.01	0.01	0.00	0.00	0.00	0.01	0.00	0.00	0.01	0.00	0.00	0.00
Na2O	6.54	0.24	7.06	0.11	6.80	0.29	7.13	0.11	6.93	0.16	7.21	0.04	7.20	0.10	7.13	0.01	7.26	0.09	7.22	0.09
CaO	0.97	0.38	0.80	0.14	1.54	0.87	0.70	0.23	0.91	0.16	0.20	0.01	0.32	0.18	0.13	0.04	0.34	0.12	0.12	0.08
MnO	0.06	0.04	0.04	0.01	0.10	0.05	0.05	0.02	0.03	0.02	0.09	0.01	0.11	0.08	0.19	0.02	0.06	0.03	0.17	0.06
FeO	9.16	0.55	9.02	0.18	10.19	0.53	9.33	0.43	7.71	0.50	11.05	0.53	11.09	2.27	14.25	0.23	9.39	0.79	11.95	0.66
MgO	11.43	0.37	11.64	0.21	11.30	0.62	11.52	0.41	11.65	0.51	9.67	0.28	10.28	1.16	8.68	0.04	11.04	0.50	9.59	0.48
TiO2	0.03	0.03	0.00	0.01	0.02	0.03	0.02	0.03	0.02	0.02	0.03	0.01	0.01	0.02	0.02	0.02	0.01	0.02	0.01	0.02
Cr2O3	0.02	0.02	0.02	0.02	0.00	0.00	0.02	0.02	0.01	0.02	0.00	0.00	0.01	0.02	0.03	0.01	0.02	0.02	0.00	0.01
Total	97.89	0.47	98.30	0.26	98.05	0.13	98.44	0.25	98.29	0.49	98.68	0.26	98.37	0.27	98.58	0.15	97.88	0.31	97.79	0.71
Si	7.96	0.05	7.94	0.03	7.81	0.12	7.92	0.03	7.97	0.05	8.00	0.00	7.97	0.02	7.99	0.02	7.96	0.02	7.97	0.02
Al (iv)	0.04	0.04	0.06	0.03	0.19	0.12	0.08	0.03	0.04	0.04	0.00	0.00	0.03	0.02	0.01	0.02	0.04	0.02	0.03	0.02
K (A)	0.00	0.00	0.00	0.00	0.00	0.00	0.00	0.00	0.00	0.00	0.00	0.00	0.00	0.00	0.00	0.00	0.00	0.00	0.00	0.00
Na (A)	0.01	0.01	0.04	0.01	0.10	0.05	0.05	0.01	0.01	0.01	0.01	0.00	0.02	0.02	0.00	0.00	0.04	0.01	0.01	0.02
Na (B)	1.71	0.06	1.81	0.02	1.70	0.12	1.82	0.03	1.80	0.04	1.89	0.00	1.88	0.04	1.90	0.00	1.88	0.02	1.91	0.04
Ca (B)	0.14	0.06	0.12	0.02	0.23	0.13	0.10	0.03	0.13	0.02	0.03	0.00	0.05	0.03	0.02	0.01	0.05	0.02	0.02	0.01
Mn (B, 2+)	0.01	0.00	0.00	0.00	0.01	0.01	0.01	0.00	0.00	0.00	0.01	0.00	0.01	0.01	0.02	0.00	0.01	0.00	0.02	0.01
Fe (B, 2+)	0.11	0.04	0.07	0.01	0.06	0.01	0.07	0.02	0.04	0.04	0.07	0.00	0.06	0.03	0.05	0.01	0.07	0.02	0.05	0.04
Fe (C, 2+)	0.91	0.06	0.82	0.05	0.91	0.09	0.83	0.08	0.81	0.09	1.16	0.05	1.02	0.19	1.32	0.04	0.89	0.09	1.11	0.05
Fe (C, 3+)	0.02	0.03	0.13	0.04	0.20	0.05	0.16	0.04	0.01	0.02	0.03	0.01	0.19	0.13	0.27	0.05	0.11	0.03	0.21	0.10
Al (C, vi)	1.75	0.05	1.70	0.03	1.58	0.10	1.69	0.04	1.83	0.02	1.85	0.01	1.71	0.09	1.63	0.03	1.76	0.03	1.71	0.04
Mg (C)	2.31	0.07	2.35	0.05	2.31	0.13	2.32	0.08	2.34	0.09	1.96	0.05	2.08	0.22	1.78	0.01	2.24	0.09	1.97	0.08
Type	Glauco-phane	Glauco-phane	Glauco-phane	Glauco-phane	Glauco-phane	Glauco-phane	Glauco-phane	Glauco-phane	Glauco-phane	Glauco-phane	Glauco-phane	Glauco-phane	Mg-Riebeckite	Glauco-phane						

Table B1: Amphibole mineral chemistry. Reported values are averages of the number of spots indicated by *n* values for each sample and micro-textural context. Uncertainties reflect the range of measured values for each micro-textural context as indicated. Cations per formula unit are calculated for ideal element partitioning for 23 Oxygen atoms.

Sample:	KCS52B $n=6$		KCS52B $n=7$		KCS12B $n=11$		KCS12B $n=8$		SY1402 $n=8$		SY1402 $n=10$		SY1402 $n=1$		SY1402 $n=2$		SY1402 $n=3$		SY1402 $n=2$	
	ps. cores	ps. rims	ps. rims	matrix cores	matrix rims	matrix rims	incl. in ep. cores	incl. in ep. rims	incl. in alb (A)	incl. in alb (B)	matrix cores	matrix rims	matrix cores	matrix rims	matrix cores	matrix rims	matrix cores	matrix rims	matrix cores	matrix rims
SiO ₂	58.58	0.20	57.72	0.42	56.32	0.22	54.03	0.63	57.78	0.15	57.30	0.69	58.28	56.52	1.24	54.13	0.26	54.93	0.96	
Al ₂ O ₃	11.35	0.13	10.65	0.44	10.72	0.38	4.92	1.61	8.12	0.87	8.45	1.28	8.05	2.80	0.89	3.12	0.16	2.23	0.60	
K ₂ O	0.00	0.01	0.00	0.00	0.00	0.00	0.02	0.01	0.02	0.01	0.03	0.03	0.05	0.19	0.14	0.12	0.03	0.09	0.03	
Na ₂ O	7.18	0.06	7.24	0.08	7.09	0.14	6.65	0.22	6.50	0.21	6.39	0.33	6.45	1.89	0.06	2.49	0.40	1.32	0.17	
CaO	0.48	0.06	0.24	0.13	0.29	0.11	0.66	0.33	0.73	0.33	0.93	0.88	1.14	8.92	0.23	8.58	0.99	10.80	0.26	
MnO	0.05	0.01	0.14	0.06	0.06	0.03	0.14	0.03	0.15	0.07	0.16	0.07	0.21	0.32	0.01	0.40	0.05	0.38	0.03	
FeO	9.08	0.27	12.51	1.43	16.93	0.49	25.10	2.03	15.28	1.08	15.55	1.60	14.41	12.24	1.06	15.64	1.74	12.16	0.79	
MgO	11.23	0.34	9.45	0.66	6.50	0.20	5.85	0.25	9.74	0.48	9.29	0.87	10.32	14.93	1.43	13.92	1.11	16.77	0.74	
TiO ₂	0.01	0.02	0.01	0.03	0.02	0.03	0.02	0.02	0.02	0.03	0.03	0.03	0.00	0.00	0.00	0.02	0.01	0.01	0.01	
Cr ₂ O ₃	0.00	0.00	0.01	0.02	0.01	0.01	0.00	0.00	0.00	0.00	0.00	0.00	0.00	0.00	0.00	0.00	0.00	0.00	0.00	
Total	97.92	0.45	97.93	0.33	97.92	0.29	97.35	0.36	98.33	0.41	98.11	0.62	98.91	97.80	0.85	98.42	0.20	98.69	0.42	
Si	7.95	0.02	7.95	0.02	7.93	0.04	7.85	0.04	8.01	0.04	7.98	0.07	8.01	8.01	0.05	7.73	0.06	7.74	0.08	
Al (iv)	0.05	0.02	0.05	0.02	0.07	0.04	0.15	0.04	0.01	0.02	0.03	0.05	0.00	0.02	0.02	0.27	0.06	0.26	0.08	
K (A)	0.00	0.00	0.00	0.00	0.00	0.00	0.00	0.00	0.00	0.00	0.01	0.00	0.01	0.03	0.03	0.02	0.00	0.02	0.00	
Na (A)	0.03	0.01	0.04	0.03	0.05	0.02	0.00	0.00	0.00	0.00	0.00	0.00	0.00	0.00	0.00	0.14	0.02	0.10	0.02	
Na (B)	1.86	0.01	1.89	0.03	1.88	0.02	1.87	0.05	1.75	0.05	1.73	0.09	1.72	0.52	0.01	0.55	0.12	0.26	0.03	
Ca (B)	0.07	0.01	0.04	0.02	0.04	0.02	0.10	0.05	0.11	0.05	0.14	0.13	0.17	1.35	0.01	1.31	0.15	1.63	0.03	
Mn (B, 2+)	0.01	0.00	0.02	0.01	0.01	0.00	0.02	0.00	0.02	0.01	0.02	0.01	0.02	0.04	0.00	0.05	0.01	0.05	0.00	
Fe (B, 2+)	0.07	0.02	0.06	0.02	0.07	0.02	0.01	0.01	0.11	0.02	0.10	0.04	0.08	0.05	0.03	0.09	0.03	0.06	0.00	
Fe (C, 2+)	0.86	0.06	1.16	0.15	1.74	0.06	1.71	0.06	1.28	0.12	1.35	0.15	1.20	1.36	0.16	1.38	0.16	1.07	0.05	
Fe (C, 3+)	0.10	0.03	0.22	0.08	0.18	0.03	1.33	0.28	0.39	0.16	0.36	0.18	0.38	0.03	0.05	0.40	0.05	0.30	0.06	
Al (C, vi)	1.77	0.02	1.68	0.06	1.71	0.04	0.69	0.29	1.32	0.13	1.36	0.17	1.31	0.45	0.13	0.26	0.05	0.11	0.03	
Mg (C)	2.27	0.06	1.94	0.12	1.36	0.04	1.27	0.05	2.01	0.10	1.93	0.17	2.12	3.15	0.25	2.96	0.23	3.52	0.13	
Type	<i>Glaucophane</i>	<i>Glaucophane</i>	<i>Glaucophane</i>	<i>Riebeckite</i>	<i>Riebeckite</i>	<i>Riebeckite</i>	<i>Riebeckite</i>	<i>Riebeckite</i>	<i>Mg-Riebeckite</i>	<i>Mg-Riebeckite</i>	<i>Mg-Riebeckite</i>	<i>Mg-Riebeckite</i>	<i>Mg-Riebeckite</i>	<i>Mg-Riebeckite</i>	<i>Winchite</i>	<i>Fe-Winchite</i>	<i>Actinolite</i>			

Table B1: Continued. Amphibole mineral chemistry. Reported values are averages of the number of spots indicated by n values for each sample and micro-textural context. Uncertainties reflect the range of measured values for each micro-textural context as indicated. Cations per formula unit are calculated for ideal element partitioning for 23 Oxygen atoms.

1148

B3 Mineral classification and formula unit calculations

1149

1150

1151

1152

1153

1154

1155

1156

1157

1158

1159

1160

Quantitative point analyses for amphiboles and white micas were converted from oxide percentage to atoms per formula unit on the basis of $22\text{O} + 2\text{OH}$, and $10\text{O} + 2\text{OH}$ Oxygen atoms, respectively. Amphibole sub-groups and species were determined following recommendations of the Commission on New Minerals Nomenclature and Classification (CNMNC) of the International Mineralogical Association (IMA) (Hawthorne et al., 2012), and species names follow the (Leake et al., 1997) classification scheme. Classifications did not assume initial M-site³⁺/ σ M-site ratios, so ferric iron components were estimated based on charge balance by adjusting valences of Fe and Mn by automatically normalizing the cations. Data shown here commonly fell into the “sum Si to Ca=15”, “sum Si to Mg=13”, and “sum Si to Na=15” normalization schemes (Hawthorne et al., 2012). Hydroxyl contents were not estimated using $\text{OH}=2-2\text{Ti}$, and initial H_2O contents were not required for calculations. White mica ferric iron was ignored in formula calculations.

1161

Appendix C Supplemental Field Photos

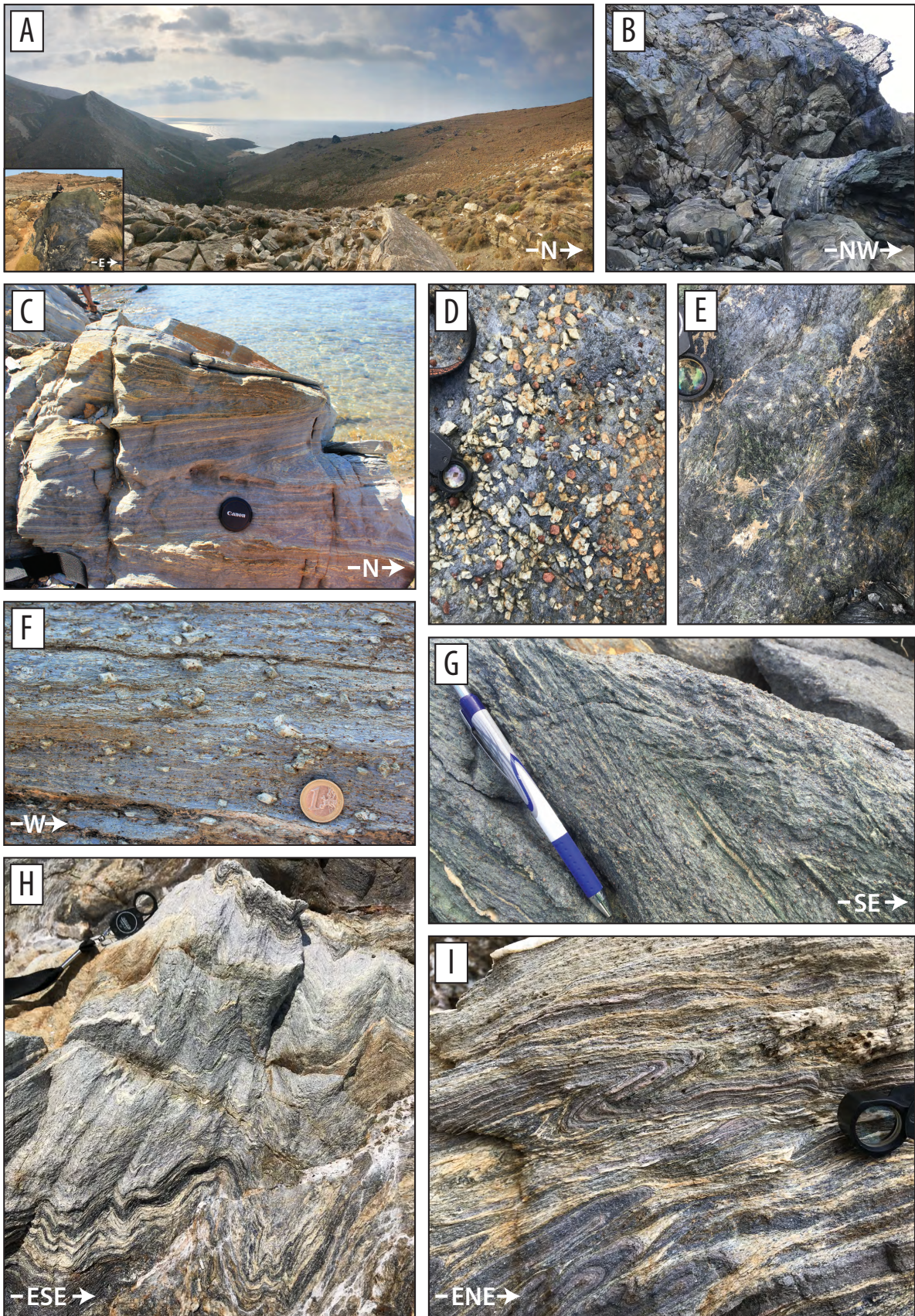


Figure C1: Caption to follow.

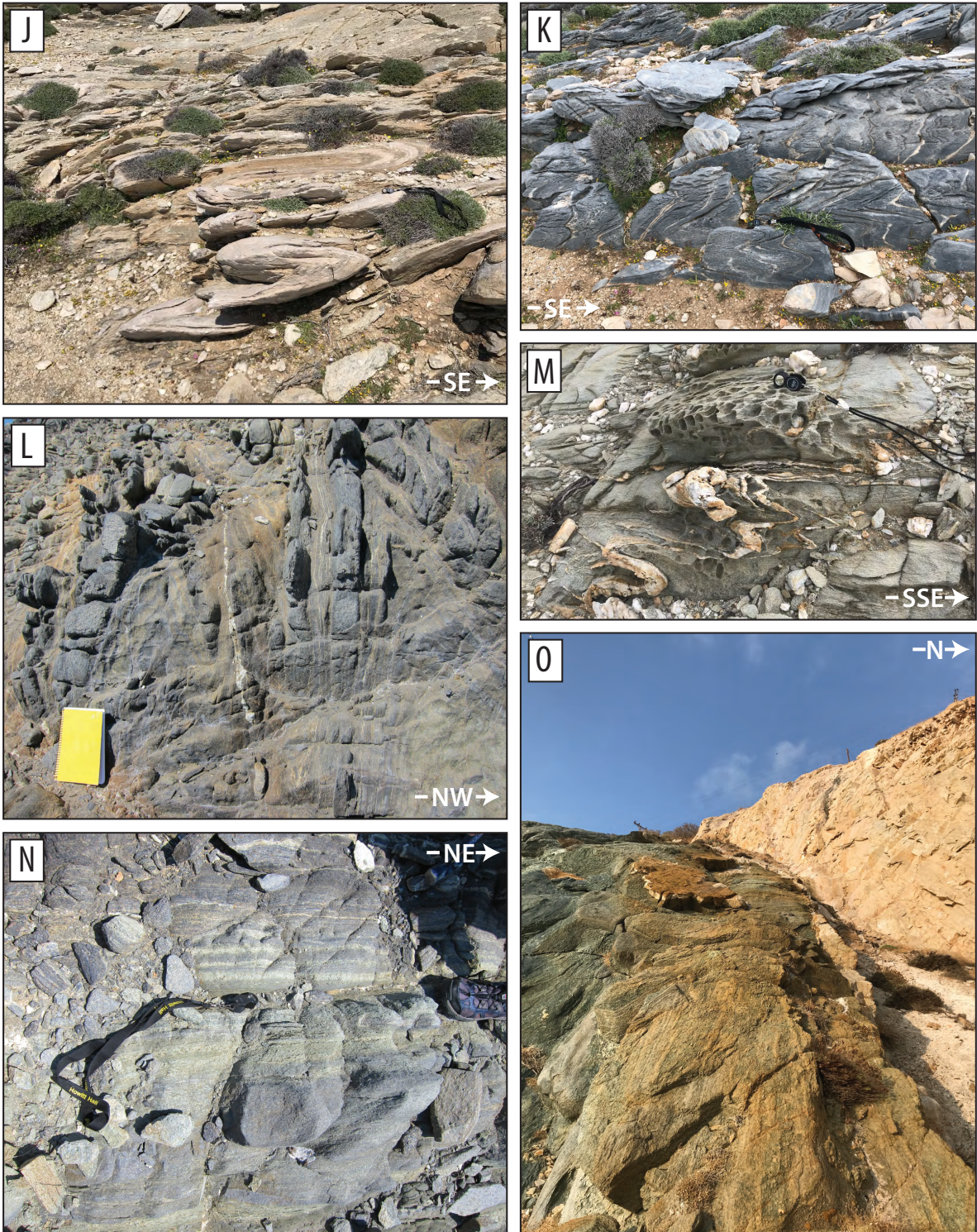


Figure C1: Caption to follow.

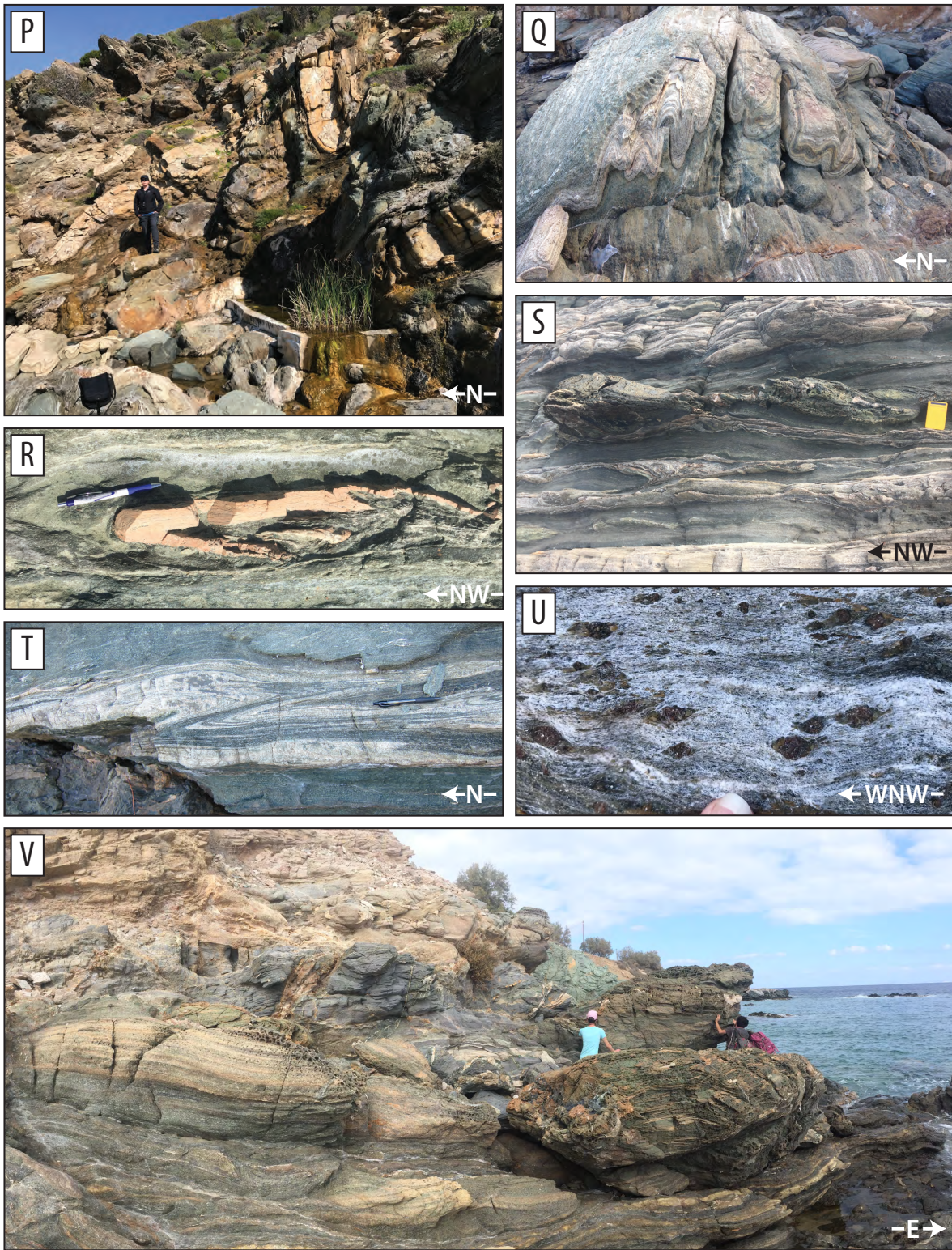


Figure C1: Caption next page.

Figure C1: (Previous pages.) Supplemental field photographs. (A) Eclogitic meta-gabbro 'blocks' pepper the Kampos Belt landscape, and are wrapped by coherent bimodal meta-volcanics (cropping out as resistant ledges in the background). Marbles in the foreground dip down towards the coastline and are structurally concordant with Belt rocks. This is a thrust contact that may have been reworked slightly during exhumation via extension, but we did not see evidence for strongly localized top-to-the-ENE shear. Inset shows example of Kampos meta-gabbro block with glaucophanite carapace. (B) Example of upright, shallowly NNE-plunging D_S folds on the shoreline W of Kampos Belt. (C) Lia Beach isoclinally-folded blueschists; the older, folded foliation is relict D_R , and isoclinal folding developed during D_S . (D) Unstrained cm-sized lawsonite pseudomorphs in Grizzas blueschist. (E) Zoom-in to margin of a Kampos Belt block showing static, radiating clusters of blue and green amphibole. (F) Unstrained D_S lawsonite pseudomorphs in Lia blueschists. (G) D_{T1} crenulation cross-cutting D_S at Kini. (H) The cores of D_{T1} upright folds in Azolimnos schists have strong axial planar cleavages associated with blueschist-to-greenschist facies retrogression. (I) Earlier D_S fabrics in Azolimnos schists record asymmetric shear in isoclinally-folded schists; pinkish layers are meta-cherts. (J) Isoclinal folds in marbles (foreground) and meta-conglomerates (background) and in meta-mafic greenschists (M) on Palos Peninsula mimic the map-scale folding seen in Fig. 2. (K) Sub-horizontal axial planar cleavages form in dolomitic blue-grey marbles during exhumation-related flattening (coaxial strain). (L) Upright D_{T1} folding at Kalamisia is associated with hinge-parallel greenschist retrogression (N) selectively permeating foliation-parallel layers. (O) Fault contact between marbles and blueschist-eclogite lithologies at Agios Dimitrios. Stretching is directly down-dip (essentially out of the page) and parallel to mullion hinges developed along the contact. Structures on either side of this contact are homogeneous. (P-S, U) Multiple generations of folding at Delfini. (P) Upright D_{T2} folding (discussed in text) develops an axial planar cleavage and hinge-parallel stretching and mineral lineations defined by quartz, epidote, and actinolite (Q). Older D_S foliations contain axial planes of isoclinal folds, best seen by salmon-colored meta-cherts (R) and compositional banding (T). Hinge:limb thickness variations locally exceed 20:1 (T, Lotos). (S) Along the limbs of upright folds like (P), coaxial stretching leads to boudinage of competent lenses. These structures record top-WNW shear, but top-ESE structures occur in roughly equal proportions. (U) Symmetric quartz-filled pressure shadows on delta-type D_S garnet porphyroblasts. (V) Asymmetric, non-coaxial strain during exhumation is limited to localities proximal to the Vari Detachment, like this example from Fabrikas.

1162 **References**

- 1163 Agard, P., Plunder, A., Angiboust, S., Bonnet, G., & Ruh, J. (2018). The subduction
1164 plate interface: rock record and mechanical coupling (from long to short timescales).
1165 *Lithos*, *320*, 537–566.
- 1166 Altherr, R., Kreuzer, H., Lenz, H., Wendt, I., Harre, W., & Dürr, S. (1994). Further evidence
1167 for a Late Cretaceous low-pressure/high-temperature terrane in the Cyclades, Greece.
1168 *Chemie der Erde*, *54*, 319–28.
- 1169 Andriessen, P., Boelrijk, N., Hebeda, E. H., Priem, H., Verdurnen, E., & Verschure, R. H.
1170 (1979). Dating the events of metamorphism and granitic magmatism in the Alpine
1171 orogen of Naxos (Cyclades, Greece). *Contributions to Mineralogy and Petrology*, *69*(3),
1172 215–225. doi: 10.1007/BF00372323
- 1173 Angiboust, S., Agard, P., Glodny, J., Omrani, J., & Oncken, O. (2016). Zagros blueschists:
1174 Episodic underplating and long-lived cooling of a subduction zone. *Earth and Plane-*
1175 *tary Science Letters*, *443*, 48–58.
- 1176 Aoki, K., Itaya, T., Shibuya, T., Masago, H., Kon, Y., Terabayashi, M., ... Maruyama,
1177 S. (2008). The youngest blueschist belt in sw japan: Implication for the exhumation
1178 of the cretaceous sanbagawa high-p/t metamorphic belt. *Journal of Metamorphic*
1179 *Geology*, *26*(5), 583–602.
- 1180 Aravadinou, E., & Xypolias, P. (2017). Evolution of a passive crustal-scale detachment (Sy-
1181 ros, Aegean region): Insights from structural and petrofabric analyses in the hanging-
1182 wall. *Journal of Structural Geology*, *103*, 57–74.
- 1183 Aravadinou, E., Xypolias, P., Chatzaras, V., Iliopoulos, I., & Gerogiannis, N. (2016). Ductile
1184 nappe stacking and refolding in the cycladic blueschist unit: insights from sifnos island
1185 (south aegean sea). *International Journal of Earth Sciences*, *105*(7), 2075–2096.
- 1186 Avigad, D., & Garfunkel, Z. (1989). Low-angle faults above and below a blueschist
1187 belt—Tinos Island, Cyclades, Greece. *Terra Nova*, *1*(2), 182–187.
- 1188 Avigad, D., & Garfunkel, Z. (1991). Uplift and exhumation of high-pressure metamorphic
1189 terrains: the example of the Cycladic blueschist belt (Aegean Sea). *Tectonophysics*,
1190 *188*, 357–372.
- 1191 Baldwin, S. L. (1996). Contrasting PTt histories for blueschists from the western Baja
1192 Terrane and the Aegean: Effects of synsubduction exhumation and backarc extension.
1193 *Washington DC American Geophysical Union Geophysical Monograph Series*, *96*, 135–
1194 141.
- 1195 Ballevre, M., Pitra, P., & Bohn, M. (2003). Lawsonite growth in the epidote blueschists
1196 from the Ile de Groix (Armorican Massif, France): a potential geobarometer. *Journal*
1197 *of metamorphic Geology*, *21*(7), 723–735.
- 1198 Baxter, E. F., & Caddick, M. J. (2013). Garnet growth as a proxy for progressive subduction
1199 zone dehydration. *Geology*, *41*(6), 643–646.
- 1200 Beaumont, C., Jamieson, R. A., Butler, J., & Warren, C. (2009). Crustal structure: A
1201 key constraint on the mechanism of ultra-high-pressure rock exhumation. *Earth and*
1202 *Planetary Science Letters*, *287*(1-2), 116–129.
- 1203 Behr, W. M., Kotowski, A. J., & Ashley, K. T. (2018). Dehydration-induced rheological
1204 heterogeneity and the deep tremor source in warm subduction zones. *Geology*, *46*(5),
1205 475–478.
- 1206 Behr, W. M., & Platt, J. P. (2012). Kinematic and thermal evolution during two-stage
1207 exhumation of a Mediterranean subduction complex. *Tectonics*, *31*(4). doi: 10.1029/
1208 2012TC003121
- 1209 Blake Jr, M. C., Bonneau, M., Geyssant, J., Kienast, J., Lepvrier, C., H., & Papanikolaou,
1210 D. (1981). A geologic reconnaissance of the Cycladic blueschist belt, Greece. *Geological*
1211 *Society of America Bulletin*, *92*(5), 247–254.
- 1212 Bolhar, R., Ring, U., & Allen, C. M. (2010). An integrated zircon geochronological and geo-
1213 chemical investigation into the miocene plutonic evolution of the cyclades, aegean sea,
1214 greece: Part 1: Geochronology. *Contributions to Mineralogy and Petrology*, *160*(5),
1215 719–742.

- 1271 of HP mélanges from Tinos and Andros, Cycladic blueschist belt, Greece. *Lithos*,
1272 *117*(1-4), 61–81.
- 1273 Burov, E., Francois, T., Yamato, P., & Wolf, S. (2014). Mechanisms of continental subduc-
1274 tion and exhumation of HP and UHP rocks. *Gondwana Research*, *25*(2), 464–493.
- 1275 Calvert, A. J., Preston, L. A., & Farahbod, A. M. (2011). Sedimentary underplating at the
1276 cascadia mantle-wedge corner revealed by seismic imaging. *Nature Geoscience*, *4*(8),
1277 545–548.
- 1278 Chemenda, A., Mattauer, M., Malavieille, J., & Bokun, A. (1995, jan). A mechanism for
1279 syn-collisional rock exhumation and associated normal faulting: Results from physical
1280 modelling. *Earth and Planetary Science Letters*, *132*, 225–232. Retrieved from
1281 [http://linkinghub.elsevier.com/retrieve/pii/0012821X9500042Bpapers3://](http://linkinghub.elsevier.com/retrieve/pii/0012821X9500042Bpapers3://publication/uuid/24846994-FAB6-4147-8883-2A2B9B1D53B5)
1282 [publication/uuid/24846994-FAB6-4147-8883-2A2B9B1D53B5](http://linkinghub.elsevier.com/retrieve/pii/0012821X9500042Bpapers3://publication/uuid/24846994-FAB6-4147-8883-2A2B9B1D53B5)
- 1283 Cisneros, M., Barnes, J., Behr, W. M., Kotowski, A. J., Stockli, D., & Soukis, K. (in press).
1284 Insights from elastic thermobarometry into exhumation of high-pressure metamorphic
1285 rocks from syros, greece. *Solid Earth*.
- 1286 Cliff, R. A., Bond, C. E., Butler, R. W. H., & Dixon, J. E. (2016, dec). Geochrono-
1287 logical challenges posed by continuously developing tectonometamorphic systems; in-
1288 sights from Rb–Sr mica ages from the Cycladic Blueschist Belt, Syros (Greece). *J.*
1289 *Metamorph. Geol.*, doi:10.1111/jmg.12228. Retrieved from [http://doi.wiley.com/](http://doi.wiley.com/10.1111/jmg.12228)
1290 [10.1111/jmg.12228](http://doi.wiley.com/10.1111/jmg.12228) doi: 10.1111/jmg.12228
- 1291 Cliff, R. A., & Meffan-Main, S. (2003, jan). Evidence from Rb–Sr microsampling
1292 geochronology for the timing of Alpine deformation in the Sonnblick Dome, SE Tauern
1293 Window, Austria. *Geochronology: Linking the Isotopic Record with Petrology and*
1294 *Textures*, 159. Retrieved from [papers3://publication/uuid/08ECF850-E95C-4774-](http://papers3://publication/uuid/08ECF850-E95C-4774-B506-7043EE2BE72A)
1295 [B506-7043EE2BE72A](http://papers3://publication/uuid/08ECF850-E95C-4774-B506-7043EE2BE72A)
- 1296 Cloos, M. (1982, jan). Flow melanges: Numerical modeling and geologic constraints on their
1297 origin in the Franciscan subduction complex, California. *GSA Bulletin*, *93*(4), 330. Re-
1298 trieved from [http://bulletin.geoscienceworld.org/cgi/content/abstract/93/](http://bulletin.geoscienceworld.org/cgi/content/abstract/93/4/330papers3://publication/uuid/388347B7-1AC8-4B74-B3B6-DC5C0E39C06A)
1299 [4/330papers3://publication/uuid/388347B7-1AC8-4B74-B3B6-DC5C0E39C06A](http://bulletin.geoscienceworld.org/cgi/content/abstract/93/4/330papers3://publication/uuid/388347B7-1AC8-4B74-B3B6-DC5C0E39C06A)
- 1300 Cloos, M. (1986). Blueschists in the Franciscan Complex of California: Petrotectonic
1301 constraints on uplift mechanisms. In *Blueschists and eclogites* (Vol. 164, pp. 77–93).
1302 Geological Society of America Memoir.
- 1303 Cooperdock, E. H., Raia, N. H., Barnes, J. D., Stockli, D. F., & Schwarzenbach, E. M.
1304 (2018). Tectonic origin of serpentinites on Syros, Greece: Geochemical signatures of
1305 abyssal origin preserved in a HP/LT subduction complex. *Lithos*, *296*, 352–364.
- 1306 Dixon, J. E. (1976). Glaucophane schists of Syros, Greece. *Bulletin de la Société géologique*
1307 *de France*, *7*(2), 280.
- 1308 Dixon, J. E., & Ridley, J. (1987). Syros. In *Chemical transport in metasomatic processes*
1309 (Vol. 218, pp. 489–501). Reidel Publishing Company Dordrecht.
- 1310 Dragovic, B., Baxter, E. F., & Caddick, M. J. (2015). Pulsed dehydration and garnet
1311 growth during subduction revealed by zoned garnet geochronology and thermodynamic
1312 modeling, Sifnos, Greece. *Earth and Planetary Science Letters*, *413*, 111–122.
- 1313 Dragovic, B., Samanta, L. M., Baxter, E. F., & Selverstone, J. (2012). Using garnet
1314 to constrain the duration and rate of water-releasing metamorphic reactions during
1315 subduction: An example from Sifnos, Greece. *Chemical Geology*, *314*, 9–22.
- 1316 Dürr, S., Altherr, R., Keller, J., Okrusch, M., & Seidel, E. (1978). The median Aegean
1317 crystalline belt: stratigraphy, structure, metamorphism, magmatism. *Alps, Apen-*
1318 *nines, Hellenides*, *38*, 455–476.
- 1319 Ernst, W., & Liu, J. (1998). Experimental phase-equilibrium study of Al- and Ti-contents
1320 of calcic amphibole in MORB—a semiquantitative thermobarometer. *American min-*
1321 *eralogist*, *83*(9-10), 952–969.
- 1322 Evans, B. W. (1990). Phase relations of epidote-blueschists. *Lithos*, *25*(1-3), 3–23. doi:
1323 [10.1016/0024-4937\(90\)90003-J](https://doi.org/10.1016/0024-4937(90)90003-J)
- 1324 Fagereng, Å., Savage, H., Morgan, J., Wang, M., Meneghini, F., Barnes, P., ... others
1325 (2019). Mixed deformation styles observed on a shallow subduction thrust, hikurangi

- margin, new zealand. *Geology*, 47(9), 872–876.
- 1326 Flansburg, M. E., Stockli, D. F., Poulaki, E. M., & Soukis, K. (2019). Tectono-magmatic
1327 and stratigraphic evolution of the Cycladic Basement, Ios Island, Greece. *Tectonics*.
1328
- 1329 Forster, M., Koudashev, O., Nie, R., Yeung, S., & Lister, G. (2020). 40Ar/39Ar ther-
1330 mochronology in the ios basement terrane resolves the tectonic significance of the
1331 south cyclades shear zone. *Geological Society, London, Special Publications*, 487(1),
1332 291–313.
- 1333 Forster, M., & Lister, G. (2005). Several distinct tectono-metamorphic slices in the Cycladic
1334 eclogite–blueschist belt, Greece. *Contributions to Mineralogy and Petrology*, 150(5),
1335 523–545.
- 1336 Forster, M., & Lister, G. (2008). Tectonic sequence diagrams and the structural evolution of
1337 schists and gneisses in multiply deformed terranes. *Journal of the Geological Society*,
1338 165(5), 923–939.
- 1339 Freeman, S., Inger, S., Butler, R., & Cliff, R. A. (1997, jan). Dating deformation using
1340 Rb-Sr in white mica: Greenschist facies deformation ages *Tectonics*. Retrieved
1341 from [http://europa.agu.org/?uri=/journals/tc/96TC02477.xml{\&}view=](http://europa.agu.org/?uri=/journals/tc/96TC02477.xml{\&}view=articlepapers3://publication/uuid/E7B4274F-FDB0-40E7-8266-BBD52B38F230)
1342 [articlepapers3://publication/uuid/E7B4274F-FDB0-40E7-8266-BBD52B38F230](http://europa.agu.org/?uri=/journals/tc/96TC02477.xml{\&}view=articlepapers3://publication/uuid/E7B4274F-FDB0-40E7-8266-BBD52B38F230)
- 1343 Fu, B., Bröcker, M., Ireland, T., Holden, P., & Kinsley, L. P. (2015). Zircon U–Pb, O, and
1344 Hf isotopic constraints on Mesozoic magmatism in the Cyclades, Aegean Sea, Greece.
1345 *International Journal of Earth Sciences*, 104(1), 75–87.
- 1346 Fu, B., Paul, B., Cliff, J., Bröcker, M., & Bulle, F. (2012). O–Hf isotope constraints on
1347 the origin of zircon in high-pressure melange blocks and associated matrix rocks from
1348 Tinos and Syros, Greece. *European Journal of Mineralogy*, 24(2), 277–287.
- 1349 Gautier, P., Brun, J.-P., & Jolivet, L. (1993). Structure and kinematics of upper cenozoic
1350 extensional detachment on naxos and paros (cyclades islands, greece). *Tectonics*,
1351 12(5), 1180–1194.
- 1352 Gerya, T. V., & Stöckhert, B. (2002, jan). Exhumation rates of high pressure metamorphic
1353 rocks in subduction channels: the effect of rheology. *Geophysical Research Letters*,
1354 29(8), 1261. Retrieved from [papers3://publication/uuid/B673D8A0-155B-43D0-](http://papers3://publication/uuid/B673D8A0-155B-43D0-B5CF-7026FE19896B)
1355 [B5CF-7026FE19896B](http://papers3://publication/uuid/B673D8A0-155B-43D0-B5CF-7026FE19896B)
- 1356 Gerya, T. V., Stöckhert, B., & Perchuk, A. L. (2002, jan). Exhumation of high-pressure
1357 metamorphic rocks in a subduction channel: A numerical simulation. *Tectonics*, 21(6),
1358 doi:10.1029/2002TC001406. Retrieved from [http://www.agu.org/pubs/crossref/](http://www.agu.org/pubs/crossref/2002/2002TC001406.shtmlpapers3://publication/doi/10.1029/2002TC001406)
1359 [2002/2002TC001406.shtmlpapers3://publication/doi/10.1029/2002TC001406](http://www.agu.org/pubs/crossref/2002/2002TC001406.shtmlpapers3://publication/doi/10.1029/2002TC001406)
- 1360 Gessner, K., Gallardo, L. A., Markwitz, V., Ring, U., & Thomson, S. N. (2013). What
1361 caused the denudation of the menderes massif: Review of crustal evolution, lithosphere
1362 structure, and dynamic topography in southwest turkey. *Gondwana research*, 24(1),
1363 243–274.
- 1364 Glodny, J., Austrheim, H., Molina, J. F., Rusin, A. I., & Seward, D. (2003). Rb/sr record
1365 of fluid-rock interaction in eclogites: The marun-keu complex, polar urals, russia.
1366 *Geochimica et Cosmochimica Acta*, 67(22), 4353–4371.
- 1367 Glodny, J., Kühn, A., & Austrheim, H. (2008, jan). Diffusion versus recrystallization
1368 processes in Rb–Sr geochronology: Isotopic relics in *Geochimica et Cosmochim-*
1369 *ica Acta*. Retrieved from [http://linkinghub.elsevier.com/retrieve/pii/](http://linkinghub.elsevier.com/retrieve/pii/S0016703707006345papers3://publication/uuid/9FE00F83-E636-43B0-9933-35B5FCBFE721)
1370 [S0016703707006345papers3://publication/uuid/9FE00F83-E636-43B0-9933-](http://linkinghub.elsevier.com/retrieve/pii/S0016703707006345papers3://publication/uuid/9FE00F83-E636-43B0-9933-35B5FCBFE721)
1371 [35B5FCBFE721](http://linkinghub.elsevier.com/retrieve/pii/S0016703707006345papers3://publication/uuid/9FE00F83-E636-43B0-9933-35B5FCBFE721)
- 1372 Glodny, J., Ring, U., Kühn, A., Gleissner, P., & Franz, G. (2005, may). Crystal-
1373 lization and very rapid exhumation of the youngest Alpine eclogites (Tauern
1374 Window, Eastern Alps) from Rb/Sr mineral assemblage analysis. *Con-*
1375 *tributions to Mineralogy and Petrology*, 149(6), 699–712. Retrieved from
1376 [http://www.springerlink.com/index/U5PW505180300421.pdfpapers3://](http://www.springerlink.com/index/U5PW505180300421.pdfpapers3://publication/doi/10.1007/s00410-005-0676-5)
1377 [publication/doi/10.1007/s00410-005-0676-5](http://www.springerlink.com/index/U5PW505180300421.pdfpapers3://publication/doi/10.1007/s00410-005-0676-5)
- 1378 Grasemann, B., Schneider, D. A., Stockli, D. F., Iglseder, C., Stöckli, D. F.,
1379 & Iglseder, C. (2012, jan). Miocene bivergent crustal extension in the
1380 Aegean: Evidence from the western Cyclades (Greece). *Lithosphere*, 4(1), 23–

- 1381 39. Retrieved from <http://lithosphere.gsapubs.org/cgi/doi/10.1130/L164>
1382 .1papers3://publication/doi/10.1130/L164.1
- 1383 Halama, R., Glodny, J., Konrad-Schmolke, M., & Sudo, M. (2018). Rb-sr and in situ
1384 40ar/39ar dating of exhumation-related shearing and fluid-induced recrystallization
1385 in the sesia zone (western alps, italy). *Geosphere*, 14(4), 1425–1450.
- 1386 Hawthorne, F. C., Oberti, R., Harlow, G. E., Maresch, W. V., Martin, R. F., Schumacher,
1387 J. C., & Welch, M. D. (2012). Nomenclature of the amphibole supergroup. *American*
1388 *Mineralogist*, 97(11-12), 2031–2048.
- 1389 Hecht, J. (1985). Geological map of Greece 1: 50 000, Syros island. *Institute of Geology*
1390 *and Mineral Exploration, Athens*.
- 1391 Huet, B., Labrousse, L., & Jolivet, L. (2009). Thrust or detachment? exhumation processes
1392 in the aegean: Insight from a field study on ios (Cyclades, Greece). *Tectonics*, 28(3).
1393 doi: 10.1029/2008TC002397
- 1394 Inger, S., & Cliff, R. (1994). Timing of metamorphism in the tauern window, eastern alps:
1395 Rb-sr ages and fabric formation. *Journal of metamorphic Geology*, 12(5), 695–707.
- 1396 Jacobshagen, V. (1986). Geologie von Griechenland: Gebrüder Borntraeger. *Berlin-*
1397 *Stuttgart*, 363pp.
- 1398 Jolivet, L., & Brun, J. P. (2010). Cenozoic geodynamic evolution of the Aegean. *Internat-*
1399 *ional Journal of Earth Sciences*, 99(1), 109–138. doi: 10.1007/s00531-008-0366-4
- 1400 Jolivet, L., Faccenna, C., Goffé, B., Burov, E. B., & Agard, P. (2003,
1401 jan). Subduction tectonics and exhumation of high-pressure metamorphic
1402 rocks in the Mediterranean orogens. *American Journal of Science*, 303(5),
1403 353–409. Retrieved from [http://ajsonline.org/cgi/content/abstract/303/5/
1404 353papers3://publication/uuid/313C27F4-1B1D-49D2-A7A3-953D704E5793](http://ajsonline.org/cgi/content/abstract/303/5/353papers3://publication/uuid/313C27F4-1B1D-49D2-A7A3-953D704E5793)
- 1405 Jolivet, L., Faccenna, C., Huet, B., Labrousse, L., Le Pourhiet, L., Lacombe, O., ... Driussi,
1406 O. (2013). Aegean tectonics: Strain localisation, slab tearing and trench retreat.
1407 *Tectonophysics*, 597-598, 1–33. doi: 10.1016/j.tecto.2012.06.011
- 1408 Jolivet, L., Trotet, F., Monie, P., Vidal, O., Goffé, B., Labrousse, L., ... Ghorbal, B.
1409 (2010, jan). Along-strike variations of PT conditions in accretionary wedges and syn-
1410 orogenic extension, the HP-LT Phyllite-Quartzite Nappe in Crete and the Peloponnese.
1411 *Tectonophysics*, 480(1-4), 133–148. Retrieved from [papers3://publication/uuid/
1412 05D78E1D-3C49-4CA6-98C3-97A752D40E1F](papers3://publication/uuid/05D78E1D-3C49-4CA6-98C3-97A752D40E1F)
- 1413 Keay, S. (1998). *The geological evolution of the Cyclades, Greece: constraints from SHRIMP*
1414 *U-Pb geochronology* (Unpublished doctoral dissertation).
- 1415 Keay, S., & Lister, G. (2002). African provenance for the metasediments and metaigneous
1416 rocks of the Cyclades, Aegean Sea, Greece. *Geology*, 30(3), 235–238.
- 1417 Keiter, M., Ballhaus, C., & Tomaschek, F. (2011). A new geological map of the Island of
1418 Syros (Aegean Sea, Greece): Implications for lithostratigraphy and structural history
1419 of the Cycladic Blueschist Unit. *Geol. Soc. Am. Spec. Pap.*, 481, 1–43.
- 1420 Keiter, M., Piepjohn, K., Ballhaus, C., Lagos, M., & Bode, M. (2004, aug). Struc-
1421 tural development of high-pressure metamorphic rocks on Syros island (Cyclades,
1422 Greece). *Journal of Structural Geology*, 26(8), 1433–1445. Retrieved from [http://
1423 linkinghub.elsevier.com/retrieve/pii/S0191814103002062papers3://
1424 publication/doi/10.1016/j.jsg.2003.11.027http://www.sciencedirect.com/
1425 science/article/pii/S0191814103002062papers3://publication/uuid/
1426 9F769F57-8390-43F0-8D62-C74BBB0F90B4](http://linkinghub.elsevier.com/retrieve/pii/S0191814103002062papers3://publication/doi/10.1016/j.jsg.2003.11.027http://www.sciencedirect.com/science/article/pii/S0191814103002062papers3://publication/uuid/9F769F57-8390-43F0-8D62-C74BBB0F90B4)
- 1427 Kendall, J. (2016). *Sm/nd garnet geochronology and pressure-temperature paths of eclogites*
1428 *from syros, greece: Implications for subduction zone processes and water loss from the*
1429 *subducting slab* (Unpublished doctoral dissertation). Boston College.
- 1430 Kimura, G., Yamaguchi, A., Hojo, M., Kitamura, Y., Kameda, J., Ujiie, K., ... Hina, S.
1431 (2012). Tectonic mélange as fault rock of subduction plate boundary. *Tectonophysics*,
1432 568, 25–38.
- 1433 Kimura, H., Takeda, T., Obara, K., & Kasahara, K. (2010). Seismic evidence for active
1434 underplating below the megathrust earthquake zone in japan. *Science*, 329(5988),
1435 210–212.

- 1436 Kirchner, K. L., Behr, W. M., Loewy, S., & Stockli, D. F. (2016). Early Miocene sub-
 1437 duction in the western Mediterranean, constraints from Rb-Sr multi-mineral isochron
 1438 geochronology. *Geochem. Geophys. Geosyst.*, *17*(5), doi:10.1002/2015GC006208. doi:
 1439 10.1002/2015GC006208
- 1440 Kleine, B. I., Skelton, A. D., Huet, B., & Pitcairn, I. K. (2014). Preservation of
 1441 Blueschist-facies Minerals along a Shear Zone by Coupled Metasomatism and Fast-
 1442 flowing CO₂-bearing Fluids. *Journal of Petrology*, *55*, 1905–1939.
- 1443 Kotowski, A. J., & Behr, W. M. (2019). Length scales and types of heterogeneities along
 1444 the deep subduction interface: Insights from exhumed rocks on Syros Island, Greece.
 1445 *Geosphere*.
- 1446 Kullerød, L. (1991). On the calculation of isochrons. *Chemical Geology: Isotope Geoscience*
 1447 *section*, *87*(2), 115–124.
- 1448 Lagos, M., Scherer, E. E., Tomaschek, F., Münker, C., Keiter, M., Berndt, J., & Ballhaus, C.
 1449 (2007, jan). High precision Lu–Hf geochronology of Eocene eclogite-facies rocks from
 1450 Syros, Cyclades, Greece. *Chemical Geology*, *243*(1), 16–35. Retrieved from [http://](http://www.sciencedirect.com/science/article/pii/S0009254107001751papers3://publication/uuid/77497147-A4FC-4D87-B574-681BE0904700)
 1451 [www.sciencedirect.com/science/article/pii/S0009254107001751papers3://](http://www.sciencedirect.com/science/article/pii/S0009254107001751papers3://publication/uuid/77497147-A4FC-4D87-B574-681BE0904700)
 1452 [publication/uuid/77497147-A4FC-4D87-B574-681BE0904700](http://www.sciencedirect.com/science/article/pii/S0009254107001751papers3://publication/uuid/77497147-A4FC-4D87-B574-681BE0904700)
- 1453 Laird, J., & Albee, A. L. (1981). Pressure, temperature, and time indicators in mafic
 1454 schist; their application to reconstructing the polymetamorphic history of Vermont.
 1455 *American Journal of Science*, *281*(2), 127–175.
- 1456 Lanari, P., & Duisterhoeft, E. (2018). Modeling metamorphic rocks using equilibrium
 1457 thermodynamics and internally consistent databases: past achievements, problems
 1458 and perspectives. *Journal of petrology*, *60*(1), 19–56.
- 1459 Lanari, P., & Engi, M. (2017). Local bulk composition effects on metamorphic mineral
 1460 assemblages. *Reviews in Mineralogy and Geochemistry*, *83*(1), 55–102.
- 1461 Lanari, P., Giuntoli, F., Loury, C., Burn, M., & Engi, M. (2017). An inverse modeling
 1462 approach to obtain P–T conditions of metamorphic stages involving garnet growth
 1463 and resorption. *European Journal of Mineralogy*, *29*(2), 181–199.
- 1464 Laurent, V., Huet, B., Labrousse, L., Jolivet, L., Monie, P., & Augier, R. (2017). Extraneous
 1465 argon in high-pressure metamorphic rocks: Distribution, origin and transport in the
 1466 Cycladic Blueschist Unit (Greece). *Lithos*, *272*, 315–335.
- 1467 Laurent, V., Jolivet, L., Roche, V., Augier, R., Scaillet, S., & Cardello, G. L. (2016). Strain
 1468 localization in a fossilized subduction channel: Insights from the Cycladic Blueschist
 1469 Unit (Syros, Greece). *Tectonophysics*, *672*(150-169). doi: 10.1016/j.tecto.2016.01.036
- 1470 Laurent, V., Lanari, P., Nair, I., Augier, R., Lahfid, A., & Jolivet, L. (2018). Exhuma-
 1471 tion of eclogite and blueschist (Cyclades, Greece): Pressure–Temperature evolution
 1472 determined by thermobarometry and garnet equilibrium modelling. *Journal of Meta-*
 1473 *morphic Geology*.
- 1474 Leake, B. E., Wooley, A. R., Arps, C. E., Birch, W. D., Gilbert, M. C., Grice, J. D., ...
 1475 others (1997). Nomenclature of amphiboles; report of the subcommittee on amphiboles
 1476 of the international mineralogical association commission on new minerals and mineral
 1477 names. *European Journal of Mineralogy*, *9*(3), 623–651.
- 1478 Liou, J. (1971). P–T stabilities of laumontite, wairakite, lawsonite, and related minerals
 1479 in the system CaAl₂Si₂O₈-SiO₂-H₂O. *Journal of Petrology*, *12*(2), 379–411.
- 1480 Lister, G., Banga, G., & Feenstra, A. (1984). Metamorphic core complexes of Cordilleran
 1481 type in the Cyclades, Aegean Sea, Greece. *Geology*, *12*, 221–225.
- 1482 Lister, G., & Forster, M. (2016). White mica ⁴⁰Ar/³⁹Ar age spectra and the timing of
 1483 multiple episodes of high-P metamorphic mineral growth in the Cycladic eclogite–
 1484 blueschist belt, Syros, Aegean Sea, Greece. *Journal of Metamorphic Geology*, *34*(5),
 1485 401–421.
- 1486 Liu, F., Gerdes, A., Liou, J., Xue, H., & Liang, F. (2006). Shrimp U–Pb zircon dating
 1487 from sulu-dabie dolomitic marble, eastern china: constraints on prograde, ultrahigh-
 1488 pressure and retrograde metamorphic ages. *Journal of metamorphic Geology*, *24*(7),
 1489 569–589.
- 1490 Löwen, K., Bröcker, M., & Berndt, J. (2015). Depositional ages of clastic metasediments

- 1491 from Samos and Syros, Greece: results of a detrital zircon study. *International Journal of Earth Sciences*, 104(1), 205–220.
- 1492
- 1493 Ludwig, L., Akciz, S., Noriega, G. R., & Zielke, O. (2010, jan). Climate-Modulated Channel Incision and Rupture History of the San *Science*. Retrieved from http://www.public.asu.edu/~ozielke/research/data/GrantLudwigEtAl{_}Science2010.pdfpapers3://publication/uuid/0CE1AAD1-6E4E-4B5C-B6A5-3FE213DAFB23
- 1494
- 1495
- 1496
- 1497
- 1498 Maluski, H., Bonneau, M., & Kienast, J. R. (1987). Dating the metamorphic events in the Cycladic area; $^{39}\text{Ar}/^{40}\text{Ar}$ data from metamorphic rocks of the Island of Syros (Greece). *Bull. Société Géologique Fr.*, 3, 833–842.
- 1499
- 1500
- 1501 Maruyama, S., Suzuki, K., & Liou, J. (1983). Greenschist–amphibolite transition equilibria at low pressures. *Journal of Petrology*, 24(4), 583–604.
- 1502
- 1503 Massonne, H., & Schreyer, W. (1987). Phengite geobarometry based on the limiting assemblage with K-feldspar, phlogopite, and quartz. *Contributions to Mineralogy and Petrology*, 96(2), 212–224.
- 1504
- 1505
- 1506 Moody, J. B., Meyer, D., & Jenkins, J. E. (1983). Experimental characterization of the greenschist/amphibolite boundary in mafic systems. *American Journal of Science*, 283(1), 48–92.
- 1507
- 1508
- 1509 Müller, W., Mancktelow, N. S., & Meier, M. (2000, jan). Rb–Sr microchrons of synkinematic mica in mylonites: an example from the DAV fault of the Eastern Alps. *Earth and Planetary Science Letters*, 180(3–4), 385–397. Retrieved from file:///Users/Behr-admin/Dropbox/Papers/Library.papers3/Articles/M{\%}25C3{\%}25BC1ler/2000/M{\%}25C3{\%}25BC1ler{_}EarthandPlanetaryScienceLetters{_}2000.pdfpapers3://publication/uuid/363451F5-8505-4CFF-ADE2-6E0208DB3E6A
- 1510
- 1511
- 1512
- 1513
- 1514
- 1515 Okrusch, M., & Bröcker, M. (1990, jan). Eclogites associated with high-grade blueschists in the Cyclades archipelago, Greece; a review. *European Journal of Mineralogy*, 2(4), 451–478. Retrieved from <http://eurjmin.geoscienceworld.org/content/2/4/451.shortpapers3://publication/uuid/50C6E894-B8CD-4559-9D35-4FFCBA81AA18>
- 1516
- 1517
- 1518
- 1519 Okrusch, M., Seidel, E., & Davis, E. N. (1978). The assemblage jadeite-quartz in the glaucophane rocks of Sifnos (Cyclades Archipelago, Greece). *N Jb Mineral Abh*, 132, 284–308.
- 1520
- 1521
- 1522 Otsuki, M., & Banno, S. (1990). Prograde and retrograde metamorphism of hematite-bearing basic schists in the sanbagawa belt in central shikoku. *Journal of Metamorphic Geology*, 8(4), 425–439.
- 1523
- 1524
- 1525 Papanikolaou, D. (1987). Tectonic evolution of the Cycladic blueschist belt (Aegean Sea, Greece). In *Chemical transport in metasomatic processes* (Vol. 218, pp. 429–450).
- 1526
- 1527 Papanikolaou, D. (2013, jun). Tectonostratigraphic models of the Alpine terranes and subduction history of the Hellenides. *Tectonophysics*, 595–596, 1–24. Retrieved from <http://linkinghub.elsevier.com/retrieve/pii/S0040195112004854>papers3://publication/doi/10.1016/j.tecto.2012.08.008
- 1528
- 1529
- 1530
- 1531 Park, J.-O., Tsuru, T., Takahashi, N., Hori, T., Kodaira, S., Nakanishi, A., ... Kaneda, Y. (2002). A deep strong reflector in the nankai accretionary wedge from multichannel seismic data: Implications for underplating and interseismic shear stress release. *Journal of Geophysical Research: Solid Earth*, 107(B4), ESE–3.
- 1532
- 1533
- 1534
- 1535 Pe-Piper, G., Piper, D. J., & Matarangas, D. (2002). Regional implications of geochemistry and style of emplacement of Miocene I-type diorite and granite, Delos, Cyclades, Greece. *Lithos*, 60(1–2), 47–66.
- 1536
- 1537
- 1538 Philippon, M., Brun, J. P., & Gueydan, F. (2011, jan). Tectonics of the Syros blueschists (Cyclades, Greece): From subduction to Aegean extension. *Tectonics*, 30, TC4001, doi:10.1029/2010TC002810.
- 1539
- 1540
- 1541 Platt, J. P. (1993, jan). Exhumation of high-pressure rocks: a review of concepts and processes. *Terra Nova*, 5, 119–133. Retrieved from http://acad.coloradocollege.edu/dept/gy/ises/docs/Platt{_}1993{_}Exhumation.pdfpapers3://publication/uuid/5EBBB563-EB8E-4E5A-8BA8-A49488B06448
- 1542
- 1543
- 1544
- 1545 Platt, J. P., Soto, J. I., Whitehouse, M. J., Hurford, A. J., & Kelley, S. P. (1998, jan).

- 1546 Thermal evolution, rate of exhumation, and tectonic significance of . . . *Tecton-*
 1547 *ics*. Retrieved from [http://earth.usc.edu/~jplatt/pdfs/PlattetalTect1998](http://earth.usc.edu/~jplatt/pdfs/PlattetalTect1998.pdfpapers3://publication/uuid/9D98D93B-8C39-4333-9426-DDE259D4F338)
 1548 [.pdfpapers3://publication/uuid/9D98D93B-8C39-4333-9426-DDE259D4F338](http://earth.usc.edu/~jplatt/pdfs/PlattetalTect1998.pdfpapers3://publication/uuid/9D98D93B-8C39-4333-9426-DDE259D4F338)
- 1549 Platt, J. P., Xia, H., & Schmidt, W. L. (2018). Rheology and stress in subduction zones
 1550 around the aseismic/seismic transition. *Progress in Earth and Planetary Science*, *5*,
 1551 1–12.
- 1552 Poulaki, E. M., Stockli, D. F., Flansburg, M. E., & Soukis, K. (2019). Zircon u-pb chronos-
 1553 tratigraphy and provenance of the cycladic blueschist unit and the nature of the contact
 1554 with the cycladic basement on sikinos and ios islands, greece. *Tectonics*.
- 1555 Powell, R., Hergt, J., & Woodhead, J. (2002). Improving isochron calculations with robust
 1556 statistics and the bootstrap. *Chemical Geology*, *185*(3-4), 191–204.
- 1557 Putlitz, B., Cosca, M. A., & Schumacher, J. C. (2005, jan). Prograde mica ⁴⁰Ar/³⁹Ar
 1558 growth ages recorded in high pressure rocks (Syros, Cyclades, Greece). *Chemical Geol-*
 1559 *ogy*, *214*(1-2), 79–98. Retrieved from [http://linkinghub.elsevier.com/retrieve/](http://linkinghub.elsevier.com/retrieve/pii/S0009254104003547)
 1560 [pii/S0009254104003547](http://linkinghub.elsevier.com/retrieve/pii/S0009254104003547)
- 1561 Raase, P. (1974). Al and Ti contents of hornblende, indicators of pressure and temperature of
 1562 regional metamorphism. *Contributions to mineralogy and petrology*, *45*(3), 231–236.
- 1563 Rabillard, A., Jolivet, L., Arbaret, L., Bessière, E., Laurent, V., Menant, A., . . . Beaudoin,
 1564 A. (2018). Synextensional granitoids and detachment systems within cycladic meta-
 1565 morphic core complexes (aegean sea, greece): Toward a regional tectonomagmatic
 1566 model. *Tectonics*, *37*(8), 2328–2362.
- 1567 Raimbourg, H., Jolivet, L., & Leroy, Y. (2007). Consequences of progressive eclogitization on
 1568 crustal exhumation, a mechanical study. *Geophysical Journal International*, *168*(1),
 1569 379–401.
- 1570 Ridley, J. R. (1982). Arcuate lineation trends in a deep level, ductile thrust belt, syros,
 1571 Greece. *Tectonophysics*, *88*(3-4), 347–360. doi: 10.1016/0040-1951(82)90246-3
- 1572 Ridley, J. R. (1984, jan). The significance of deformation associated with blueschist facies
 1573 metamorphism on the Aegean island of Syros. *Geological Society, London, Special*
 1574 *Publications*, *17*(1), 545–550.
- 1575 Ring, U., Glodny, J., Will, T., & Thomson, S. (2007). An Oligocene extrusion wedge
 1576 of blueschist-facies nappes on Evia, Aegean Sea, Greece: implications for the early
 1577 exhumation of high-pressure rocks. *Journal of the Geological Society*, *164*, 637–652.
- 1578 Ring, U., Glodny, J., Will, T., & Thomson, S. (2010, jan). The Hellenic subduction
 1579 system: high-pressure metamorphism, exhumation, normal faulting, and large-scale
 1580 extension. *Annual Review of Earth and Planetary Sciences*, *38*, 45–76. Retrieved
 1581 from [http://www.annualreviews.org/doi/abs/10.1146/annurev.earth.050708](http://www.annualreviews.org/doi/abs/10.1146/annurev.earth.050708.170910papers3://publication/doi/10.1146/annurev.earth.050708.170910)
 1582 [.170910papers3://publication/doi/10.1146/annurev.earth.050708.170910](http://www.annualreviews.org/doi/abs/10.1146/annurev.earth.050708.170910)
- 1583 Ring, U., Glodny, J., Will, T. M., & Thomson, S. (2011). Normal faulting on sifnos and
 1584 the south cycladic detachment system, aegean sea, greece. *Journal of the Geological*
 1585 *Society*, *168*(3), 751–768.
- 1586 Ring, U., & Layer, P. W. (2003). High-pressure metamorphism in the Aegean, eastern
 1587 Mediterranean: Underplating and exhumation from the Late Cretaceous until the
 1588 Miocene to Recent above the retreating Hellenic subduction zone. *Tectonics*, *22*(3).
- 1589 Ring, U., Layer, P. W., & Reischmann, T. (2001). Miocene high-pressure metamor-
 1590 phism in the Cyclades and Crete, Aegean Sea, Greece: Evidence for large-magnitude
 1591 displacement on the Cretan detachment. *Geology*, *29*(5), 395–398. doi: 10.1130/
 1592 [0091-7613\(2001\)029\(0395:MHPMIT\)2.0.CO;2](https://doi.org/10.1130/0091-7613(2001)029(0395:MHPMIT)2.0.CO;2)
- 1593 Ring, U., Pantazides, H., Glodny, J., & Skelton, A. (2020). Forced return flow deep in the
 1594 subduction channel, syros, greece. *Tectonics*, *39*(1), e2019TC005768.
- 1595 Ring, U., & Reischmann, T. (2002). The weak and superfast Cretan detachment, Greece:
 1596 exhumation at subduction rates in extruding wedges. *Journal of the Geological Society*,
 1597 *159*, 225–228. doi: 10.1144/0016-764901-150
- 1598 Ring, U., Thomson, S. N., & Bröcker, M. (2003). Fast extension but little exhumation: the
 1599 Vari detachment in the Cyclades, Greece. *Geological Magazine*, *140*(3), 245–252.
- 1600 Ring, U., Will, T., Glodny, J., Kumerics, C., Gessner, K., Thomson, S., & Drüppel, K.

- 1601 (2007, jan). Early exhumation of high-pressure rocks in extrusion wedges: Cycladic
 1602 blueschist unit in the eastern Aegean, Greece, and Turkey. *Tectonics*, *26*, TC2001.
 1603 Retrieved from <http://www.agu.org/pubs/crossref/2007.../2005TC001872>
 1604 .shtmlpapers3://publication/uuid/11FA1518-AD95-4182-9BE4-2B6413C8D45F
- 1605 Robertson, A. H. F. (2007). Overview of tectonic settings related to the rifting and open-
 1606 ing of Mesozoic ocean basins in the Eastern Tethys: Oman, Himalayas and Eastern
 1607 Mediterranean regions. *Geological Society, London, Special Publications*, *282*(1), 325–
 1608 388.
- 1609 Robinson, P. (1982). Phase relations of metamorphic amphiboles: Natural occurrences and
 1610 theory. *Rev. Mineral.*, *9*, 1–227.
- 1611 Roche, V., Laurent, V., Cardello, G. L., Jolivet, L., & Scaillet, S. (2016). Anatomy of the
 1612 cycladic blueschist unit on Sifnos island (Cyclades, Greece). *Journal of Geodynamics*,
 1613 *97*, 62–87.
- 1614 Rogowitz, A., Grasemann, B., Huet, B., & Habler, G. (2014). Strain rate dependent calcite
 1615 microfabric evolution—an experiment carried out by nature. *Journal of Structural*
 1616 *Geology*, *69*, 1–17.
- 1617 Romer, R. L., & Rotzler, J. (2011). The role of element distribution for the isotopic dating
 1618 of metamorphic minerals. *European Journal of Mineralogy*, *23*(1), 17–33.
- 1619 Rondenay, S., Abers, G. A., & van Keken, P. E. (2008, jan). Seis-
 1620 mic imaging of subduction zone metamorphism. *Geology*, *36*(4), 274–
 1621 275. Retrieved from <http://geology.gsapubs.org/cgi/doi/10.1130/G24112A.1>
 1622 .1papers3://publication/doi/10.1130/G24112A.1
- 1623 Rosenbaum, G., Avigad, D., & Sánchez-Gómez, M. (2002, jan). Coaxial flattening at deep
 1624 levels of orogenic belts: evidence from blueschists and eclogites on Syros and Sifnos
 1625 (Cyclades, Greece). *Journal of Structural Geology*, *24*, 1451–1462.
- 1626 Ruffet, G., Féraud, G., Ballèvre, M., & Kiénaast, J. R. (1995, jan). Plateau ages and excess
 1627 argon in phengites: an ⁴⁰Ar ³⁹Ar laser probe study of Alpine micas (Sesia Zone,
 1628 Western Alps, northern Italy). *Chemical Geology*, *121*(1-4), 327–343. Retrieved from
 1629 papers3://publication/uuid/6814706D-6FE8-4CF0-B86A-7D88DAD96861
- 1630 Schliestedt, M. (1986). Eclogite-blueschist relationships as evidenced by mineral equilibria
 1631 in the high-pressure metabasic rocks of Sifnos (Cycladic Islands), Greece. *Journal of*
 1632 *Petrology*, *27*(6), 1437–1459. doi: 10.1093/petrology/27.6.1437
- 1633 Schmädicke, E., & Will, T. M. (2003). Pressure-Temperature evolution of blueschist facies
 1634 rocks from Sifnos, Greece, and implications for the exhumation of high-pressure rocks
 1635 in the Central Aegean. *Journal of Metamorphic Geology*, *21*(8), 799–811. doi: 10
 1636 .1046/j.1525-1314.2003.00482.x
- 1637 Schmidt, M. W. (1992). Amphibole composition in tonalite as a function of pressure: an ex-
 1638 perimental calibration of the Al-in-hornblende barometer. *Contributions to mineralogy*
 1639 *and petrology*, *110*(2-3), 304–310.
- 1640 Schneider, D. A., Grasemann, B., Lion, A., Soukis, K., & Draganits, E. (2018). Geodynamic
 1641 significance of the Santorini Detachment System (Cyclades, Greece). *Terra Nova*.
- 1642 Schumacher, J. C., J.B., B., Cheney, J. T., Tonnsen, R. R., Brady, J. B.,
 1643 Cheney, J. T., & Tonnsen, R. R. (2008, aug). Glaucophane-bearing
 1644 Marbles on Syros, Greece. *J. Petrology*, *49*(9), 1667–1686. Retrieved
 1645 from [http://www.petrology.oxfordjournals.org/cgi/doi/10.1093/petrology/](http://www.petrology.oxfordjournals.org/cgi/doi/10.1093/petrology/egn042papers3://publication/doi/10.1093/petrology/egn042)
 1646 [egn042papers3://publication/doi/10.1093/petrology/egn042](http://www.petrology.oxfordjournals.org/cgi/doi/10.1093/petrology/egn042)
- 1647 Seck, H. A., Koetz, J., Okrusch, M., Seidel, E., & Stosch, H.-G. (1996). Geochemistry of a
 1648 meta-ophiolite suite: an association of metagabbros, eclogites and glaucophanites on
 1649 the island of Syros, Greece. *European Journal of Mineralogy*, 607–624.
- 1650 Seidel, E., Kreuzer, H., & Harre, W. (1982). A late oligocene/early miocene high pressure
 1651 belt in the external Hellenides. *Geologisches Jahrbuch. Reihe E, Geophysik*(23), 165–
 1652 206.
- 1653 Seman, S. (2016). *The tectonostratigraphy of the Cycladic Blueschist Unit and new garnet*
 1654 *geo/thermochronology techniques* (Unpublished doctoral dissertation).
- 1655 Seman, S., Stockli, D., & Soukis, K. (2017). The provenance and internal structure of the

- 1656 Cycladic Blueschist Unit revealed by detrital zircon geochronology, Western Cyclades,
1657 Greece. *Tectonics*, 36(7), 1407–1429.
- 1658 Sherlock, S. C., & Arnaud, N. O. (1999). Flat plateau and impossible isochrons: Apparent
1659 40ar-39ar geochronology in a high-pressure terrain. *Geochimica et Cosmochimica Acta*,
1660 63(18), 2835–2838.
- 1661 Skelton, A., Peillod, A., Glodny, J., Klonowska, I., Månbro, C., Lodin, K., & Ring, U.
1662 (2019). Preservation of high-P rocks coupled to rock composition and the absence of
1663 metamorphic fluids. *Journal of Metamorphic Geology*.
- 1664 Skora, S., Baumgartner, L. P., Mahlen, N. J., Johnson, C. M., Pilet, S., & Hellebrand,
1665 E. (2006). Diffusion-limited ree uptake by eclogite garnets and its consequences for
1666 lu-hf and sm-nd geochronology. *Contributions to Mineralogy and Petrology*, 152(6),
1667 703–720.
- 1668 Soukis, K., & Stockli, D. F. (2013, jan). Structural and thermochronometric evidence
1669 for multi-stage exhumation of southern Syros, Cycladic islands, Greece. *Tectono-*
1670 *physics*, 595-596, 148–164. Retrieved from [http://www.sciencedirect.com/
1671 science/article/pii/S0040195112002806papers3://publication/uuid/
1672 E4EA6C10-9045-4A74-AF9D-OD016D22F6A8](http://www.sciencedirect.com/science/article/pii/S0040195112002806papers3://publication/uuid/E4EA6C10-9045-4A74-AF9D-OD016D22F6A8)
- 1673 Sousa, J., Kohn, M. J., Schmitz, M. D., Northrup, C. J., & Spear, F. (2013). Stron-
1674 tium isotope zoning in garnet: implications for metamorphic matrix equilibration,
1675 geochronology and phase equilibrium modelling. *Journal of Metamorphic Geology*,
1676 31(4), 437–452.
- 1677 Thompson, R. (1974). Some high-pressure pyroxenes. *Mineralogical Magazine*, 39(307),
1678 768–787.
- 1679 Thomson, S. N., Stöckhert, B., & Brix, M. R. (1999). Miocene high-pressure metamor-
1680 phic rocks of crete, greece: rapid exhumation by buoyant escape. *Geological Society,
1681 London, Special Publications*, 154(1), 87–107.
- 1682 Tomaschek, F., Keiter, M., Kennedy, A. K., & Ballhaus, C. (2008). Pre-Alpine basement
1683 within the Northern Cycladic Blueschist Unit on Syros Island, Greece [Präalpines
1684 Grundgebirge in der Nördlichen Kykladischen Blauschieferinheit auf der Insel Syros,
1685 Griechenland.]. *Zeitschrift der deutschen Gesellschaft für Geowissenschaften*, 159(3),
1686 521–531.
- 1687 Tomaschek, F., Kennedy, A. K., Villa, I. M., Lagos, M., & Ballhaus, C. (2003). Zircons from
1688 Syros, Cyclades, Greece—recrystallization and mobilization of zircon during high-
1689 pressure metamorphism. *Journal of Petrology*, 44(11), 1977–2002.
- 1690 Trotet, F., Jolivet, L., & Vidal, O. (2001). Tectono-metamorphic evolution of Syros and
1691 Sifnos islands (Cyclades, Greece). *Tectonophysics*, 338(2), 179–206. doi: 10.1016/
1692 S0040-1951(01)00138-X
- 1693 Trotet, F., Vidal, O., & Jolivet, L. (2001). Exhumation of Syros and Sifnos metamorphic
1694 rocks (Cyclades, Greece). New constraints on the PT paths. *European Journal of
1695 Mineralogy*, 13(5), 901–902.
- 1696 Ukar, E., Cloos, M., & Vasconcelos, P. (2012). First 40ar-39ar ages from low-t mafic
1697 blueschist blocks in a franciscan mélange near san simeon: Implications for initiation
1698 of subduction. *The Journal of Geology*, 120(5), 543–556.
- 1699 Uunk, B., Brouwer, F., ter Voorde, M., & Wijbrans, J. (2018). Understanding phengite
1700 argon closure using single grain fusion age distributions in the Cycladic Blueschist
1701 Unit on Syros, Greece. *Earth and Planetary Science Letters*, 484, 192–203.
- 1702 Vanderhaeghe, O., & Whitney, D. (2004). Structural development of the naxos migmatite
1703 dome. *SPECIAL PAPERS-GEOLOGICAL SOCIETY OF AMERICA*, 211–228.
- 1704 van der Maar, P. A., & Jansen, J. B. H. (1983). The geology of the polymetamorphic complex
1705 of Ios, Cyclades, Greece and its significance for the Cycladic Massif. *Geologische
1706 Rundschau*, 72(1), 283–299.
- 1707 Van Hinsbergen, D. J., Torsvik, T. H., Schmid, S. M., Mañenco, L. C., Maffione, M., Vissers,
1708 R. L., ... Spakman, W. (2020). Orogenic architecture of the mediterranean region
1709 and kinematic reconstruction of its tectonic evolution since the triassic. *Gondwana
1710 Research*, 81, 79–229.

- 1711 Vermeesch, P. (2018). Isoplotr: A free and open toolbox for geochronology. *Geoscience*
1712 *Frontiers*, 9(5), 1479–1493.
- 1713 Villa, I. M., De Bièvre, P., Holden, N., & Renne, P. (2015). Iupac-iugs recommendation on
1714 the half life of ^{87}Rb . *Geochimica et Cosmochimica Acta*, 164, 382–385.
- 1715 Wakabayashi, J. (1990). Counterclockwise PTt paths from amphibolites, Franciscan Com-
1716 plex, California: Relics from the early stages of subduction zone metamorphism. *The*
1717 *Journal of Geology*, 98(5), 657–680.
- 1718 Warren, C. J., Beaumont, C., & Jamieson, R. A. (2008, apr). Forma-
1719 tion and exhumation of ultra-high-pressure rocks during continental collision:
1720 Role of detachment in the subduction channel. *Geochem. Geophys. Geosyst*,
1721 9(4). Retrieved from [http://doi.wiley.com/10.1029/2007GC001839papers3://](http://doi.wiley.com/10.1029/2007GC001839papers3://publication/doi/10.1029/2007GC001839)
1722 [publication/doi/10.1029/2007GC001839](http://doi.wiley.com/10.1029/2007GC001839)
- 1723 Wendt, I., & Carl, C. (1991). The statistical distribution of the mean squared weighted
1724 deviation. *Chemical Geology: Isotope Geoscience Section*, 86(4), 275–285.
- 1725 Wijbrans, J., & McDougall, I. (1988). Metamorphic evolution of the attic cycladic metamor-
1726 phic belt on naxos (cyclades, greece) utilizing $^{40}\text{Ar}/^{39}\text{Ar}$ age spectrum measurements.
1727 *Journal of Metamorphic Geology*, 6(5), 571–594.
- 1728 Wijbrans, J. R., Schliestedt, M., & York, D. (1990). Single grain argon laser probe dating of
1729 phengites from the blueschist to greenschist transition on Sifnos (Cyclades, Greece).
1730 *Contributions to Mineralogy and Petrology*, 104, 582–593.
- 1731 Xia, H., & Platt, J. P. (2017). Structural and rheological evolution of the Laramide sub-
1732 duction channel in southern California. *Solid Earth*, 8(2).
- 1733 Yakymchuk, C., Clark, C., & White, R. W. (2017). Phase relations, reaction sequences and
1734 petrochronology. *Reviews in Mineralogy and Geochemistry*, 83(1), 13–53.